8. FUSION POWER CORE ENGINEERING

S. P. Grotz, J. P. Blanchard, E. T. Cheng, P. I. H. Cooke,
R. W. Conn, R. L. Creedon, A. E. Dabiri, W. P. Duggan,
O. Fischer, N. M. Ghoniem, P. J. Gierszewski, G. Gorker,
M. Z. Hasan, C. E. Kessel, R. A. Krakowski, O. Kveton,
R. C. Martin, F. Najmabadi, G. E. Orient, K. R. Schultz,
S. Sedehi, S. Sharafat, D. Steiner, D. K. Sze,
E. L. Vold, and C. P. C. Wong

CONTENTS

8.1. Introduction 8-1
8.2. Self-Cooled Lithium Vanadium Blanket Design 8-4
8.2.1. Concept Description 8-4
8.2.2. Materials 8-11
8.2.3. Neutronics 8-17
8.2.4. Thermal Hydraulics 8-26
8.2.5. Integrated Blanket-Coil Concept (IBC) 8-37
8.2.6. Structural Analysis 8-43
8.2.7. Tritium 8-58
8.2.8. Conclusions 8-60
8.3. Aqueous Loop-in-Pool Blanket Design 8-61
8.3.1. Concept Description 8-62
8.3.2. Materials 8-69
8.3.3. Neutronics 8-75
8.3.4. Thermal Hydraulics 8-78
8.3.5. Structural Analysis 8-80
8.3.6. Tritium 8-84
8.3.7. Safety 8-91
8.3.8. Conclusions 8-92
8.4. Flibe Pool Design (IPFR) 8-93
8.4.1. Concept Description 8-93
8.4.2. Materials 8-96
8.4.3. Thermal Hydraulics 8-97
8.4.4. Materil Compatibility and Tritium Containment 8-99
8.4.5. Safety 8-102
8.4.6. Conclusions 8-103
8.5. Helium-Cooled Cermaic Blabket Design (FISC) 8-103
8.5.1. Concept Description 8-103
8.5.2. Materials 8-107
8.5.3. Thermal Hydraulics 8-111
8.5.4. Neutronics 8-115
8.5.5. Structural Analysis 8-117
8.5.6. Tritium 8-124
8.5.7. Safety 8-124
8.5.8. Conclusions 8-126
8.6. Directions for the Design Phase 8-127
References 8-129

8. FUSION POWER CORE ENGINEERING

8.1. INTRODUCTION

The TITAN research program is a multi-institutional effort to determine the potential of the reversed-field pinch (RFP) magnetic fusion concept as a compact, high-power-density, and "attractive" fusion energy system from economic (cost of electricity, COE), environmental, and operational view-points. In particular, a high neutron wall loading design (18 MW/m^2) has been chosen as the reference case in order to quantify the issue of engineering practicality, to assess significant benefits of compact systems, and to illuminate the main drawbacks. The program has been divided into two phases, each roughly one year in length: the Scoping Phase and the Design Phase.

During the first half of the scoping phase of the TITAN project several fusion power core (FPC) concepts were proposed and studied in various degrees of detail (Sec. 3). The four concepts which were selected for further analysis are presented in this section. The "final four" designs are:

- A self-cooled, lithium loop design with a vanadium alloy structure.
- An aqueous, self-cooled design with a copper first wall, beryllium neutron multiplier and Primary-Candidate-Alloy (PCA) structure.
- A self-cooled FLiBe pool design using a vanadium alloy structure.
- A helium-cooled ceramic design with a solid breeder and silicon carbide structure.

These four designs are described in Sec. 8.2 to 8.5, respectively. The performance of these designs was investigated in several areas: materials, neutronics, thermal hydraulics, structural analysis, tritium and safety analysis. A brief description of the general activities in each of these areas follows. A list of the general reactor operating parameters is shown in Table 8.1.-I.

Material properties were studied in the scoping phase to determine the feasibility and lifetime of materials in the fusion environment. The compactness of the FPC inevitably introduces a unique set of materials issues

TABLE 8.1.-I
GENERAL REACTOR OPERATING PARAMETERS

14 MeV neutron wall load, (MW/m^2)	18.
Plasma major radius (m)	3.9
Plasma minor radius (m)	0.60
Plasma aspect ratio	6.5
Reversed toroidal field during burn (T)	0.36
Poloidal field at plasma surface (T)	5.9
Net electric power (MW)	1,000.

associated with high power densities. These include management of very high surface heat loads, relatively short blanket material chronological lifetime because of higher radiation-damage rates and strong coupling between mechanical, chemical and electromagnetic environments. An effective irradiation-temperature operational lifetime window can be established if stress, swelling, embrittlement and creep behaviour are assessed. The limited data base for fusion reactor materials impedes efforts to establish such a lifetime window. For example, the stress environment can be estimated fairly accurately at beginning of life (BOL). However, changes in the microstructure of materials make it difficult to determine accurate stress responses of the materials as a function of time. Without sufficient data only crude estimates can be made based on an understanding of basic and fundamental processes taking place. The study has concentrated, therefore, on filling the gaps of experimental data with phenomenological equations which rely heavily on an understanding of fundamental processes.

During the scoping phase the neutronics analysis was primarily limited to one-dimensional investigations using the discrete ordinates transport code, ANISN [1].

For the TITAN reactor, the following neutronics design goals were chosen:

1. Local (full coverage, one-dimensional result) tritium breeding ratio should be larger than 1.2.

2. Life-of-plant (30 full power year) OH coils is desirable.

3. The blanket energy multiplication (M_n) should be maximized. Values of M_n greater than 1.2 are desired.

The neutronics scoping studies were performed to understand, parametrically, the general nuclear performance of the TITAN FPC design. All neutronics calculations in the scoping phase were performed using ANISN [1], with P_3S_8 approximations in cylindrical geometry. The cross section library employed is the 30 neutron 12 gamma-ray group MATXS5 library, processed at Los Alamos and based on the ENDF/B-V files [2]. The results of these calculations are expected to be within 2 to 3% of that calculated from the Monte Carlo code, MCNP [3], and continuous energy library, RMCCS [4], as will be shown later in the discussion of the reference design.

In a compact high neutron wall load device (18 MW/m^2) the first wall could have surface heat fluxes as high as 4.5 MW/m^2 and volumetric heat generation in the 100 MW/m^3 range. Detailed thermal-hydraulic analysis has been performed to ensure that all temperature limits are satisfied and that the power is removed at maximum efficiency for use in the thermal energy conversion cycle. The analysis made during the scoping phase involved a wide range of configurations (e.g., materials, coolant and structure). One-dimensional, analytical solutions and two-dimensional finite-element analyses were employed for all aspects of the thermal-hydraulic analysis.

Reversed-field pinch experiments appear to operate well even when the dominant core-plasma loss mechanism is radiation rather than conductive or convective energy transport. This highly radiative plasma mode of operation is particularly advantageous for high wall loading systems, as it distributes the plasma energy loss uniformly on the walls. This approach has been adopted for TITAN. A key parameter, f_{RAD}, has been defined as the ratio of radiative losses to the total plasma energy losses. For the 18 MW/m^2 base line, the heat flux on the first wall is roughly $4.5 \times f_{RAD}$ MW/m^2. For the purpose of the scoping phase, it was assumed that f_{RAD} can be varied, and for each design the maximum heat flux limitation of the first wall was determined. Although any first wall design is feasible if f_{RAD} is made sufficiently small, the decreased radiation results in higher heat fluxes in the divertor. Therefore, the first-wall thermal analysis must be closely coupled to the divertor thermal analysis (Sec. 6.5) for an optimized design.

The structural analysis of the FPC must consider both the thermal and hydrostatic loads. The high surface heat flux can lead to severe thermal

stresses, just as it can lead to excessive peak temperatures. Efficient energy recovery often requires high-pressure coolant, which generally leads to the dominant primary stress. Both analytical and numerical thermo-structural analyses have been performed during the scoping phase for the four FPC concepts.

The major issues for tritium systems are adequate tritium breeding and concerns in handling and containing the tritium. Tritium inventory and permeation relate to the safety of tritium containment and release during operation and maintenance. Tritium is a beta-emitter with a half-life of 12.3 years and an activity of 10,000 Ci/g. With a daily tritium production of about 360 g in the blanket, a very large radioactive inventory must be contained. Assuming a burn-up fraction of 10%, over 3 kg of tritium must flow through the plasma chamber and be cleaned and recycled each day, along with removal and cleaning of at least 360 g from the breeder. With atmospheric release limits of 10 to 100 Ci/d required, especial attention should be given to tritium containment. Containment becomes a greater concern with high-temperature operation as hydrogen isotopes can permeate through metals and other containment structures. A tritium systems flow diagram is shown in Fig. 8.1.-1, which is used to calculate inventory and leakage rates for the TITAN blanket designs.

The TITAN study is aiming towards a fusion reactor with four major features: minimum cost of electricity, high availability, design simplicity, and improved safety. These goals may not be achieved simultaneously and trade-offs are required. For example, if add-on safety equipment is needed, the design can become more complex and have lower availability and higher cost. On the other hand, if the safety features are incorporated in the design from the beginning, the reactor can potentially be inherently safe, simpler, and have higher availability and lower cost. The TITAN study, therefore, has designated safety as an integral part of the design activity.

8.2. SELF-COOLED LITHIUM VANADIUM BLANKET DESIGN

8.2.1. Concept Description

The TITAN lithium-vanadium blanket concept is a self-cooled design with liquid-lithium as the coolant and breeder and a vanadium-alloy structure. The general configuration is shown in Figs. 8.2.-1 and 8.2.-2. Operating parameters are listed in Table 8.2.-I. Both the blanket and first wall are cooled with lithium. The first wall and blanket coolant flow paths are poloidal, single pass with different exit temperatures as shown in Figs. 8.2.-1 and 8.2.-2. The

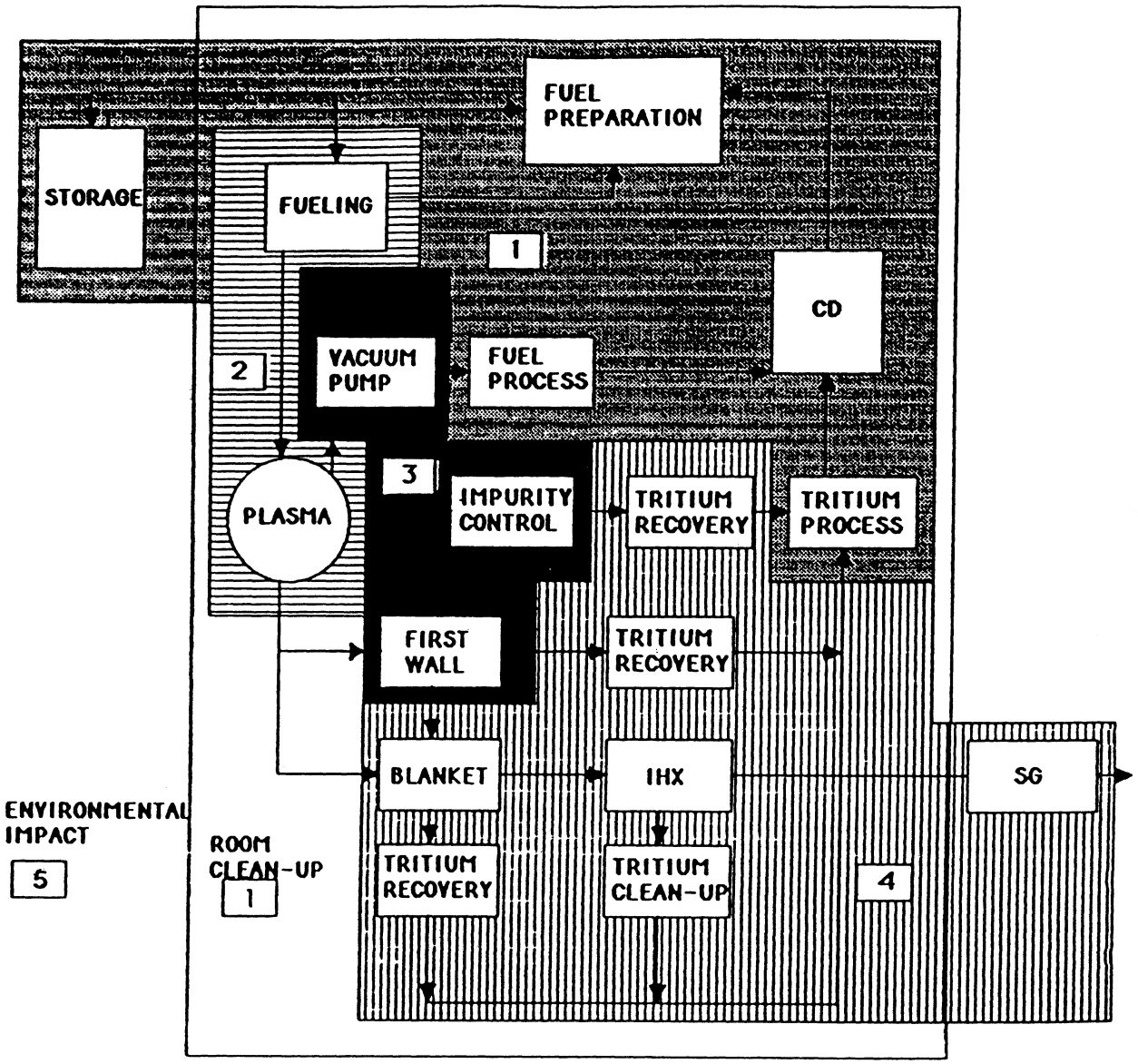

Fig. 8.1.-1. Tritium flow paths through the various reactor sub-systems.

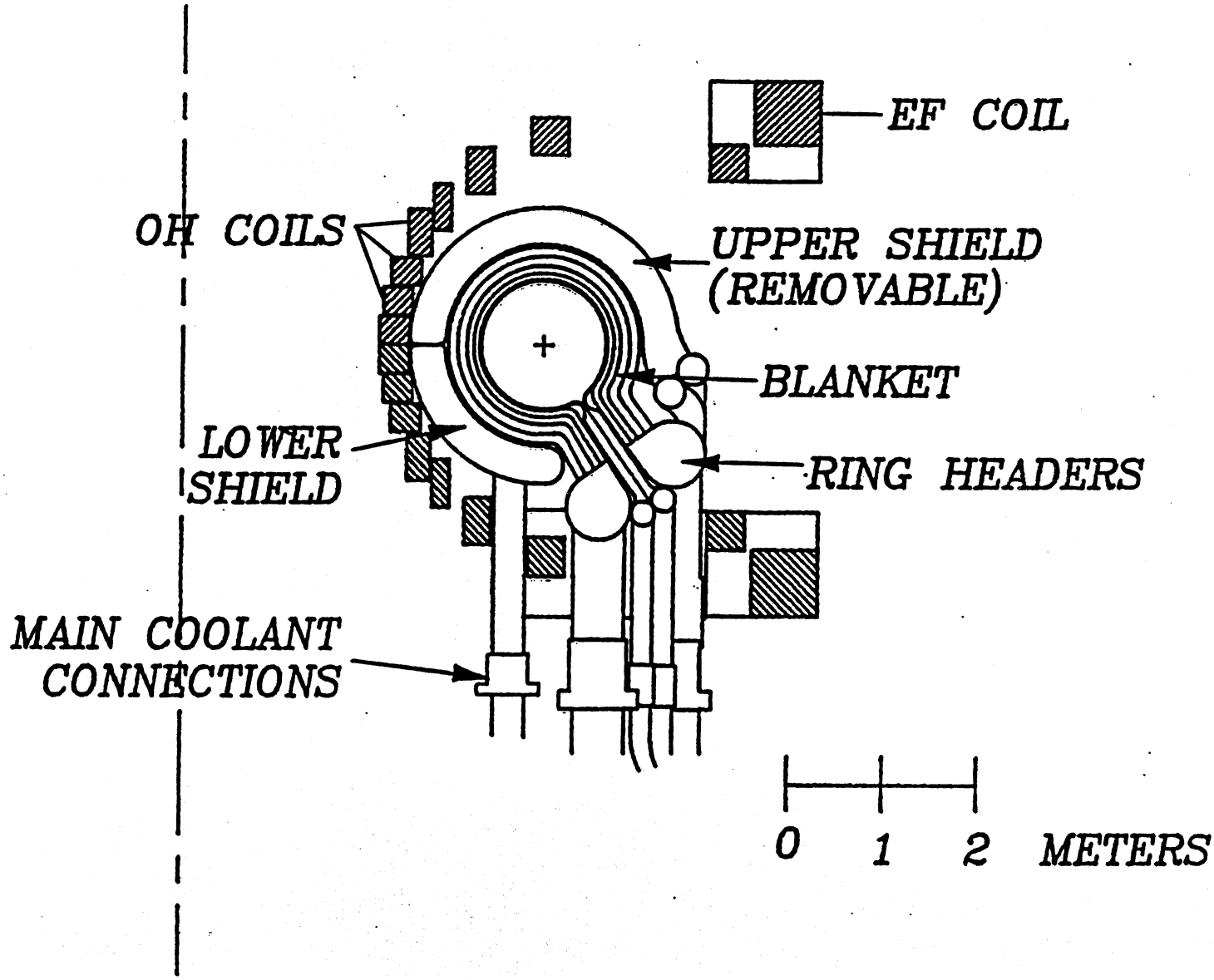

Fig. 8.2.-1. The poloidal cross section of TITAN lithium-vanadium design.

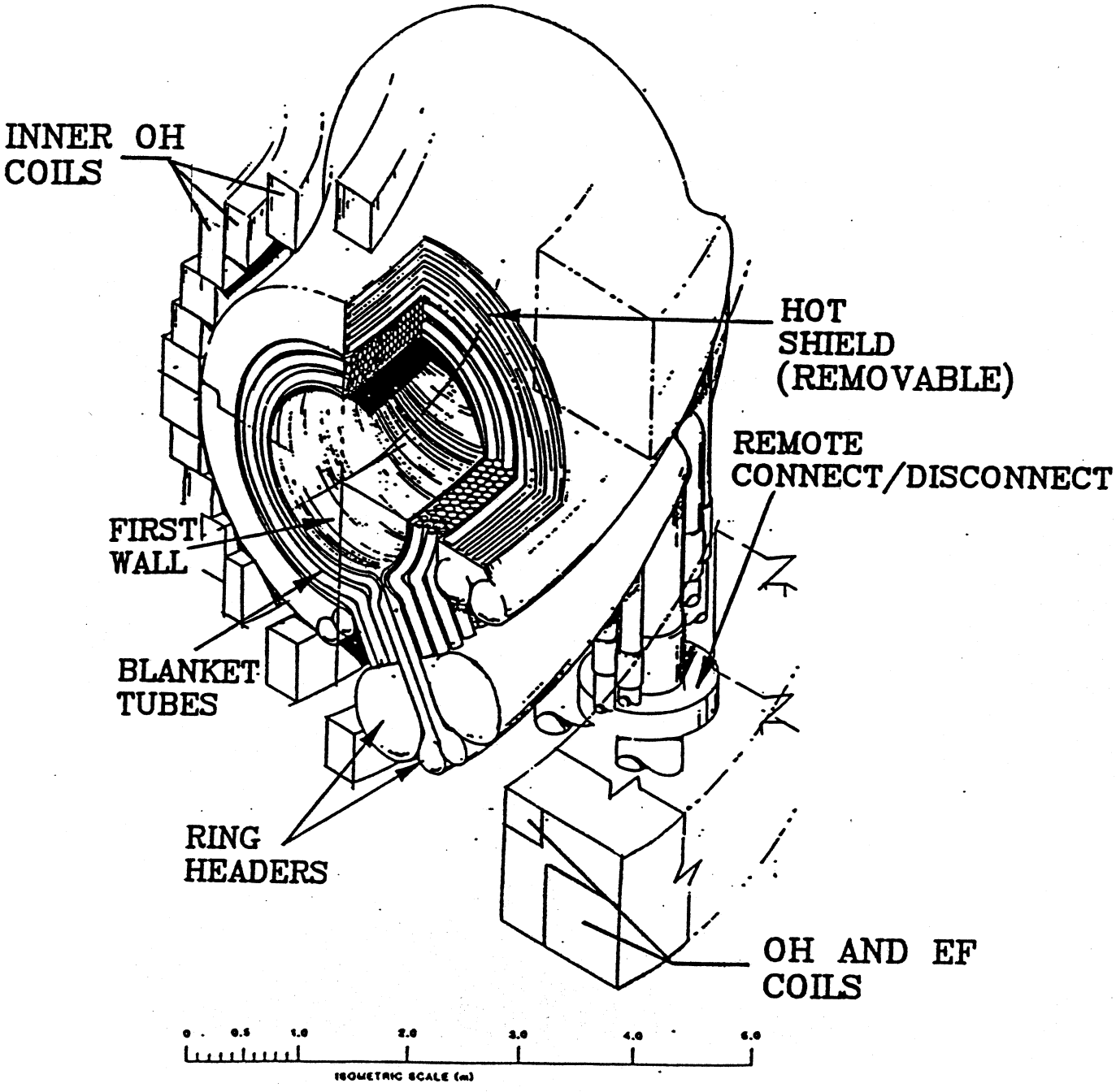

Fig. 8.2.-2. Isometric view of TITAN lithium-vanadium blanket design.

TABLE 8.2.-I
OPERATING PARAMETERS FOR THE LITHIUM-VANADIUM DESIGN

FIRST WALL

Description: Bank of lithium-cooled, seamless circular tubes; poloidal single pass flow; inter-tube welds for toroidal electrical circuit and to reduce fretting.

Structural material	V-3Ti-1Si
Tube o.d. (mm)	10.5
Tube i.d. (mm)	8.0
Erosion allowance (mm)	0.25
Design lifetime (full power year, FPY)	1.
Poloidal radius (m)	0.68
Number of tubes	2,440.
First wall area (m^2)	166.
Surface heat flux, peak (MW/m^2)	4.7
Volumetric heat generation (MW/m^3)	
- Lithium	76.
- Vanadium	107.
Inlet temperature (°C)	300.
Outlet temperature (°C)	393.
Mass flow rate (kg/s)	1,460.
Volume flow rate (m^3/s)	3.08
Velocity, peak (m/s)	22.5
Pressure drop (MPa)	11.2

two streams are mixed at the exit to achieve the desired bulk outlet temperature. Details of the first wall and blanket thermal hydraulics are discussed in Section 8.2.4.

The first wall consists of a bank of tubes with a nominal diameter of 10 mm. The relative tube positions vary with poloidal position to accommodate the wedge effect of the toroidal geometry. Typical first-wall cross sections are illustrated in Fig. 8.2.-3 for the inboard, top/bottom and outboard first wall locations. The change in toroidal width of the first-wall tube bank from inboard to outboard is 43%.

The breeding blanket consists of a bank of large tubes (75 mm o.d.), stacked 4-deep to form a 0.30 m thick blanket. These tubes must have decreased toroidal width on the inboard side to accommodate the toroidal geometry. The maximum increase in tube width from inboard to outboard is 64%. A typical blanket sector cross section is shown in Fig. 8.2.-4.

The shield for the lithium design is a two-piece, hot shield located behind the breeding blanket. The shield is designed to be a life-of-plant component because the radiation-damage rates are low relative to the first wall and

TABLE 8.2.-I (cont.)
OPERATING PARAMETERS FOR THE LITHIUM-VANADIUM DESIGN

BLANKET

Description: 4 rows of varying cross section, seamless tubes increased structural fraction with depth into blanket to maximize shield lifetime.

Structural material	V-3Ti-1Si
Tube o.d. (mm)	75.
Tube wall thickness (mm)	
- Row 1	2.75
- Row 2	3.25
- Row 3	4.00
- Row 4	4.50
Blanket thickness (m)	0.30
Volume fractions,	
- Lithium	0.64
- Vanadium	0.14
- Void	0.22
Volumetric heat generation, peak (MW/m^3)	
- Lithium	65.
- Vanadium	102.
Inlet temperature (°C)	300.
Outlet temperature (°C)	681.
Mass flow rate (kg/s)	667.
Volumetric flow rate (m^3/s)	1.4
Velocity, peak (m/s)	0.3
Pressure drop (MPa)	1.2

SHIELD

Description: Lithium cooled, 2-piece hot shield; double-pass poloidal flow.

Structural material	V-3Ti-1Si
Moderator/absorber	HT-9
Volume fractions	
- Lithium	0.445
- Vanadium	0.044
- HT-9	0.511
Lifetime (dpa)	200.-250.
Damage rate, peak (dpa/FPY)	47.2
Inlet temperature (°C)	300.
Outlet temperature (°C)	681.
Mass flow rate (kg/s)	667.
Volumetric flow rate (m^3/s)	1.4

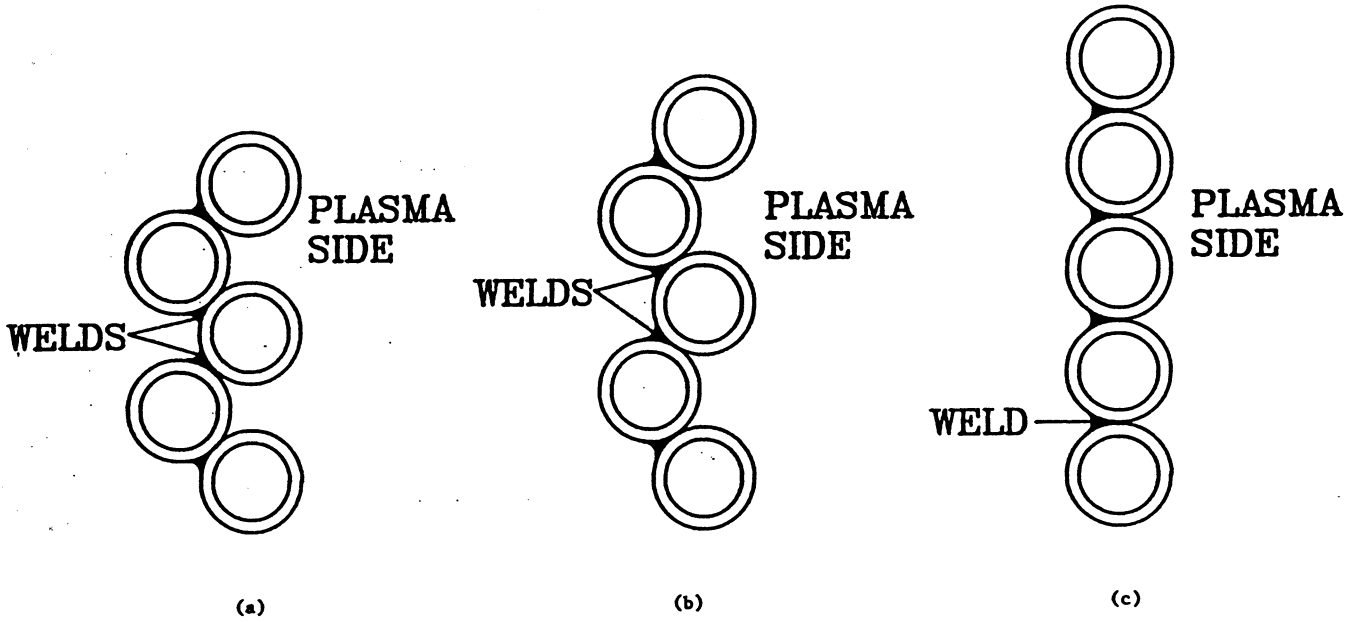

Fig. 8.2.-3. Cross section of the first wall of the lithium-vanadium design, (a) inboard, (b) top/bottom, (c) outboard.

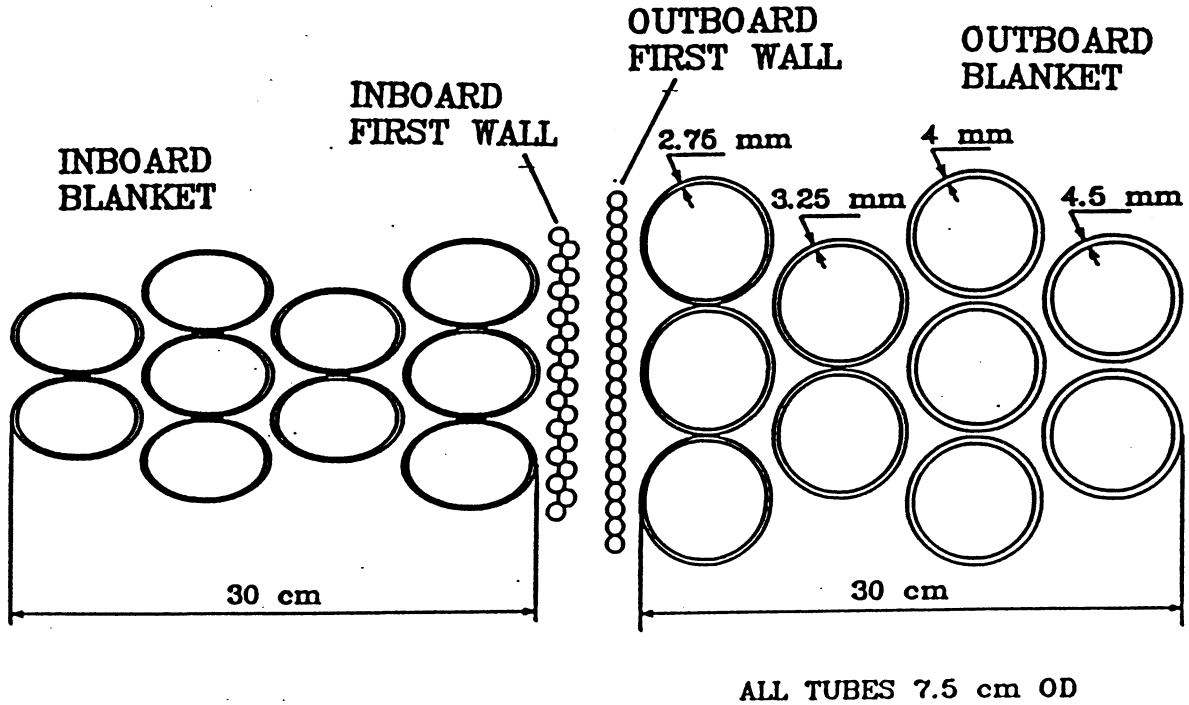

Fig. 8.2.-4. Horizontal, mid-plane cross section of the lithium-vanadium design.

blanket. Re-using the shield following a first-wall and blanket replacement reduces the yearly waste disposal from ~400 tonnes to ~50 tonnes. Approximately 40% of the neutron energy is recovered in the hot shield. The lithium coolant in the shield is mixed with first wall and blanket streams upon exit. The two-piece design requires a separate header set for each half of the shield. The lower shield segment is permanently installed.

The inlet and outlet ring headers for the first wall and blanket are located below the torus. A separate inlet header for the first wall is necessary because of the pressure requirements of the first wall thermal hydraulics (see Sec. 8.2.4). The first wall and blanket coolant streams are mixed together prior to entering the intermediate heat exchanger (IHX).

The remote connect/disconnects for the reactor torus (including the first wall, blanket, shield, and the divertor sections) are located on the pump/IHX side of the ring headers. This location minimizes the number of remotely handled connections. A bottom-access header system is chosen as opposed to an outboard midplane location because of the limited clearance between the reactor torus and the outer OH and EF coils (Fig. 8.2.-2) for headers and remotely activated shear joints . Non-moveable outer coils are chosen to minimize the number of components moved during first wall and blanket replacement. In addition, the delicate nature of the large superconducting EF coils may place limits on their mobility.

The upper shield segment is removed and placed aside for access to the first wall and blanket during replacement. After a new pre-tested first wall and blanket is installed the upper shield segment is placed back on top of the torus for operation.

A unique feature of this design is the integration of the breeding blanket with the toroidal field coils. The integrated-blanket-coil (IBC) concept [5] is discussed in Sec. 8.2.5. Key features of the IBC are: FPC simplification, reduced shielding requirements, easier access to the first wall and blanket, and reduced toroidal-field ripple.

8.2.2. Materials

8.2.2.1. Structural Material

The high power density of the TITAN reactor calls for a first wall and blanket structural material which is capable of high temperature operation. Comparison between thermal-stress factors and lithium corrosion limits of

vanadium-based alloys, HT-9, and PCA steels of BCSS [6] clearly points to the superiority of vanadium alloys, particularly at temperatures above 600°C. Three vanadium based alloys: V-15Cr-5Ti, VANSTAR-7 and V-3Ti-1Si, were studied and compared for the TITAN lithium-vanadium design.

Physical properties of vanadium-based alloys are not sensitive to moderate compositional variations [7]. Data for similar vanadium-based alloys can be regarded as representative for V-3Ti-1Si. Table 8.2.-II summarizes some of the properties as selected from Ref. 7.

To simplify assessment of material behaviour the complex interaction of the irradiation, stress, chemical, thermal and electromechanical environments can be divided into two categories: (1) high temperature irradiation effects on physical properties and (2) coolant compatibility issues. Point defect production during irradiation causes hardening of the matrix because of

Table 8.2.-II.
PHYSICAL PROPERTIES ADOPTED FOR V-3Ti-1Si [7]

Melting point (°C)	1,890.
Density (kg/m^3)	6,100.
Poisson's ratio	0.36
Young's modulus (GPa)	127.
Linear thermal expansion ($10^{-6}/K$)	
400°C	10.2
500°C	10.3
600°C	10.5
Thermal conductivity (W/m-K)	
400°C	26.8
500°C	28.0
600°C	29.5
Electrical resistivity (μΩ-m)	
400°C	0.67
500°C	0.74
600°C	0.81
Specific heat (J/kg-K)	
400°C	535.
500°C	560.
600°C	575.

dislocation obstacle interactions. Hydrogen generation in structural materials during irradiation raises the concern of hydrogen embrittlement. Since the hydrogen concentrations required for the formation of hydrides in metals are large, hydrogen production and pickup has not been of great concern [8]. Loomis [9] has reported that hydrogen concentrations above 5000 appm are required to raise the ductile-to-brittle transition temperature (DBTT) of vanadium above room temperature [9]. Table 8.2.-III shows anticipated hydrogen and helium production rates in a vanadium first wall exposed to a 20 MW/m^2 neutron wall loading. Figures 8.2.-5.a,b illustrate the unirradiated and irradiated stress-strain characteristics of the candidate vanadium alloys.

Helium production from nuclear reactions enhances embrittlement. Latest results of irradiation hardening and helium production of the three vanadium-based alloys [10] show clearly that V-3Ti-1Si outperforms the other two in resisting the effects of neutron irradiation and helium generation. Because of lack of creep data for irradiated vanadium-based alloys, creep behavior under irradiation can only be estimated. Preliminary calculations [11] show that V-3Ti-1Si has a marginal creep behavior for TITAN design limits (lifetime ~ 1 yr and allowable stress range of 100 to 150 MPa). More detailed calculations of

Table 8.2.-III
HYDROGEN AND HELIUM PRODUCTION RATES IN THE FIRST WALL
OF THE LITHIUM DESIGN AT 20 MW/m^2 NEUTRON WALL LOADING [1]

Isotope	appm per year
H	6,287
D	332
T	36
Total Hydrogen	6,655
^3He	nil
^4He	1,500
Total Helium	1,500

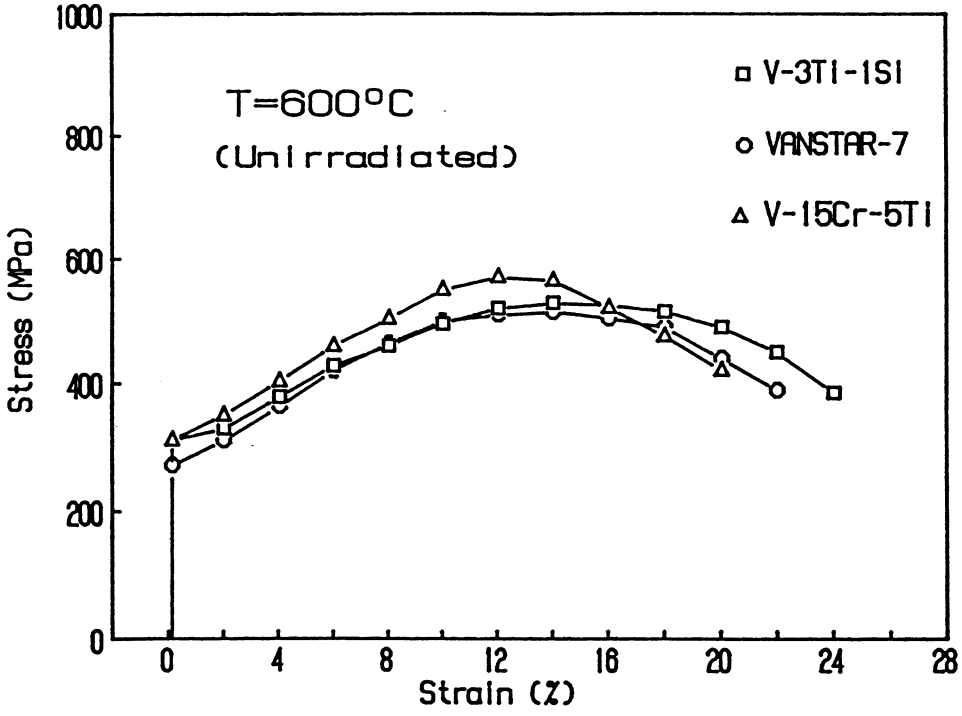

(a)

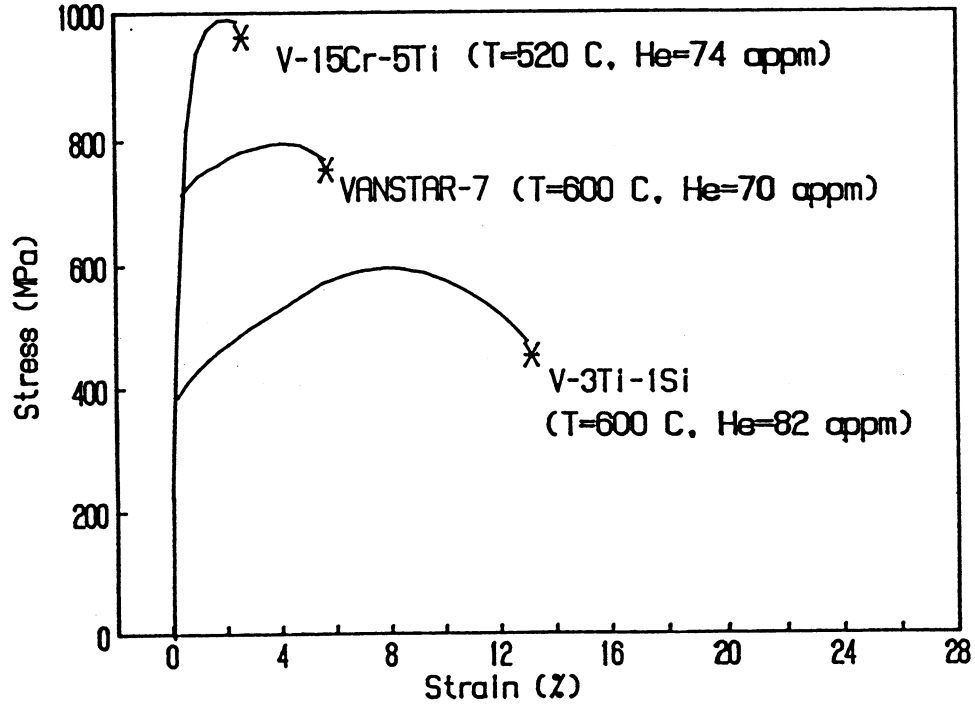

(b)

Fig. 8.2.-5. Unirradiated (a) and irradiated (b) stress-strain relations for three vanadium alloys.

the creep behavior based on the amount of helium retained coupled with the Orr-Sherby-Dorn (OSD) parametric method [12] are planned.

The BCSS has rated vanadium-based alloys to be least corrosive in liquid lithium compared with iron-based alloys. Furthermore, vanadium alloys do not show liquid-metal embrittlement in liquid lithium. Based on a radioactive mass transport limit of 0.5 μm/yr, the highest allowable vanadium/lithium operating temperature is 750 to 800°C. This mass transport limit as suggested by BCSS was adopted from 316 stainless-steel/sodium systems and may be overly stringent for vanadium/lithium systems.

The high cost of vanadium components necessitates that only the first wall and blanket be made out of vanadium-based alloys. The remainder of the coolant loop is made out of steel. Steels contain a large amount of nonmetallic additions such as C, N and O in solid solution. These nonmetallic impurities are leached from the steel by lithium through the formation of lithium compounds such as Li_3N, Li_2C_2, Li_2O. Since the carbides and nitrides of vanadium are thermodynamically more stable than those of lithium, the lithium will give up the carbon and nitrogen leached from the steel. The transfer of nonmetallic impurities between two different alloys in contact with the same coolant is generally referred to as the Bi-Metallic Impurity Pickup (BMIP) mechanism.

While some options promise to mitigate BMIP (see Sec. 8.2.2.2), certain nonmetallic impurity levels in liquid lithium have to be assumed. Recent experiments conducted on a V-3Ti-1Si and a Ti-stabilized ferritic steel loop with liquid lithium have shown favorable results [13]. The formation of a dense, adhesive and exposure time independent vanadium and titanium nitride layer (~ 2 to 5 μm) was observed which promises to be a barrier to complete bulk nitridation or carbonization of the reactor torus structure. Since these surface nitride layers are ceramics, they possibly will act as an electrical insulator to mitigate MHD pressure drops. However, the integrity of these layers in an irradiation environment remains to be investigated.

8.2.2.2. Piping

The BMIP issue plays a crucial role in determining the choice of material for liquid lithium piping outside the FPC. Ferritics are highly susceptible to decarbonization when in contact with liquid lithium. Addition of Ti and/or V to ferritics stabilizes their carbides. Austenitic steels, on the other hand, have more stable carbides than ferritics, but are more easily corroded in liquid lithium [14]. A protective layer, such as aluminum nitride (AlN), will protect

the steel from corrosion since AlN is stable in liquid lithium. Either one or a combination of the following options is available to mitigate BMIP: (1) use stabilized ferritic steels, or (2) use aluminized austenitic or ferritic steels for the remainder of the coolant loop.

Recent experimental findings show that stainless steel AISI 304 was only moderately attacked by highly purified liquid lithium at 550°C [15]. The material loss was measured to be not more than 2 μm/yr at a flow velocity of 70 mm/s. Although the experiments were conducted at low velocities, they indicate the feasibility of using steel piping outside the FPC.

8.2.2.3. Coatings

The chemical and electromagnetic environment of a fusion device may necessitate the use of coatings as chemical barriers or electrical insulators. Experiments have shown the formation and compatibility of nitride layers on steels and vanadium-based alloys in a liquid-lithium environment [13,15]. In addition to constituting a chemical interaction barrier, these nitride layers also act as hydrogen diffusion barriers and electrical insulators. This latter property is most useful in the electromagnetic environment of a liquid-metal-cooled fusion device because electrically insulating coatings minimize MHD pressure drops. While the formation of electrically insulating nitride layers on V-3Ti-1Si alloys in a liquid-lithium environment has been shown experimentally [13], the integrity of this layer in an irradiation environment is questionable. The behavior of the vanadium and titanium nitride layer under irradiation is not known at this time. Boron nitride (BN), for example, swells anisotropically, which leads to cracking. Assuming that vanadium and titanium nitrides also have hexagonal crystal structures, these compounds would behave similar to BN under irradiation. The self-healing process of the vanadium and titanium nitride layer however, may compensate for cracking and loss during operation. Because of the uncertainties in the stability of insulating layers under irradiation, the use of laminated insulation structures is also under study in order to reduce the MHD pressure drop.

8.2.2.4. Magnets

The critical issue regarding magnet lifetime is the increase in resistivity of the conductor and swelling of the insulation material in an irradiation environment. The response of insulating materials to neutron irradiation has a direct bearing on the shield thicknesses required. Coil shielding thicknesses

directly influence the reactor dimensions and mass. The insulating material, therefore, has a strong impact on the design and economic performance of the device. Special attention is being given to the development of design equations for the radiation response of candidate insulating materials such as magnesium alumina or spinel.

8.2.2.5. Materials Summary

The interaction of the irradiation, chemical, thermal, stress, and electromagnetic environments in a high-power-density compact device poses stringent performance criteria on materials. Quantification of lifetime performances is difficult not only because of the lack of sufficient data base in most aspects of material behavior, but also because fundamental processes have not yet been studied in detail. The development of phenomenological equations to determine material lifetimes, therefore, can only serve as first- order approximations until more experimental support becomes available.

Efforts are continuing to study the irradiation response of the vanadium alloy, V-3Ti-1Si; the corrosion effects of liquid lithium on this alloy; the stability and viability of electrical insulation coating materials in a liquid-lithium environment; and the radiation response of electrically insulating materials.

8.2.3. Neutronics

8.2.3.1. Scoping Studies

The base case considered in the scoping phase is described in Fig. 8.2.-6. The neutronics model for the lithium-vanadium design consists of a plasma zone in the center of the cylinder with a radius of 0.60 m. A 50 mm scrape-off region is located between the plasma and the first wall. The first-wall zone consists of three regions: 6 mm vanadium alloy, 10 mm 50% vanadium alloy and 50% lithium, and 10 mm vanadium alloy. Two lithium zones follow the first wall zone, which are 0.375 m thick each and are divided by a 5 mm separation plate made of vanadium. The lithium zones are followed by a 5 mm vanadium wall and a normal copper magnet. The neutronics performance of this base case blanket is summarized in Table 8.2.-IV.

Table 8.2.-IV shows the tritium breeding ratio and nuclear heating rate in the base case design. The tritium breeding ratio is 1.42, of which 0.524 is from the $^{7}Li(n,n'\alpha)T$ reaction in lithium. The nuclear energy deposited in the

TABLE 8.2.-IV

SUMMARY OF THE NUCLEAR PERFORMANCE OF THE LITHIUM-VANADIUM DESIGN

Tritium breeding (T/DT neutron):	
$^6Li(n,\alpha)T$	0.898
$^7Li(n,n',\alpha)T$	0.524
Tritium breeding ratio	1.42
Nuclear heating (MeV/DT neutron):	
First wall zone	1.69
Lithium zones	12.59
Total blanket nuclear heating	14.28
Nuclear heating in OH coils	2.58

blanket is about 14.3 MeV per DT neutron corresponding to a blanket energy multiplication M_n of 1.01. The nuclear energy leaking into the magnet is about 2.58 MeV per DT neutron, which is about 18% of the energy deposited in the blanket. The fast neutron flux (E_n > 0.1 MeV) at the magnet is estimated to be 10^{26} n/m^2/yr at 20 MW/m^2 neutron wall loading. This damage rate implies that the radiation lifetime of the magnet because of radiation-damage to the spinel insulator is four full-power years if the criterion given in Ref. 16 is used.

To improve the blanket energy multiplication and to increase the lifetime of the magnet, the base-case design was modified to employ a hot reflector/shield. Figure 8.2.-7 gives the schematic model of the modified design. The hot reflector/shield made of 10% lithium, 10% vanadium alloy, and balance of manganese steel, Fe1422, and is located between the lithium zone and the normal conducting magnets. A parametric study was performed varying the thicknesses of the lithium zone, the hot reflector/shield and the ^6Li content in lithium. The results are presented in Figs. 8.2.-8 to 8.2.-11.

Figure 8.2.-8 shows the fast neutron flux at the magnet as a function of total blanket/shield thickness and for several lithium zone thicknesses. The flux values are given at 20 MW/m^2 neutron wall loading. As shown in this figure, a lower fast neutron flux at the magnet can be obtained for a thinner lithium zone design, provided that the total blanket/shield thickness is kept constant. For a magnet design with a 30 full-power-year-lifetime, the required total blanket/shield thickness will be 0.70, 0.77, and 0.83 m with the lithium zone thickness of 0.4, 0.3, 0.2 m, respectively. Note these analyses were made

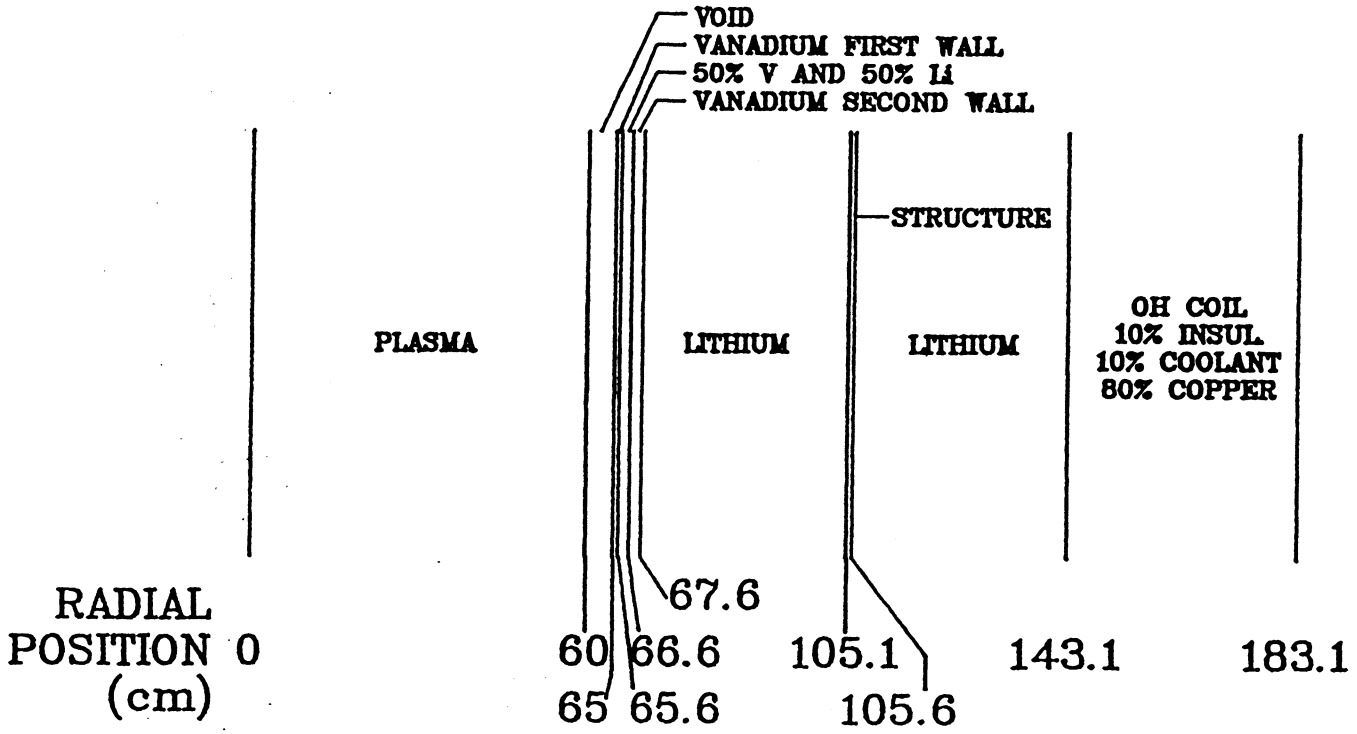

Fig. 8.2.-6. Schematic of the one-dimensional neutronics model for the base-case lithium-vanadium blanket design.

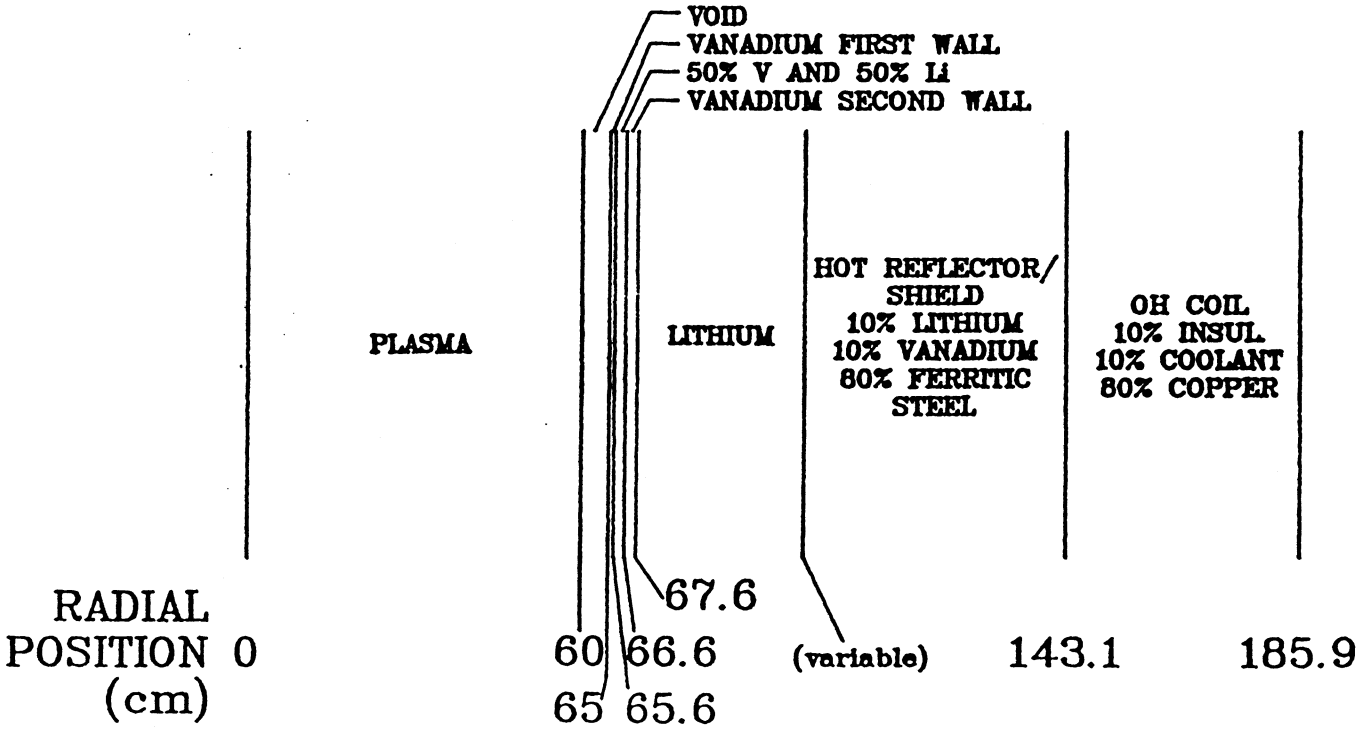

Fig. 8.2.-7. Schematic of the one-dimensional FPC neutronics model for the modified base-case design. The significant departure from the base case design is the inclusion of a hot reflector/shield between the lithium zone and the TF/OH magnets.

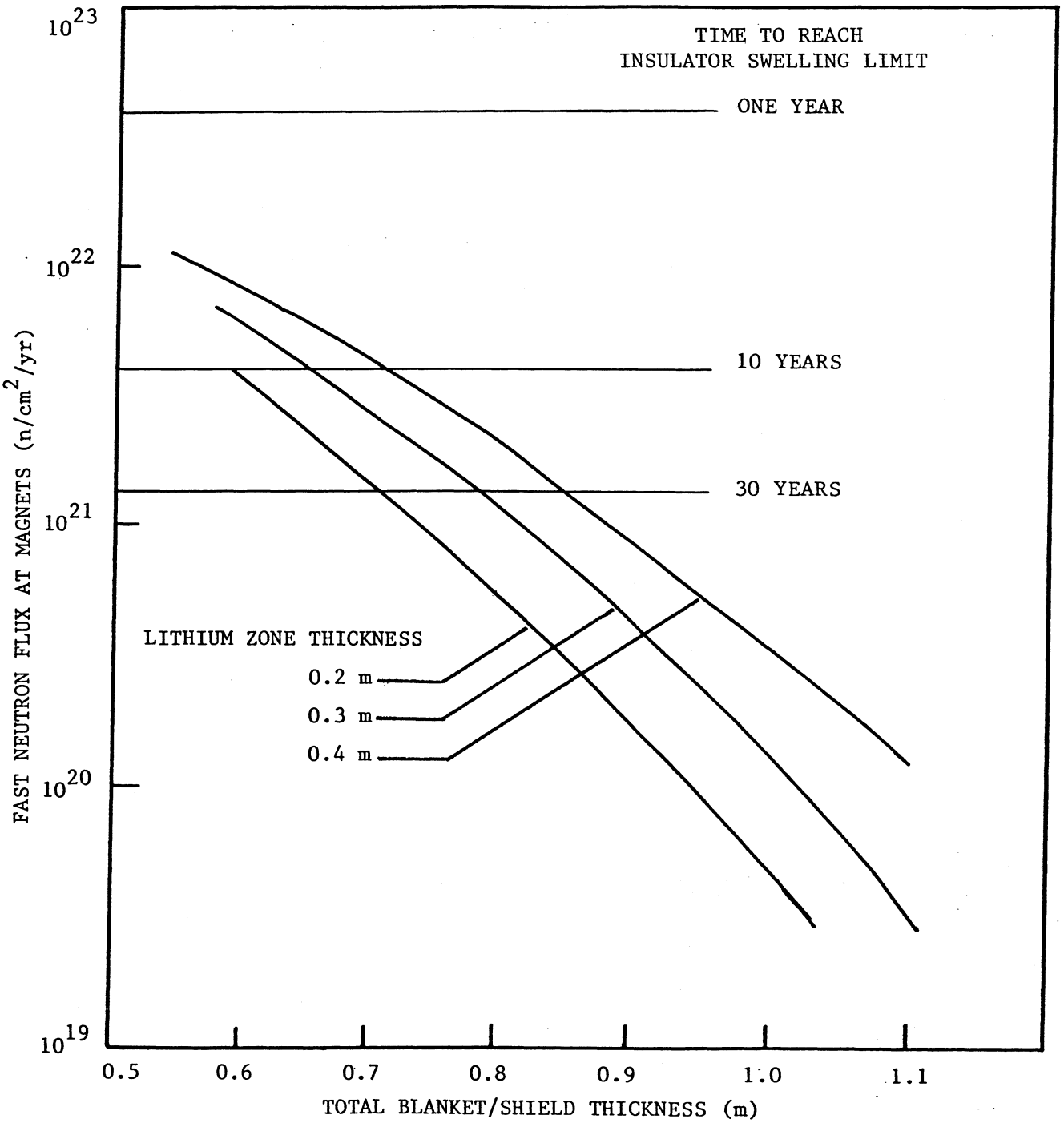

Fig. 8.2.-8. Fast neutron flux at the TF/OH magnets as a function of total blanket and shield thickness. The flux values are given for 0.2, 0.3 and 0.4 m thick lithium zone designs at 20 MW/m^2 neutron wall loading.

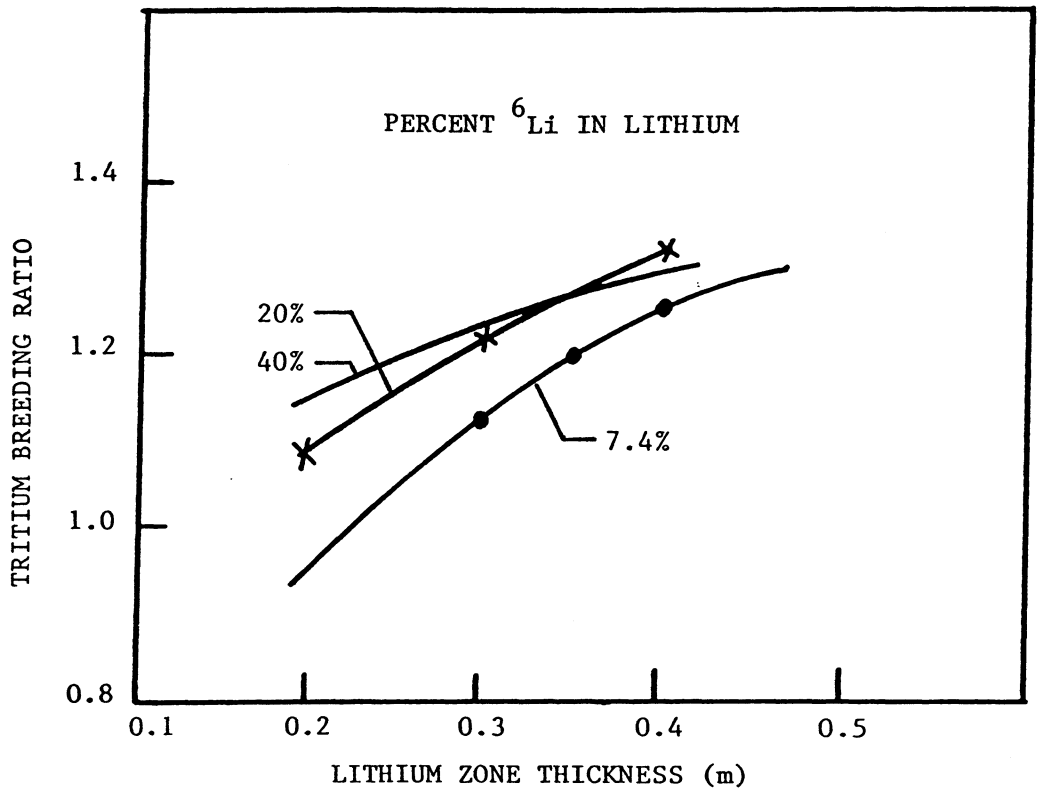

Fig. 8.2.-9. Tritium breeding ratio as a function of lithium zone thickness for the TITAN lithium-vanadium design with the total blanket/shield thickness fixed at 0.77 m. The tritium breeding ratios are given for several ^{6}Li enrichments in lithium, 7.4% (natural Li), 20% and 40%.

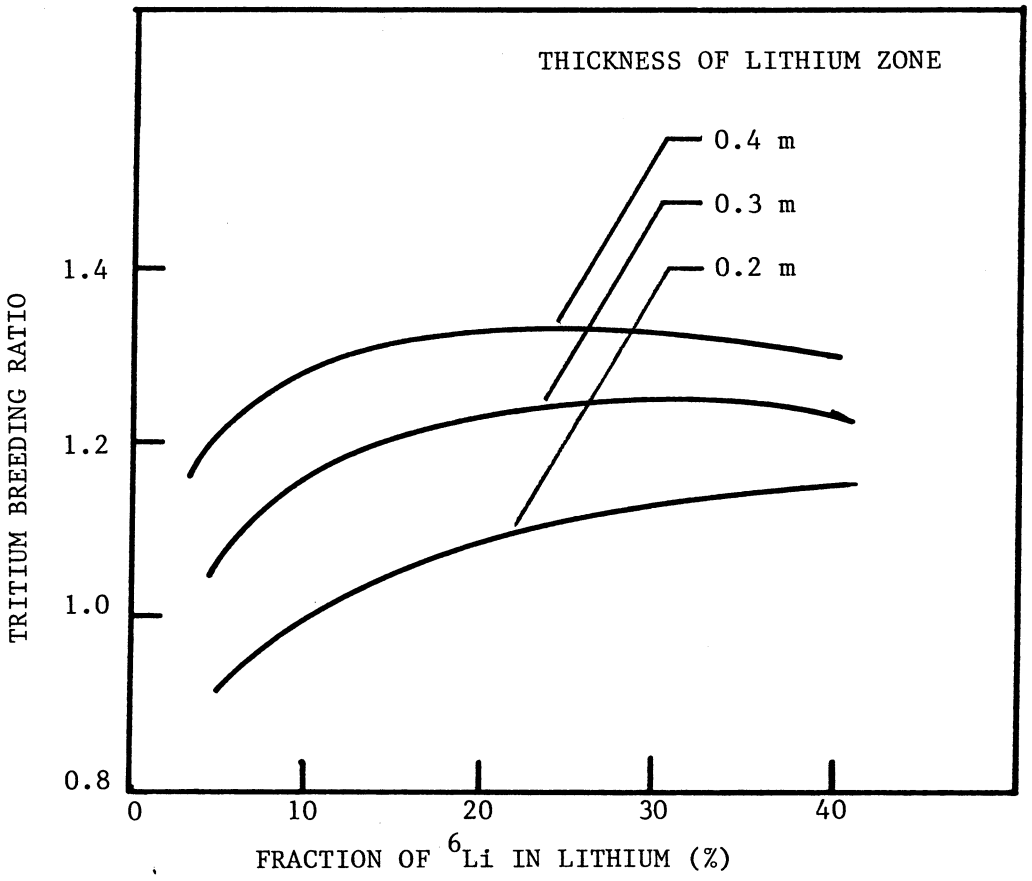

Fig. 8.2.-10. Tritium breeding ratio as a function of percent ^{6}Li in the lithium. The tritium breeding ratios are given for three lithium zone thickness designs: 0.2, 0.3, and 0.4 m. Note that the total blanket/shield thickness in these designs is fixed at 0.77 m.

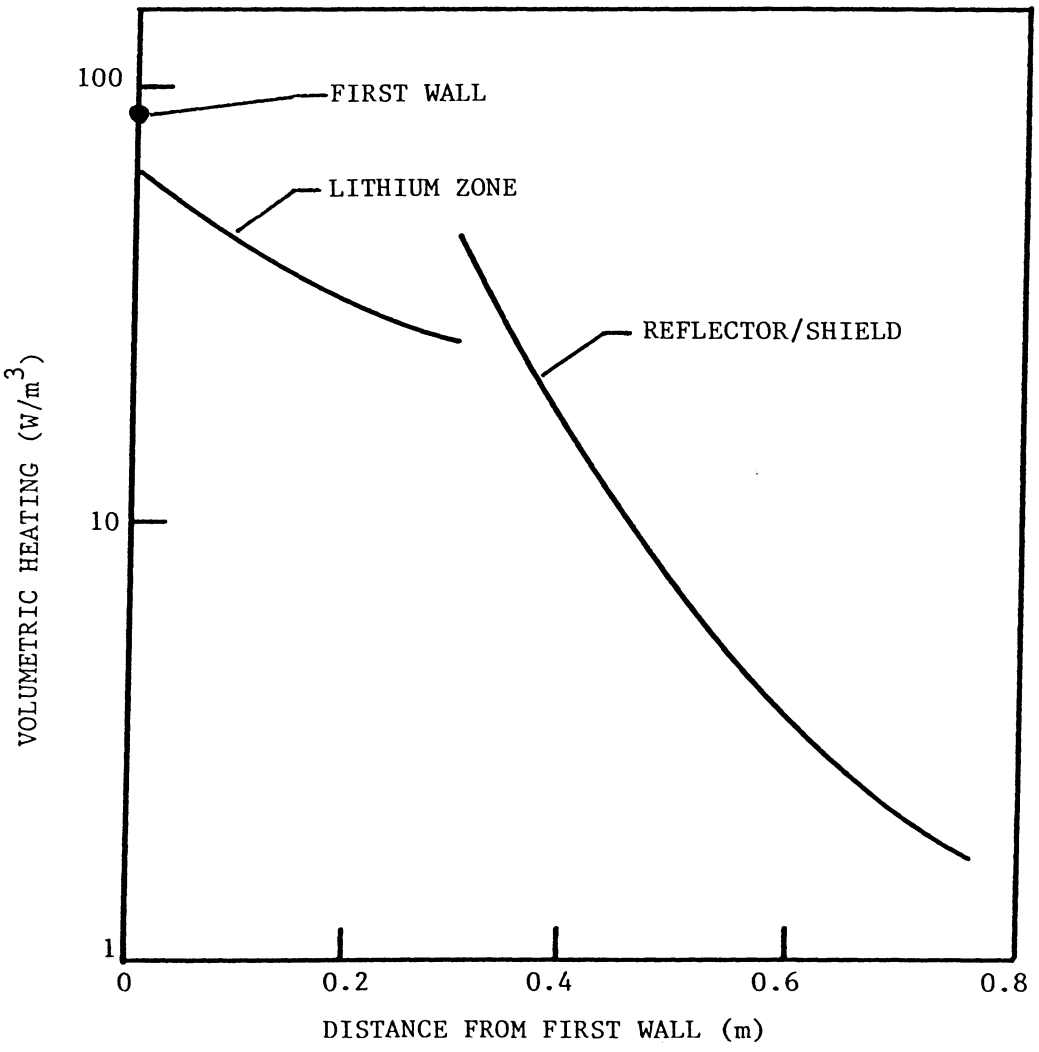

Fig. 8.2.-11. Nuclear heating distribution in the TITAN lithium-vanadium blanket design.

with the results from the design calculations employing natural lithium. When the lithium is enriched with ^{6}Li, the fast neutron fluxes at the magnet will be further reduced, hence giving a longer lifetime than estimated based on natural lithium designs.

The tritium breeding ratio as functions of lithium zone thickness and ^{6}Li enrichment in lithium is shown, respectively, in Figs. 8.2.-9 and 8.2.-10. In these two figures, the total blanket/shield thickness is kept constant at 0.77 m. Figure 8.2.-9 shows that the tritium breeding ratio will exceed 1.20 when the lithium zone is thicker than 0.25, 0.28, and 0.35 m, respectively, at 40%, 20%, and 7.4% (natural lithium) ^{6}Li in lithium. However, when the lithium zone thickness is reduced to 0.3 m, the minimum ^{6}Li content in lithium to obtain a tritium breeding ratio of no less than 1.2 would increase to 14% or more. At 0.2 m lithium zone thickness, a tritium breeding ratio in excess of 1.20, is probably not achievable, as is also shown in Fig. 8.2.-10. From the above discussions it appears that, within the total blanket/shield thickness constraint of 0.77 m, the design with a lithium zone thickness of 0.3 m and a ^{6}Li enrichment of 20% in lithium is a resonable reference case for more detailed engineering study of the blanket concept.

8.2.3.2. Reference Design Point

The nuclear performance of the reference design was explored in detail and is reported in this subsection. In these calculations the first wall zone was modified as: 1 mm vanadium alloy, 8 mm 20% vanadium alloy and 80% lithium, and 6 mm vanadium alloy. The modification was made to reflect an iterated design improvement in the first wall region.

Tritium breeding ratios and nuclear energy deposition rates in the reference design for 20% (enriched) and 7.4% (natural lithium) ^{6}Li in lithium are given in Table 8.2.-V. Results from both ANISN and MCNP calculations are compared in this table. The results from MCNP calculations, which are used as reference values, are statistically accurate to about 1%. Furthermore, the results from ANISN calculations are within about 3% of that calculated from MCNP, as shown in Table 8.2.-V. The significant difference occurs in the energy deposited in the magnets, where the ANISN calculations could underestimate the nuclear heating up to 50%.

Table 8.2.-V shows that the tritium breeding ratio for the case of 20% enriched ^{6}Li in lithium is about 1.29 and decreases to 1.21 when natural lithium is used. For the enriched Li case, the nuclear energy deposited in the

TABLE 8.2.-V

NEUTRONICS RESULTS FOR THE LITHIUM COOLED REFERENCE DESIGN.

PERCENT ^{6}Li IN LITHIUM:	20%		7.4%	
TRANSPORT CODE:	ANISN	MCNP	ANISN	MCNP
Tritium breeding (triton/DT neutron):				
^{6}Li(n,α)T	0.869	0.890	0.716	0.733
^{7}Li(n,n',α)T	0.391	0.404	0.458	0.475
Total TBR	1.250	1.294	1.174	1.208
Nuclear heating (MeV/DT neutron):				
First wall zone	0.86	0.88	0.87	0.89
Lithium zones	10.08	10.10	9.54	9.50
Reflector/shield	6.07	6.07	7.13	7.19
Total blanket/shield	17.01	17.06	17.54	17.57
Magnet nuclear heating	0.27	0.35	0.31	0.47

blanket/shield is about 17.1 MeV, which is equivalent to a blanket energy multiplication of 1.21. The blanket/shield nuclear heating rate in the system with natural lithium, however, is higher, about 17.6 MeV, corresponding to a blanket energy multiplication of 1.25. The nuclear energy deposited in the magnet behind the blanket/shield is about 0.35 MeV for the enriched Li case, however, this value increases to about 0.47 MeV if natural lithium is used.

The volumetric nuclear heating rate in the blanket/shield is depicted in Fig. 8.2.-11 as a function of distance from the first wall. The heating rate distribution is given for a neutron wall load of 20 MW/m^2. The heating rate is about 88 MW/m^3 at the first wall. The volumetric heating rate in the lithium zone immediately behind the first wall is about 63 MW/m^3 and falls off steadily to about 27 MW/m^3 in front of the reflector/shield zone. The maximum heating in the reflector/shield zone, occurs at the region close to the lithium zone and is 43 MW/m^3. The volumetric heating rate decreases as the location moves away from the lithium zone and is about 2 MW/m^3 at the end of the reflector/shield (45 cm from the lithium zone).

8.2.4. Thermal Hydraulics

8.2.4.1. Coolant Selection

The desirable features of the coolant are high thermal conductivity, high heat capacity, and compatibility with structural materials. Also, the coolant should improve, or at least should not degrade the blanket nuclear performance (i.e., tritium breeding ratio and energy multiplication). Furthermore, for a liquid-metal coolant, the electrical conductivity should be low enough so that the coolant pressure drop, caused mainly by the MHD effects, and the associated pumping-power are acceptable.

Of all the liquid metals, lithium has the largest specific heat capacity. Although sodium has slightly better electrical properties, the advantages of better thermal capacity of lithium outweigh its higher electrical conductivity. Liquid lithium combines the function of the coolant and the tritium breeder. Furthermore, liquid lithium is compatible with the proposed vanadium-alloy structural material (Sec. 8.2).

8.2.4.2. Thermal and MHD Analysis

In this section, a brief outline of the thermal and MHD analysis is presented. The results of this analysis are presented in the next section. The first wall consists of a bank of tubes,behind which are followed by blanket coolant channels. A diagram of the first wall and blanket coolant channels is given in Fig. 8.2.-2. As the poloidal magnetic field is much larger than the toroidal field, the coolant channels are aligned along the poloidal field to reduce the MHD pressure drop.

The thermal and MHD analysis is performed to determine the maximum structure temperature. Heat conduction in the first wall tube is assumed one-dimensional with a uniform heat flux equal to the maximum radiation heat flux, (q_o''') on the tube wall. Volumetric heat generation (q''') from nuclear heating in the tube wall is assumed uniform. The temperature distribution in the tube wall as a function of radial position, r, is given by:

$$T(r) = T_i + \left[\frac{q_o'''b}{k} + \frac{q'''b^2}{2k}\right] \ln\left(\frac{r}{a}\right) - \frac{q'''(r^2-a^2)}{4k}, \qquad (8.2.-1)$$

where T_i is the inner wall temperature, a is the inner radius, b is the outer

radius and k is the thermal conductivity. The actual heat flux on the tube wall varies along the circumference and can be approximated by a cosine distribution. Because of the strong variation of the film temperature drop along the circumference, a 2-D solution of the energy equation in the coolant has been obtained with a method similar to that used by Reynolds [17]. To incorporate the effect of the magnetic field on the coolant velocity profile, the following velocity profile has been assumed.

$$v(r) = \frac{m+2}{m}\,\bar{U}\left[1 - \left(\frac{r}{a}\right)^m\right], \qquad (8.2.-2a)$$

$$\bar{U} = \frac{2}{a^2}\int_0^a v(r)\, r\,dr \qquad (8.2.-2b)$$

where $\bar{U}$ is the average velocity. Large values of the power index, m, simulate a high Hartmann number, $H \equiv Bd_h(\sigma/\eta)^{1/2}$ where B is the magnetic field, d_h is the hydraulic diameter, σ is the electric conductivity and η is the liquid viscosity. The resulting film temperature drop as a function of circumferential angle, θ, is then given by,

$$\Delta T_f(\theta) = f(m)\int_0^{2\pi} q''(\theta')d\theta' - \frac{a}{\pi k}\int_0^{2\pi} q''(\theta')\,\ln\left[2\sin\left(\frac{\theta-\theta'}{2}\right)\right]d\theta', \qquad (8.2.-3a)$$

where

$$f(m) = \frac{a}{\pi k}\left[\frac{(m+2)^2-4}{4m(m+2)} - \frac{2(m+2)^2}{m^2}\left\{\frac{1}{16} - \frac{1}{(m+2)(m+4)} - \frac{1}{4(m+4)} + \frac{1}{2(m+2)^3}\right\}\right], \qquad (8.2.-3b)$$

and $q''(\theta')$ is the heat flux at the circumferential angle, θ', on the surface.

The coolant exit temperature and coolant flow rate are calculated from an energy balance. The blanket is treated as a single channel as the final blanket channel configuration has not yet been decided.

The coolant pressure drop includes both friction and MHD effects although the latter is the dominant contributor. The coolant flow paths for the first

wall and blanket coolant channels are shown schematically in Fig. 8.2.-12. The perpendicular magnetic-field strength varies along the inlet/outlet ducts (AB, CD, EF and GH), but is constant along the first wall tubes and blanket channels (BC and FG). Bends and contractions/expansions are located at B, C, F and G.

Analytical expressions for MHD pressure drop for flow in straight ducts in a uniform perpendicular magnetic field have been obtained by solving the Navier-Stokes and Maxwell's equations under the assumptions of high Hartmann number, high magnetic interaction parameter and low magnetic Reynolds number, $Re_m = \sigma v \mu d_h$ where σ is the electric conductivity, v is the velocity, μ is the magnetic permeability, and d_h is the hydraulic diameter [18,19,20]. These assumptions are generally valid in a fusion environment and allow the induced magnetic field to be neglected in Maxwell's equations and the inertia and viscous terms to be neglected in Navier-Stokes equation.

Hunt and Holroyd [21], and Hoffman and Carlson [22] have provided semi-empirical equations for MHD pressure drops for the cases of bends, inlet/outlet contractions and magnetic field gradient. The equations in Ref. 21 have been used to calculate the MHD pressure drops along the coolant paths shown in Fig. 8.2.-12. These equations are given in Table 8.2.-VI. In Table 8.2.-VI, $\Phi \equiv \sigma_w t_w/\sigma$, σ_w and σ are the electrical conductivity of the channel wall and the fluid, respectively, L is the flow length path, t_w is the thickness of the channel wall, u is the fluid velocity, and a is one half of the width of the coolant channel in the direction of B. Leakage paths for current in the coolant channels can seriously affect the MHD pressure drop [23]. Preliminary analysis has shown no leakage current effect for the coolant channel configuration used here.

The first-wall tubes will be subjected to high coolant pressure because the high coolant velocity required results in a large MHD pressure drop. Two-dimensional stress analysis of the coolant tubes has been performed. The primary stress is caused by the coolant pressure and is maximum at the entrance of a tube. The thermal or secondary stress is due to the temperature variation in the tube wall. The equations for these stresses are given by,

$$\sigma_{pr}(r) = \frac{a^2 p}{b^2 - a^2}\left(1 - \frac{b^2}{r^2}\right) \qquad (8.2.\text{-}4a)$$

A - Entrance

AB- Straight Duct

- Varying B-Field

B - Inlet/Contraction

- Bend

BC- Straight Tube

C - Bend, Expansion

CD- Straight Duct

- Varying B-Field

D - Expansion

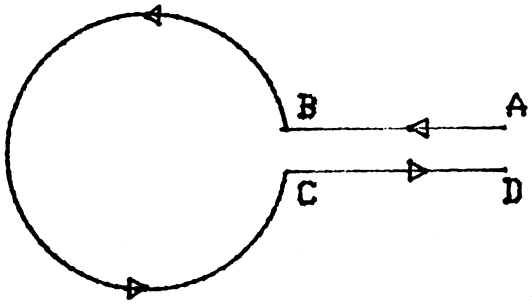

FW Flow Circuit

E - Entrance

EF- Straight Duct

- Varying B-Field

F - Inlet/Contraction

- Bend

FG- Straight Channel

G - Bend, Expansion

GH- Straight Duct

- Varying B-Field

H - Expansion

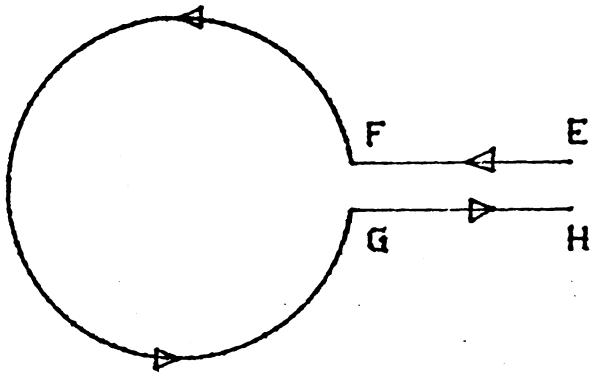

Blanket Channel Flow Circuit

Fig. 8.2.-12. Illustration of lithium flow paths for FIRST WALL and blanket.

TABLE 8.2.-VI
EQUATIONS FOR THE MHD PRESSURE DROP

1. Straight channel (Magnetic field component normal to flow)	$\Delta P = \sigma u B^2 L \frac{\Phi}{1+\Phi}$
2. Inlet/contraction	$\Delta P = 0.2\sigma u B^2 a \Phi^{1/2}$
3. Varying B-field	$\Delta P = 0.2\sigma u B^2 a \Phi^{1/2} + \sigma u B^2 L \frac{\Phi}{1+\Phi}$
4. Bend, one leg normal to B-field	$\Delta P = \sigma u B^2 a \Phi^{1/2}$
5. Bend, both legs normal to B-field	$\Delta P = 0$

$$\sigma_{p\theta}(r) = \frac{a^2 p}{b^2 - a^2}\left(1 + \frac{b^2}{r^2}\right) , \qquad (8.2.-4b)$$

where σ_{pr} and $\sigma_{p\theta}$ are the radial and circumferential components, respectively, of the pressure stress, and

$$\sigma_{tr}(r) = \frac{\alpha E}{r^2}\left[\frac{r^2 - a^2}{b^2 - a^2}\int_a^b T(r)rdr - \int_a^r T(r)rdr\right] \qquad (8.2.-5a)$$

$$\sigma_{t\theta}(r) = \frac{\alpha E}{r^2}\left[\frac{r^2 - a^2}{b^2 - a^2}\int_a^b T(r)rdr + \int_a^r T(r)rdr - T(r)r^2\right] , \qquad (8.2.-5b)$$

where σ_{tr} and $\sigma_{t\theta}$ are the radial and circumferential components, respectively, of the thermal stress.

The equivalent stresses are:

$$\sigma_{eq,p}(r) = \left[\frac{1}{2}(\sigma_{pr} - \sigma_{p\theta})^2 + \sigma_{pr}^2 + \sigma_{p\theta}^2\right]^{1/2} \qquad (8.2.-6a)$$

$$\sigma_{eq,t}(r) = \left[\frac{1}{2}(\sigma_{tr} - \sigma_{t\theta})^2 + \sigma_{tr}^2 + \sigma_{t\theta}^2\right]^{1/2}, \qquad (8.2.-6b)$$

where r is the radius, θ is the angle along the circumference, a is the inner radius, b is the outer radius, E is Young's modulus and α is the coefficient of linear thermal expansion of the tube material. The temperature distribution in the tube wall (Eq. 8.2.-1) is T(r), and p is the coolant pressure. A more accurate description is given by a complete 2-D temperature distribution that includes the effect of poloidal curvature of the coolant tubes. A detailed thermo-mechanical analysis is discussed in Sec. 8.2.6. Similar analysis will be performed for the blanket channels later.

8.2.4.3. Thermal-Hydraulic Design Window

In this section, the results of design calculations are cast in the form of design windows. The logic and sequence of the calculations are shown in the flow chart in Fig. 8.2.-13. The results presented here are for the 18 MW/m^2 neutron wall loading design. The relevant reactor parameters and the limiting design values are shown in Table 8.2.-VII. The TITAN reactor operates with a highly radiative plasma (Sec. 4). A key parameter, f_{RAD}, has been defined as the ratio of the radiation losses to the total losses from the plasma. For the 18 MW/m^2 reference case, the heat flux on the first wall is roughly

TABLE 8.2.-VII

REACTOR PARAMETERS USED FOR PRELIMINARY MHD ANALYSIS

R = 3.9 m	η_{th} = 0.4
a_w = 0.65 m	Blanket thickness = 0.775 m
B_p = 6 T at first wall	$T_{w,max}$ = 750 °C
= 3 T at back of blanket	T_{in} = 300 °C
B_T = 0.36 T	$\sigma_{p,design}$ = 100 MPa
P_{th} = 2866 MW	$\sigma_{s,design}$ = 300 MPa
M = 1.33	t = 1.5 mm
d_i = 8 mm	

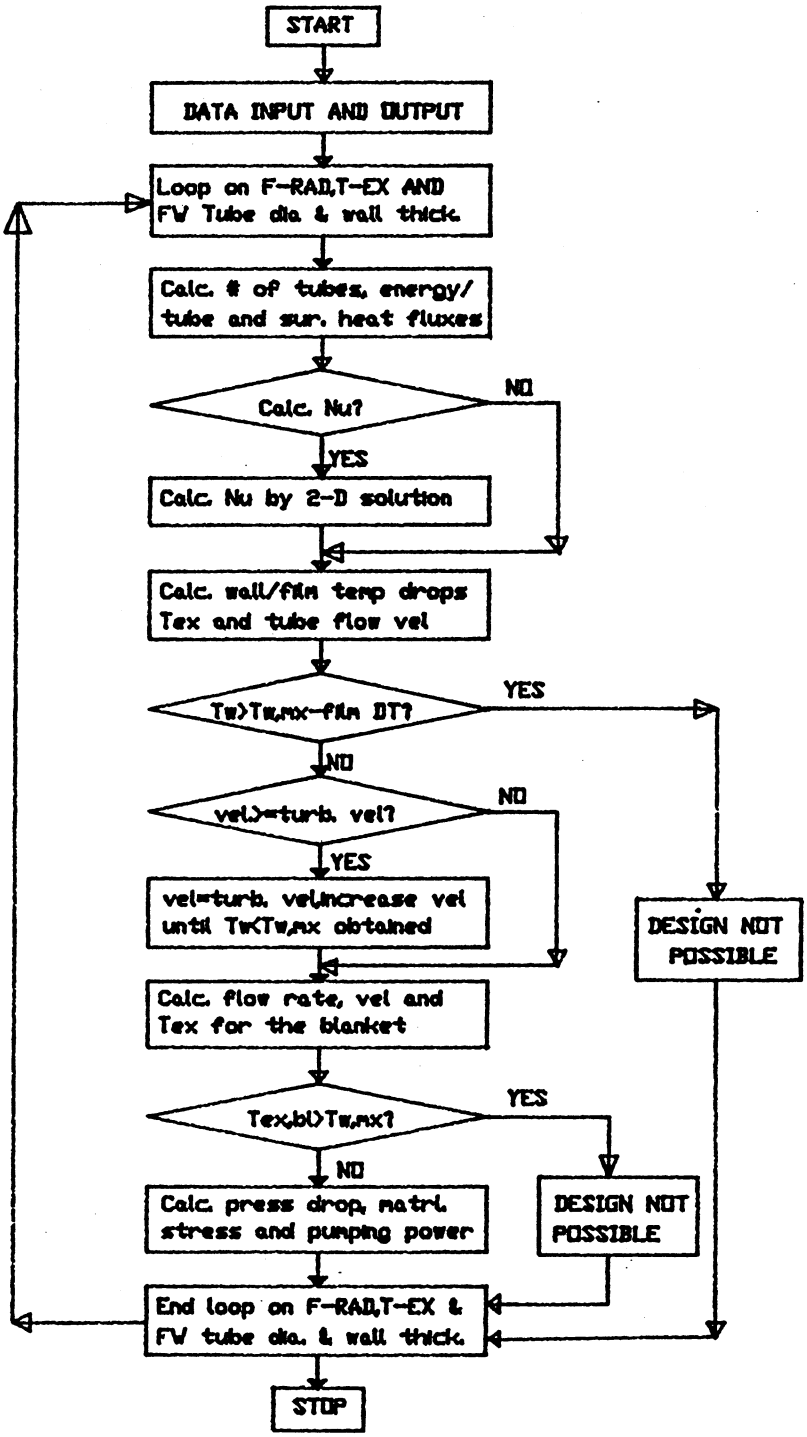

Fig. 8.2.-13. Flow chart of the calculation steps for the MHD analysis.

$4.5 \times f_{RAD}$ MW/m^2. For the purpose of the scoping phase, it was assumed that f_{RAD} can be varied in order to determine the maximum heat-flux limitation of the first wall.

Fig. 8.2.-14 shows the coolant pressure increment above the exit pressure for 3.6 MW/m^2 (f_{RAD} = 0.8) of heat flux on the first wall tubes. The maximum pressures at the inlets of the first wall loop (point A) and blanket flow loops (point E) are 8.4 MPa and 1.2 MPa, respectively. Using electrical insulation in the inlet/outlet ducts makes the pressure drops in the ducts (AB, CD, EF and GH) negligible. In this case the maximum pressures are 8 MPa and 0.6 MPa for the first wall and blanket flow loops, respectively. The large pressure drop in the first wall tubes is caused by the high coolant velocity necessary to remove the high surface heat flux.

The maximum equivalent stresses in the first wall tubes are shown in Fig. 8.2.-15 as a function of heat flux (or f_{RAD}). Even at a surface heat flux of 4.0 MW/m^2 (f_{RAD} = 0.9), the stresses are below the allowable design stress, which for vanadium alloys are taken as 100 MPa for primary stress and 300 MPa for secondary or thermal stress.

Figure 8.2.-16 shows the design window plotted in terms of T_{EXIT} and the surface heat flux. The upper line shows the maximum coolant exit temperature possible without exceeding the maximum allowable V-alloy temperature, which is taken as 750°C based on the recommendation in BCSS [6]. The lower limit on T_{EXIT} is determined by the limit of 5% of the gross electric power recirculated for pumping. Using electrical insulation in the inlet/outlet ducts lowers the lower limit on T_{EXIT} and enlarges the design window. The curves for the stress limit are below the pumping power limit curves and, hence, do not affect the design window. This design window shows that the first wall can be effectively cooled by lithium up to a heat flux of 4.5 MW/m^2 (f_{RAD} = 1.0). A coolant exit temperature of more than 500°C can be obtained, which results in good thermal efficiency. This conclusion is in contrast to the results of previous reactor studies, which have placed a much lower limit on the surface heat flux with liquid metal cooling [6].

Removal of high surface heat fluxes in the TITAN design is possible for two reasons; (a) use of turbulent flow when necessary and (b) two different exit temperatures for first wall and blanket flow loops and then mixing them to obtain the desired average exit temperature. The transition to turbulent flow is possible in the RFP reactor configuration because of the low perpendicular magnetic field, 0.36 T. The onset of turbulence occurs at about 20 m/s.

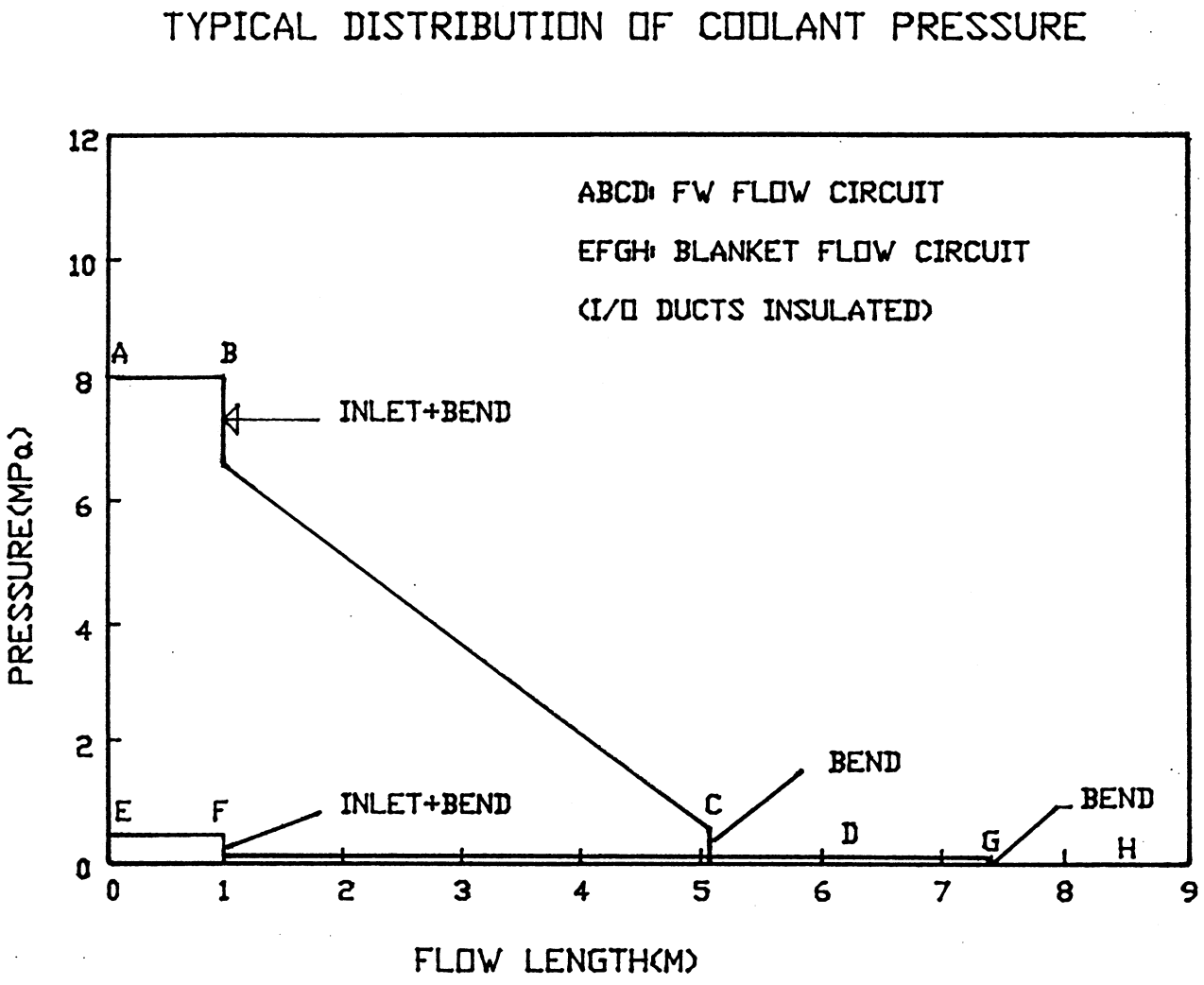

Fig. 8.2.-14. Coolant pressure along the length of the first-wall and blanket channels.

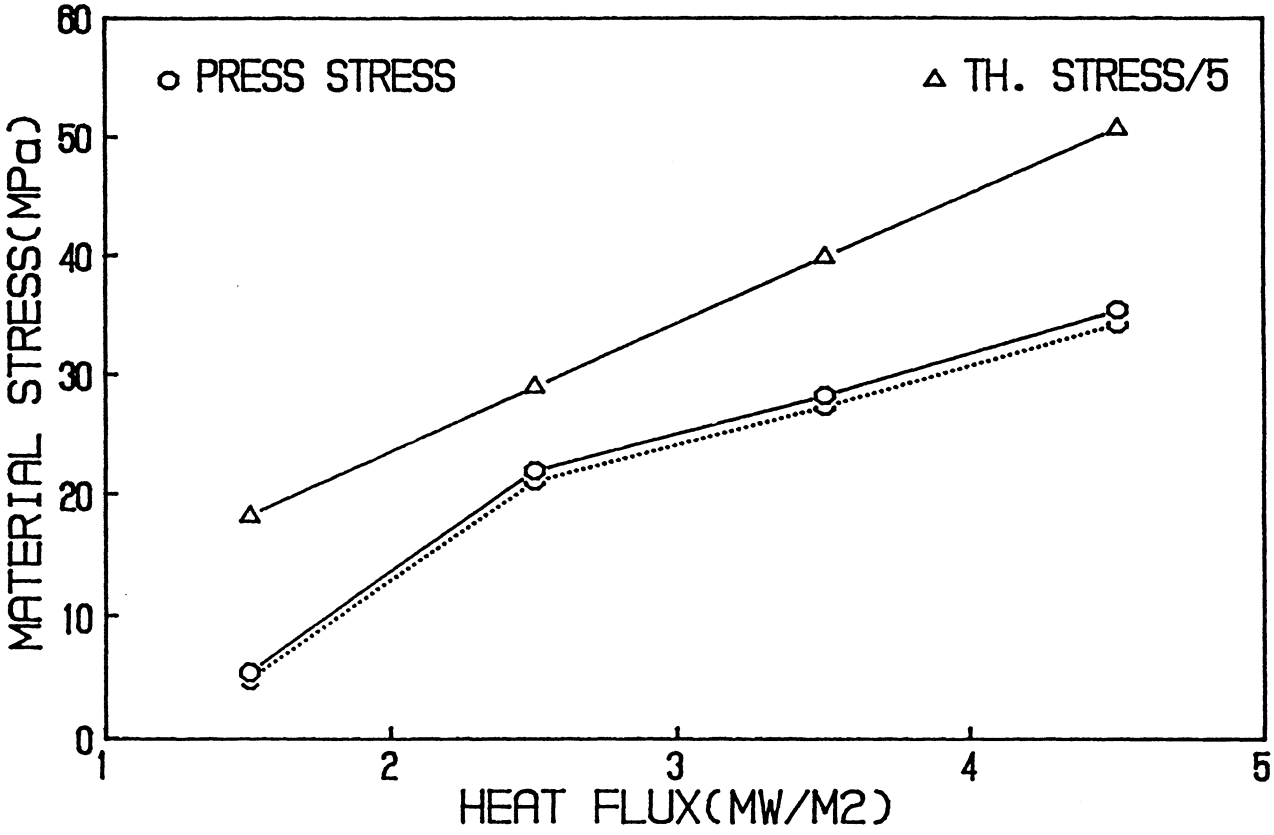

Fig. 8.2.-15. Stress in first wall tubes as a function of incident surface heat flux.

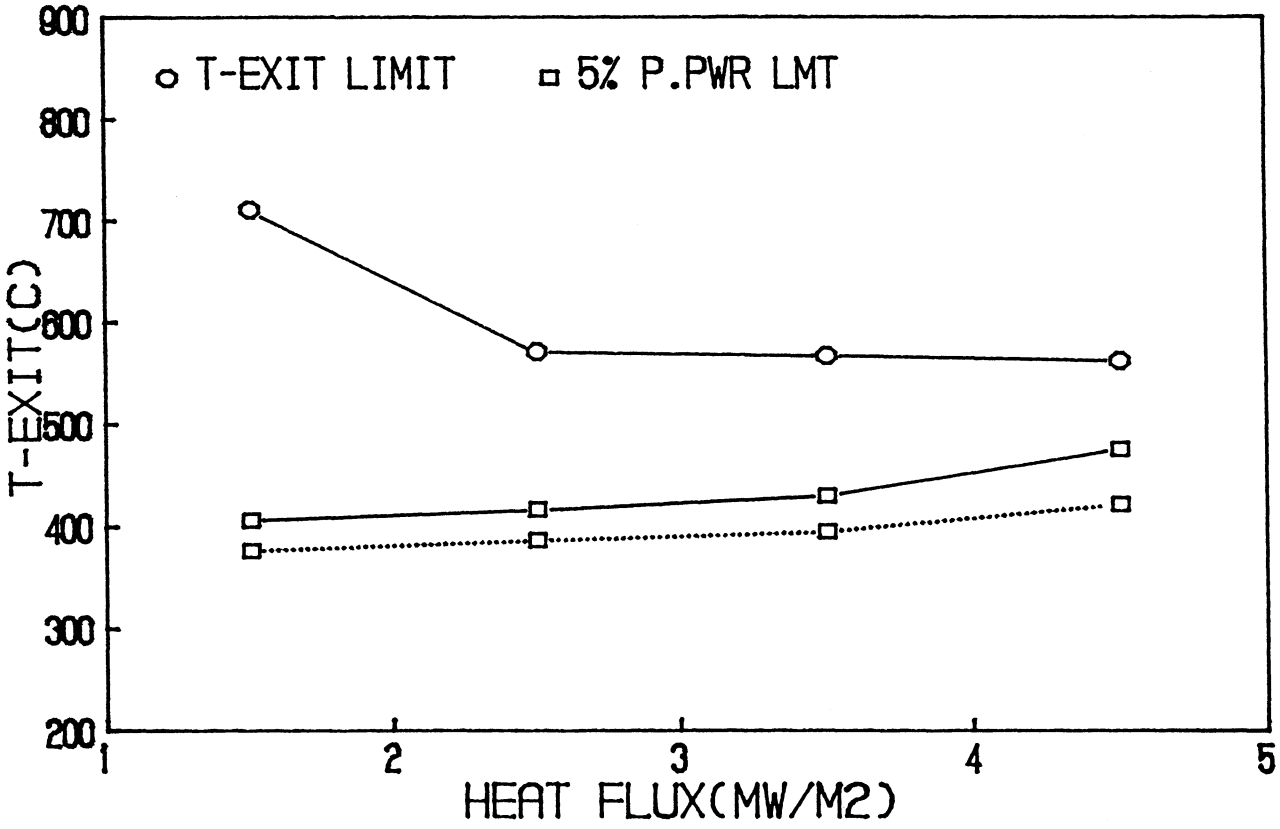

Fig. 8.2.-16. First wall and blanket design window with different exit temperatures from the first wall and blanket.

Fig. 8.2.-17 shows the design window for the case of no mixing or equal exit temperatures for both the first wall and blanket flow loops. For this case, the limiting heat flux on the first wall is about 2.3 MW/m^2 (f_{RAD} = 0.5).

8.2.4.4. Conclusions

The MHD and thermal-hydraulic analysis of the first wall and blanket for the 18 MW/m^2 TITAN reactor design shows that liquid-lithium cooling is feasible even with a first wall heat flux as high as 4.5 MW/m^2 (f_{RAD} = 1.0). Several reasons lead to this highly encouraging result: (a) the dominant field in a RFP is in the poloidal direction, while the coolant flows across the much weaker toroidal field (0.36 T); (b) separate flow loops for the first wall and blanket are used; (c) provisions are made for different coolant exit temperatures for the first wall and blanket loops and subsequent mixing, and (d) turbulent flow is used where necessary. Liquid-metal cooling allows operation with a high coolant exit temperatures (>500°C), which results in a high thermal power cycle efficiency of about 40%.

Work in several areas is ongoing. Detailed MHD and thermal hydraulic analysis of the blanket will be considered shortly. Additional MHD analysis, including 2-D and 3-D investigations as well as spatial variation of volumetric heating in the blanket, is planned. Although thermal considerations dictate the use of a thin first wall, consideration must be given to the erosion rate anticipated from plasma sputtering.

8.2.5. Integrated-Blanket-Coil (IBC)

One of the unique features of the lithium-vanadium blanket design is the integration of the breeding blanket and the toroidal field coils into a single component. The Integrated-Blanket-Coil (IBC) [5] concept combines the blanket functions of tritium breeding and energy recovery with the coil function of magnetic field production in a single component. Several benefits anticipated from adopting the IBC approach are listed as follows:

1. Simplification of the FPC by combining the function of two components into a single unit.

2. Shielding normally required for copper toroidal field (TF) coils is no longer needed.

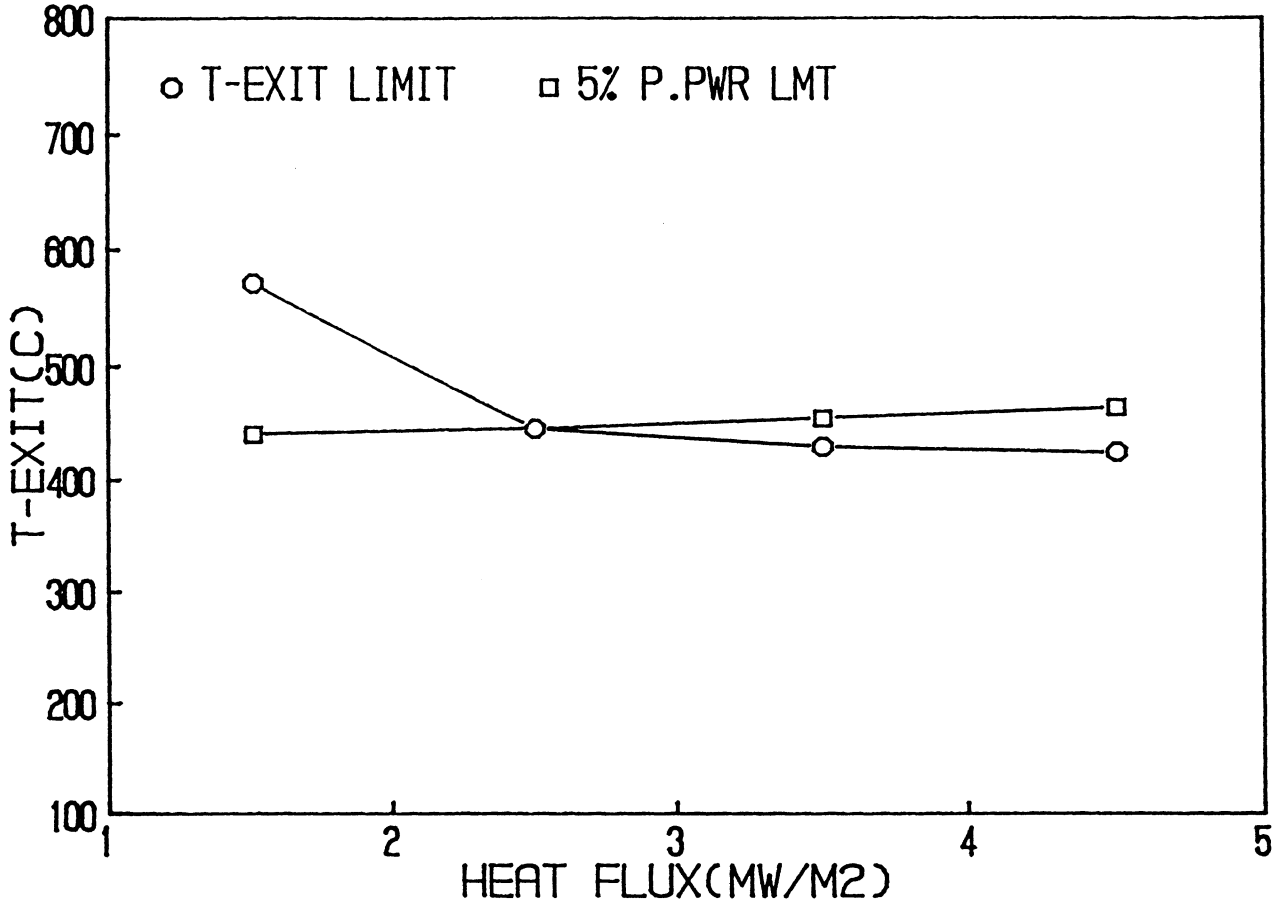

Fig. 8.2.-17. The design window for the first wall and blanket with equal exit temperatures.

3. Easier access for maintenance to first wall and blanket because TF coils need not be removed.

4. Reduced toroidal-field ripple because of the full coverage coil design.

Possible drawbacks to the IBC concept are as follows:

1. High-current, low-voltage power supplies are required. These power supplies can be quite large and the associated bussing connections may be cumbersome.

2. Trade-offs between thermal-hydraulic flow paths and electrical flow paths need to be addressed.

3. Field errors produced in the vicinity of the current connections should be minimized.

The IBC concept is illustrated schematically in Fig. 8.2.-18. The simplest configuration is dictated by the hydraulic flow path, which results in a single-turn TF coil. The current required per coil (16 coils per torus) is 480 kA and is driven through the main lithium channel in the blanket. Typical operating parameters for the TF IBC are listed in Table 8.2.-VIII.

Although the electrical resistivity of liquid lithium is about 20 times that of copper, the resistance of the IBC is comparable to that of the normal copper TF coils. The comparable resistance results because of a larger cross sectional area for current flow (lower current density) and a shorter current length because of the smaller minor radius of the IBC coils. The Joule losses in the IBC coil set are 16 MW, as compared with 34 MW in the copper TF coils. In addition, the power loss in the IBC can subsequently be recovered in the thermal energy conversion cycle resulting in a net power loss of 9.6 MW, not accounting for losses in the bussing which may be appreciable.

The most serious drawback to the IBC concept is the need for high-current, low-voltage power supplies (480 kA, 2 V/coil). After accounting for losses associated with leakage current in the headers and resistive losses in the

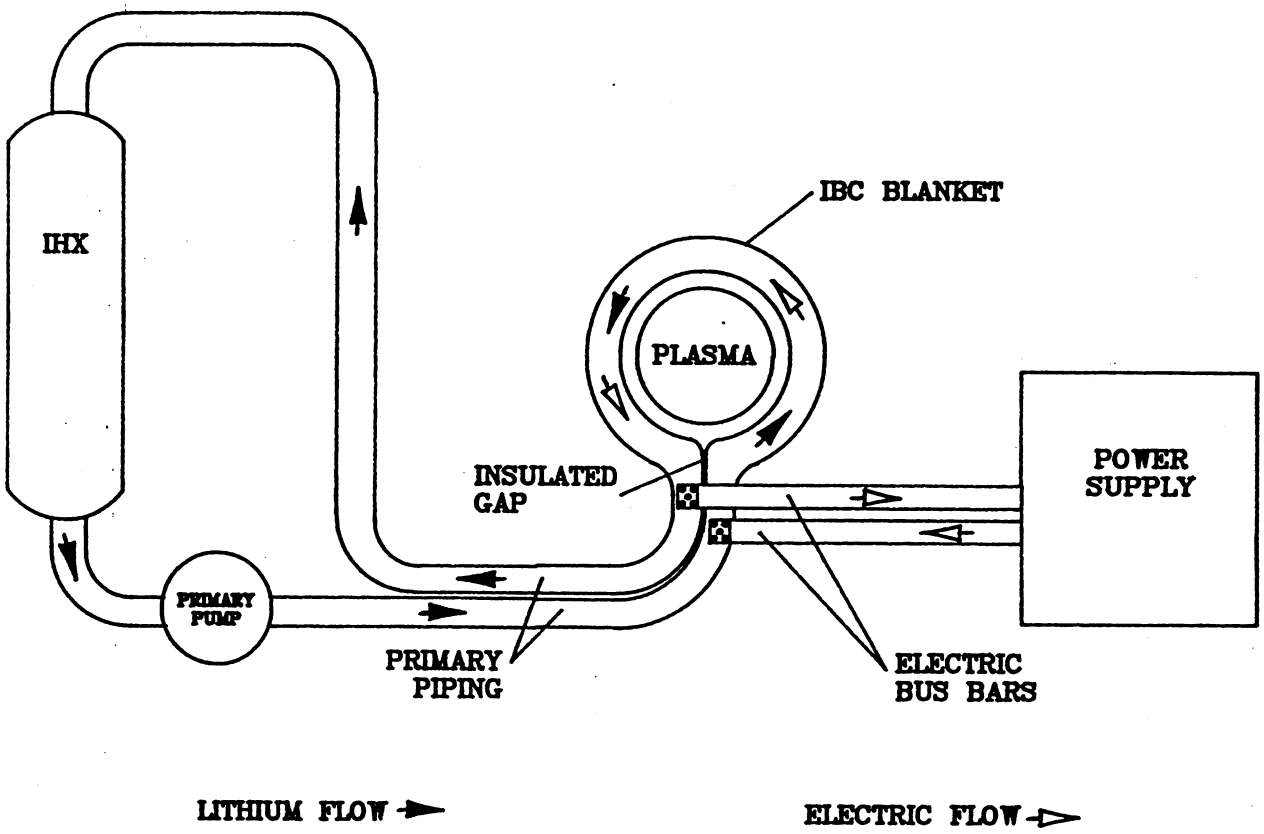

Fig. 8.2.-18. Illustration of the IBC concept.

TABLE 8.2.-VIII

PRELIMINARY IBC TOROIDAL FIELD COIL PARAMETERS

Total current (MA-turns)	7.5
Number of single turn coils	16
Current per coil (kA)	470.
Voltage drop per coil (V)	2
Number of coils per power supply	4
Power supply characteristics[a]	
Voltage (V)	18.
Current (kA)	600.
Power (MW_e)	10.8
Cost (M$)	7.1

[a] including losses in the bussing and the coolant headers.

bussing, the power-supply requirement for each loop is 600 kA at 18 V. Four of these power supplies are required.

Large 18-V/60-kA rectifier modules can be constructed with conventional components. To provide 600 kA, ten modules must be connected in parallel. The cost for four power supplies and the required bussing would be 28 M$. An alternative to the conventional power supply is to use motor driven homopolar generators (HPGs). Because the HPGs can be located closer to the machine than the rectifier power supplies, 12 V/quadrant is required instead of 18 V. Medium size HPGs have been built for short pulse application. No reason could be identified why a water-cooled steady state generator could not be built for this application. The breakeven cost for these generators is estimated at $885/kW. An accurate estimate af the cost of the motor driven HPGs cannot be made because the large steady state HPG must be developed for this application. It is possible that this power supply could be developed and produced for substantially less than $885/kW, which would make HPGs the more attractive power-supply option.

The trade-offs between the thermal-hydraulic flow path and the electrical current path are being investigated. To reduce the Joule losses through the primary loop piping and components, the blanket coolant inlet and outlet should be at the same electrical potential. Such a configuration is illustrated in Fig. 8.2.-19a. The disadvantages with this flow geometry are as follows:

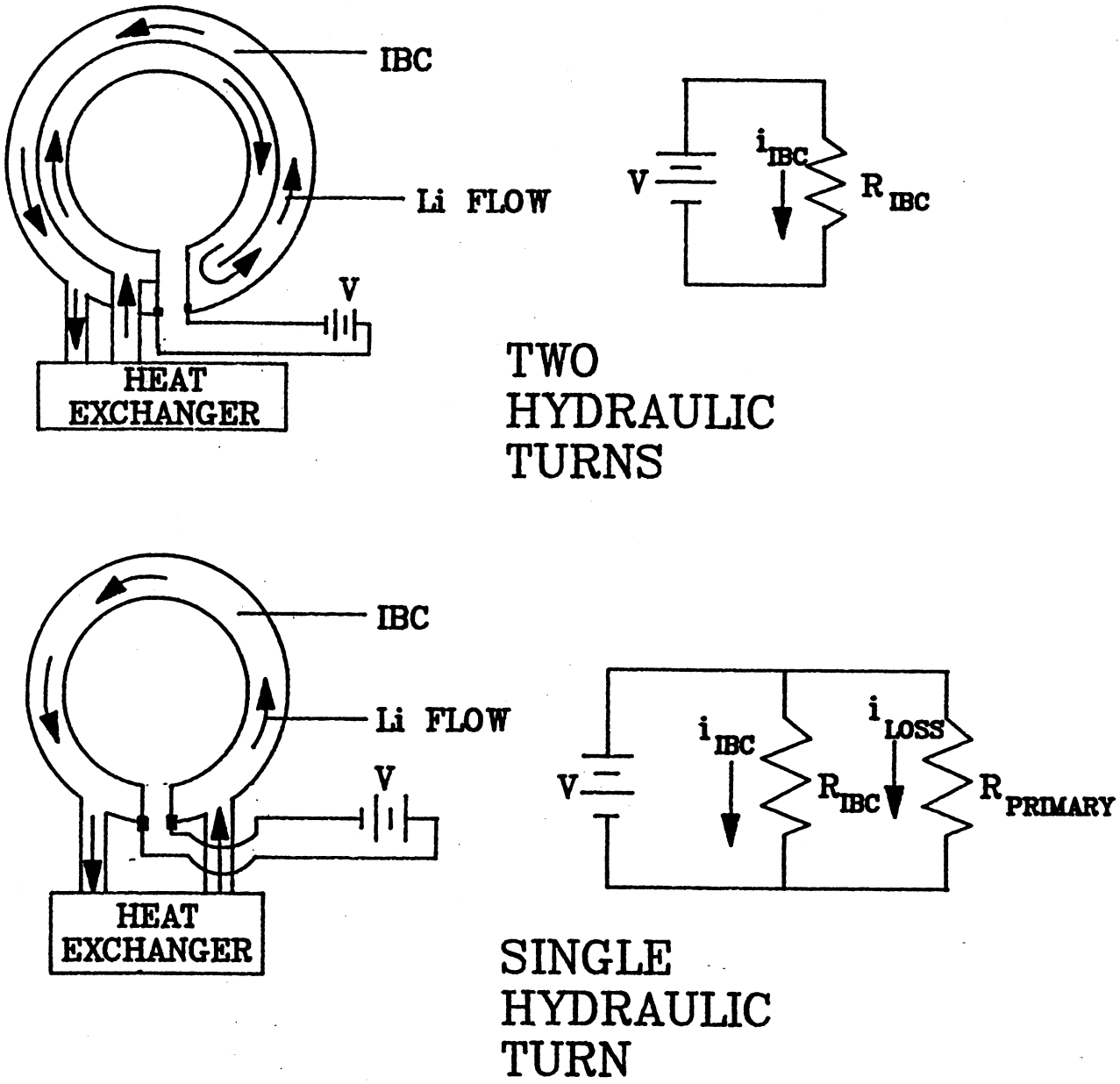

Fig. 8.2.-19. Two options for the hydraulic and electrical arrangement of the IBC circuit.

1. The flow must make two poloidal passes, which requires a coolant velocity that is twice as high as that in a single pass configuration. The higher velocity results in larger friction and MHD pressure drops.

2. An additional bend in the flow path is necessary. The bend, as discussed in Sec. 8.2.4, is a large contributor to the MHD pressure drop.

The preferred layout from a thermal hydraulic viewpoint is a single poloidal pass design as shown in Fig. 8.2.-19. This layout has an electrical loss associated with current leakage through the primary loop. Grounding of the primary loop before the IHX and after the primary coolant pumps will be necessary to prevent current flow through these components. Locating the current leads close to the blanket and increasing the electrical resistance of the primary loop will reduce the leakage current to an acceptable level. The present design has primary-loop electrical losses equal to about 10% of the power consumed in the IBC. Further study of the IBC concept is ongoing. Research is required in areas such as electrical grounding requirements, power supply development, and electrical current lead attachment methods.

8.2.6. Structural Analysis

8.2.6.1. Thermo-mechanical Analysis of the First Wall

The first wall geometries and loading conditions suggest that both the thermal and mechanical fields will exhibit significantly smaller gradients in the poloidal direction than in the radial and/or toroidal directions. A two-dimensional modeling of the cross section at the location of the extreme value of the loading in the poloidal direction, therefore, is appropriate. This approach has been used in several analyses [6,24], but the assumptions involved were not clearly indicated or were overly conservative. One possible reason for the conservatism is the virtual invariance of the temperatures and, to a lesser degree, the pressure stresses to the assumptions for structures with large radius of curvature. The thermal stresses, however, exhibit more pronounced dependence on the modeling.

The six components of the strain tensor for small deformations, ε_{ij}, in the Cartesian coordinate system are given in terms of the displacements as follows:

$$\varepsilon_{ij} = \frac{1}{2}\left[\frac{\partial u_i}{\partial x_j} + \frac{\partial u_j}{\partial x_i}\right], \qquad (8.2.-7)$$

where x_i (i=1,2,3) represents a Cartesian coordinate system and u_i denotes the displacements. If certain assumptions regarding the behavior in a direction are considered, the number of independent stress and strain components can be decreased significantly.

Plane-Strain Assumptions. The displacement components shown on Fig. 8.2.-20 are assumed to have the following form:

$$u_1 = u(x,y) \qquad (8.2.-8a)$$

$$u_2 = v(x,y) \qquad (8.2.-8b)$$

$$u_3 = w = 0 \; . \qquad (8.2.-8c)$$

These assumptions describe exactly a situation when a cylinder of arbitrary length is entirely constrained from axial movement and the deformation is independent of the axial dimension.

$$\varepsilon_{xx} = \frac{\partial u}{\partial x} \; , \quad \varepsilon_{yy} = \frac{\partial v}{\partial y} \; , \quad \varepsilon_{xy} = \frac{1}{2}\left[\frac{\partial u}{\partial y} + \frac{\partial v}{\partial x}\right] \; . \qquad (8.2.-9)$$

The constitutive equations including thermal strains are:

$$\varepsilon_{ij} = \frac{1}{E}\left[(1+\nu)\sigma_{ij} - \nu\sigma_{kk}\right] + \alpha T \qquad (8.2.-10a)$$

$$\sigma_{kk} = \sigma_{xx} + \sigma_{yy} + \sigma_{zz} \; , \qquad (8.2.-10b)$$

where σ_{ij} is the stress tensor, E is the Young's Modulus, α is the thermal expansion coefficient and T is based on some reference temperature. From Eq. (8.2.-10) the following expression results:

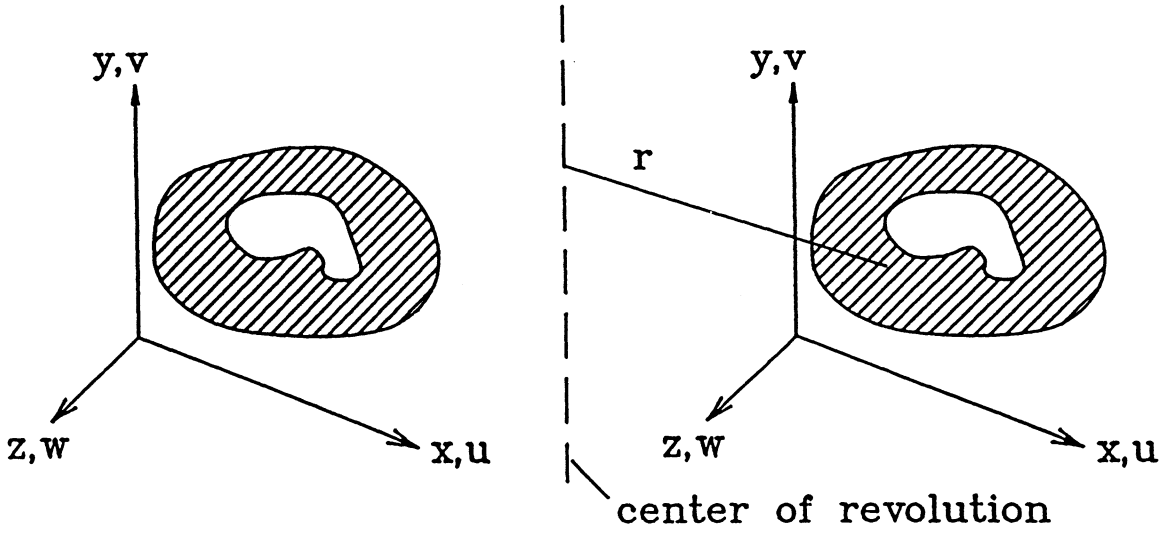

Fig. 8.2.-20. Displacement components.

$$\varepsilon_{zz} = \frac{1}{E}\left[(1+\nu)\sigma_{zz} - \nu(\sigma_{xx} + \sigma_{yy} + \sigma_{zz})\right] + \alpha T = 0 \ , \qquad (8.2.-11)$$

which yields

$$\sigma_{zz} = \nu(\sigma_{xx} + \sigma_{yy}) - E\alpha T \ . \qquad (8.2.-12)$$

If equivalent properties $E' = E/(1-\nu^2)$, $\nu' = \nu/(1-\nu)$ and $\alpha' = \alpha(1+\nu)$ are introduced, then the constitutive equations assume the following form:

$$\varepsilon_{xx} = \frac{1}{E'}(\sigma_{xx} - \nu'\sigma_{yy}) + \alpha' T \qquad (8.2.-13a)$$

$$\varepsilon_{yy} = \frac{1}{E'}(-\nu'\sigma_{xx} - \sigma_{yy}) + \alpha' T \qquad (8.2.-13b)$$

$$\varepsilon_{xy} = \frac{1+\nu'}{E}\sigma_{xy} \ . \qquad (8.2.-13c)$$

Additional mechanical field equations include equilibrium and compatibility equations.

Plane-Stress Assumptions. These assumptions approximately correspond to the behavior of a thin disk that is free of loading at the flat ends:

$$u_1 = u(x,y) \qquad (8.2.-14a)$$

$$u_2 = v(x,y) \qquad (8.2.-14b)$$

$$\sigma_{zz} = \sigma_{xz} = \sigma_{yz} = 0 \ . \qquad (8.2.-14c)$$

The tractions have to vanish there, which is exactly the condition given in Eq. (8.2.-18). Since the disk is thin, the variation of these stress components must be small compared with the in-plane stresses. The strains for small deformations are the same as those in Eq. (8.2.-9).

$$\varepsilon_{xx} = \frac{1}{E} (\sigma_{xx} - \nu\sigma_{yy}) + \alpha T \qquad (8.2.-15a)$$

$$\varepsilon_{yy} = \frac{1}{E} (\sigma_{yy} - \nu\sigma_{xx}) + \alpha T \qquad (8.2.-15b)$$

$$\varepsilon_{xy} = \frac{1 + \nu}{E} \sigma_{xy} \qquad (8.2.-15c)$$

$$\varepsilon_{zz} = - \frac{\nu}{E} (\sigma_{xx} - \sigma_{yy}) + \alpha T \ . \qquad (8.2.-15d)$$

Comparing these expressions with Eqs. (8.2.-13) shows that the in-plane quantities of a plane-strain problem can be obtained by solving the corresponding plane-stress problem with the equivalent properties. The out-of-plane stress component can be calculated from Eq. (8.2.-12). For thermal problems in toroidal fusion applications the out-of-plane forces can be high, since the αE product ranges from 1 to 3 for the structural materials considered, and the temperature difference between the current and the reference temperature can exceed 300°C.

Axisymmetric Deformation Assumptions. The displacements are assumed to be given by:

$$u_1 = u = u(x,y) \qquad (8.2.-16a)$$

$$u_2 = v = v(x,y) \qquad (8.2.-16b)$$

$$u_3 = w = 0 \ . \qquad (8.2.-16c)$$

The remaining strain components from Eq. (8.2.-7), expressed in the cylindrical coordinate system, are as follows:

$$\varepsilon_{xx} = \frac{\partial u}{\partial x} \ , \quad \varepsilon_{yy} = \frac{\partial v}{\partial y} \ , \quad \varepsilon_{xy} = \frac{1}{2} \left[\frac{\partial u}{\partial y} + \frac{\partial v}{\partial x} \right] \ , \quad \varepsilon_{zz} = \frac{u}{r} \ . \qquad (8.2.-17)$$

There are four stress components. The out-of-plane stress is not zero, and its value is generally less than that obtained from a plane strain analysis of the same plane section under the same loading conditions. If the geometry and the loading of the structure considered is nearly axisymmetric, then the modeling should also be axisymmetric. Plane-stress modeling underestimates, whereas plane strain formulation overestimates the out-of-plane stress component.

Since the structural material is metallic, the relevant uniaxial stress measure is the von Mises stress, which is given by

$$\sigma_{eq} = \left[0.5 \left((\sigma_1 - \sigma_2)^2 + (\sigma_2 - \sigma_3)^2 + (\sigma_3 - \sigma_1)^2\right)\right]^{1/2} , \qquad (8.2.-18)$$

where σ_1, σ_2 and σ_3 are the principal stresses. Yielding in metals has been observed to occur as a result of distortion and not volume change; therefore, the equivalent stress is based on the equality of the distortional strain energy due to the given three-dimensional stress state and the distortional energy due to the uniaxial equivalent stress. Note that a hydrostatic state produces zero equivalent stress.

In this section the results obtained from plane-stress and axisymmetric analyses are discussed. Pressure stresses as well as thermal stresses are calculated. The geometry analyzed is a circular tube with inner diameter of 8.0 mm, outer diameter of 11.0 mm, and radius of curvature of 0.65 m. The internal pressure is 7.4 MPa. Two cases of thermal loadings are considered, uniform heat flux and one-sided heating emanating from the center of curvature. In both cases the peak heat flux is 3.65 MW/m^2, the internal heat-generation rate is 115 MW/m^3, the fluid bulk temperature is 398 °C and the Nusselt number is 10.5. The calculations were performed using ANSYS, a general purpose finite-element code [25]. The cross section of the first-wall tube shown in Fig. 8.2.-21a was modeled employing symmetry. The boundary conditions for the thermal and mechanical analyses are explained on Fig. 8.2.-21b.

Pressure Stresses. The in-plane pressure stresses exhibit the same axial symmetry within the tube cross section in both plane-stress and axisymmetric analyses. The effect of poloidal curvature appears only in the presence of a near constant poloidal stress. The maximum equivalent stress is 28 MPa in the plane-stress analysis and 26.7 MPa in the axisymmetric analysis. The latter

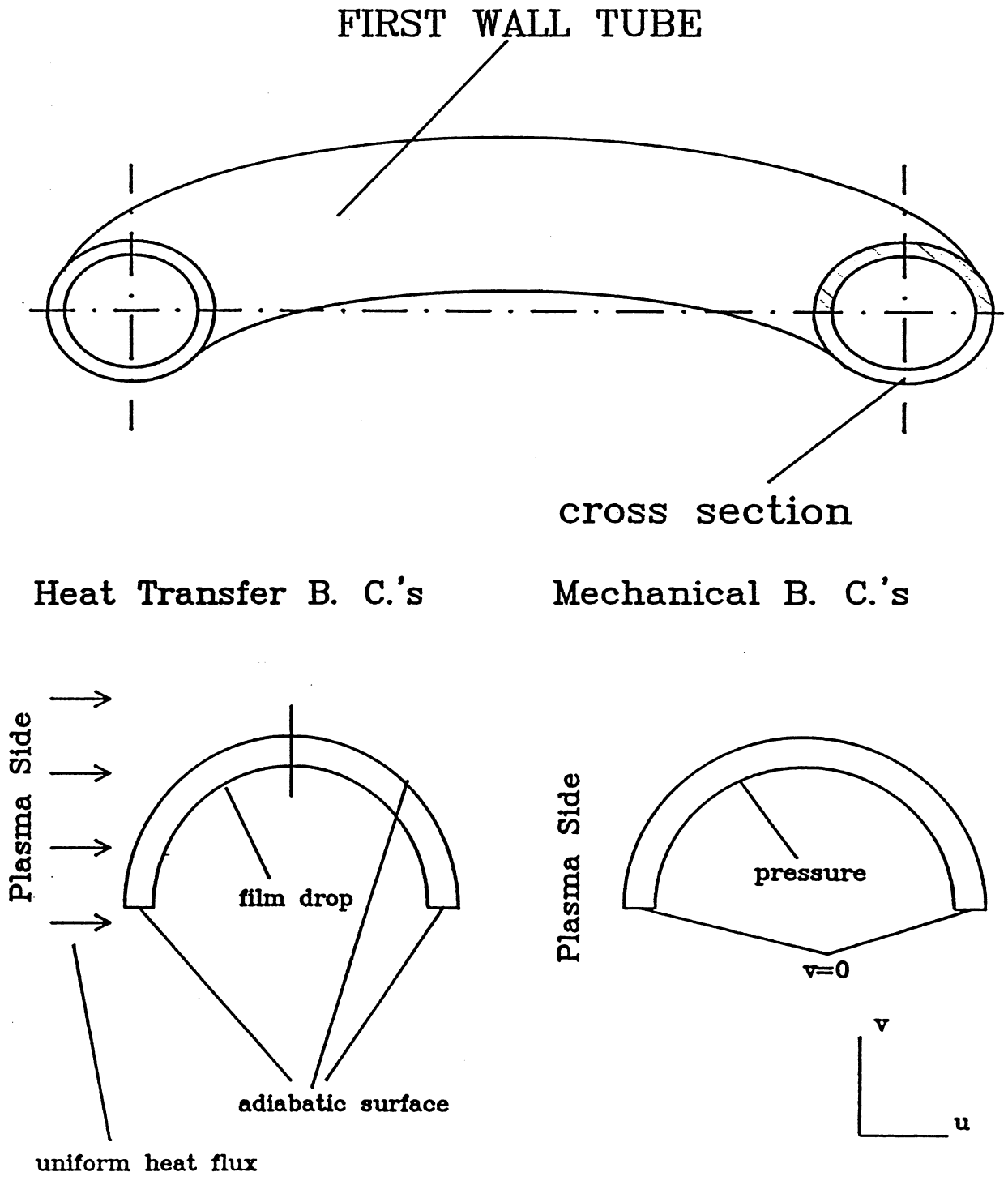

Fig. 8.2.-21. Model of first wall tube with thermal and mechanical boundary conditions.

stress is lower, since the curvature produces tensile stresses in the poloidal direction, and the stress state becomes closer to a hydrostatic state.

Temperatures - Uniform Heat Flux. The axisymmetric and two dimensional heat transfer analyses gave approximately the same maximum temperature of 677°C occurring at the outer perimeter and minimum temperature of 471°C at the inner wall surface. The large radius of curvature caused only a slight asymmetry in the thermal field.

Thermal Stresses - Uniform Heat Flux. The axisymmetric and the plane-stress results are significantly different. The plane-stress values are axisymmetric within the tube cross section and show good agreement with the exact results. The maximum equivalent stress is 129 MPa, which occurs at the points of the highest temperature, while the minimum stress is 14 MPa at the inner radius. The axisymmetric analysis showed that the highest stress component is the poloidal stress, which by assumption is set to zero in the plane-stress results. The source of these stresses arises from the condition of axisymmetry, which ensures no motion out of the plane of the cross section. This condition induces compressive out-of-plane stresses in the high-temperature zone and tensile stresses in the cold zone. Coupling between the in-plane and poloidal stresses makes the in-plane stresses higher in the axisymmetric case than in the plane stress case. Consequently, the maximum equivalent stress is 129 MPa at the outer radius, and the minimum stress is 13.8 MPa at the inner radius for the plane-stress model, with the maximum and minimum stresses being 200 MPa and 21.1 MPa, respectively, in the axisymmetric case.

Temperatures - One-Sided Heating. With less total heat transmitted to the tube, the maximum temperature and the temperature drop across the wall are lower than in the uniform-heat-flux case. The temperature contours in Fig. 8.2.-22 show asymmetry and are from the axisymmetric analysis. The two-dimensional results are very close to those given in Fig. 8.2.-22, and show the weak dependence of the thermal field on the fairly large radius of curvature. The maximum temperature of 662°C occurs at the point closest to the plasma, and the minimum temperature of 398°C is at the point farthest from the plasma at the inner radius.

Thermal Stresses - One-Sided Heating. Similar effects to those in the uniform heating can be observed. Fig. 8.2.-23 shows the equivalent stresses in the plane-stress model, Fig. 8.2.-24 gives the stress contours of the poloidal stresses and Fig. 8.2.-25 depicts the equivalent stresses resulting from the axisymmetric analysis. The asymmetry of the temperature field causes

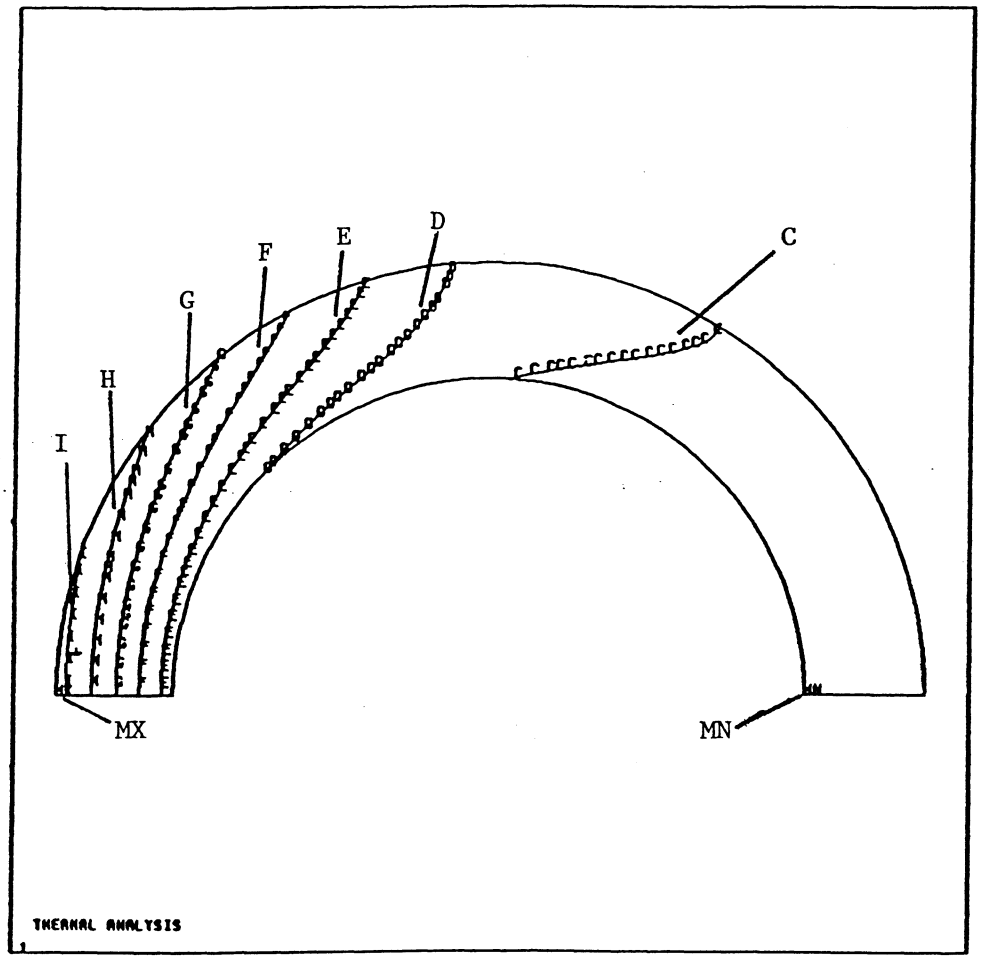

TEMPERATURE CONTOURS (K)

C=680	F=800
D=720	G=840
E=760	H=880
MN=671	I=920
MX=935	

Fig. 8.2.-22. Temperature contours in the first wall of the lithium design.

significant poloidal stresses with contours resembling the temperature contours. The maximum and minimum stresses are 88.3 MPa and 0.3 MPa in the plane-stress model, and 235 MPa and 11.5 MPa in the axisymmetric model, respectively.

While ignoring the poloidal stresses when calculating the pressure stresses does not cause significant errors and proved to be conservative, the thermal stresses develop entirely differently in a thin disk and in an axisymmetric structure. Plane stress results still give a good idea about the magnitude of the stresses but have to be treated cautiously due to their nonconservative nature. Also, the asymmetric temperature distribution due to one-sided heating raises the stress level even further.

Summary. Assuming 100 MPa allowable value for the primary stresses and 750°C maximum wall temperature for the vanadium alloy, all structural design criteria are satisfied and the current design is feasible. Future analysis will address the effect of the poloidally varying coolant temperature and possible methods to relieve some of the poloidal thermal stresses.

8.2.6.2. Structural Analysis of the Lithium Blanket

In this section the pressure stresses in the lithium blanket are calculated using the finite element method. Initially, a baseline configuration is chosen, and simplifying assumptions are made so the structure can be modeled with 2-D axisymmetric elements. Subsequently, the blanket dimensions are varied to reduce the bending stresses at the corners and to study the effects of possible design changes. Finally, the likely effects of the pending thermo-structural analysis are discussed.

In order to perform a 2-D axisymmetric analysis the toroidal curvature and poloidal break at the inlet/outlet header must be ignored. The resulting model is shown in Fig. 8.2.-26, where toroidal symmetry is assumed so only half of the blanket needs to be modeled. The analysis was performed with the ANSYS finite-element code [25], using 484 nodes and 360 elements. The baseline model dimensions and material properties are given in Table 8.2.-IX.

For the baseline module dimensions and a uniform pressure of 1.5 MPa, the maximum equivalent stress occurred on the outside surface at the center of the side plate and was 398 MPa. The major components of this stress are a hoop stress of -175 MPa and a large bending stress of -470 MPa. Obviously, this design requires modification.

Before discussing any design modifications, the baseline blanket is used to study the effect of increasing the outlet pressure to 2 MPa. In this case the

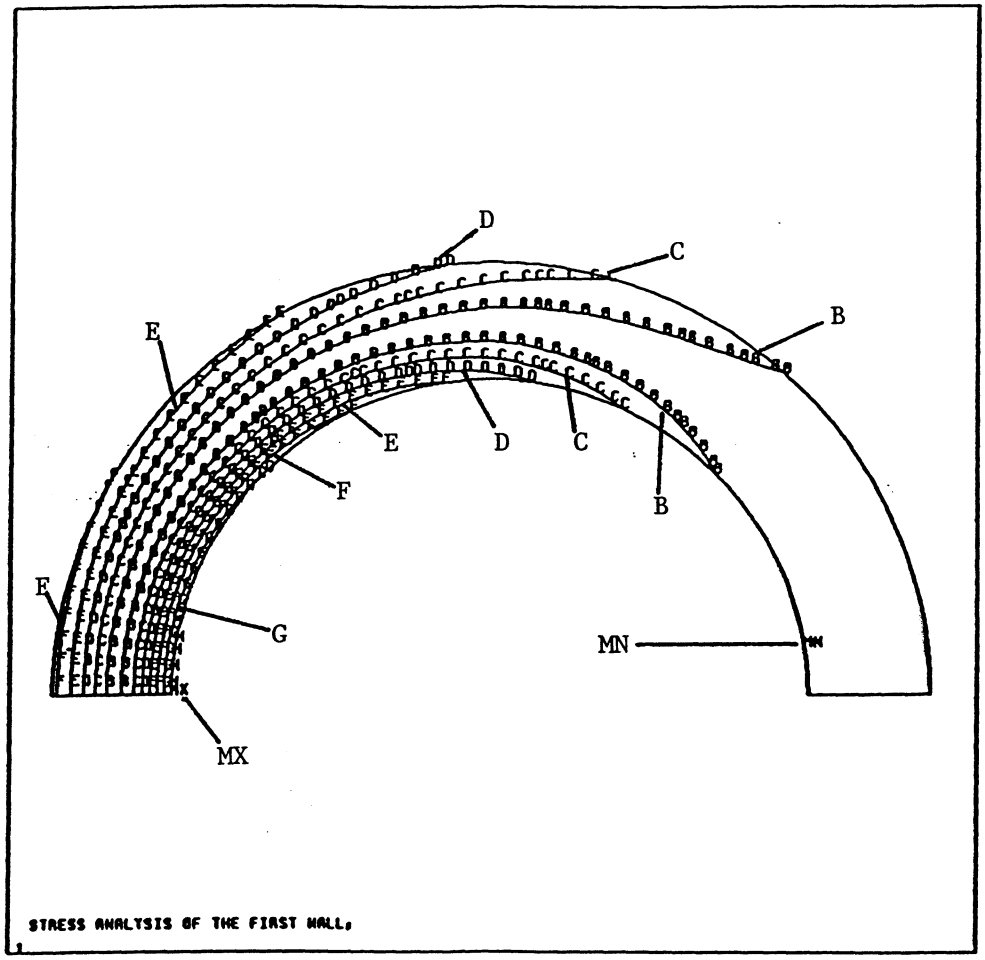

EQUIVALENT STRESS CONTOURS (MPa)

B=12.5	E=50.0
C=25.0	F=62.5
D=37.5	G=75.0
MN=0.305	MX=88.3

Fig. 8.2.-23. Equivalent stress in the first wall of the lithium design.

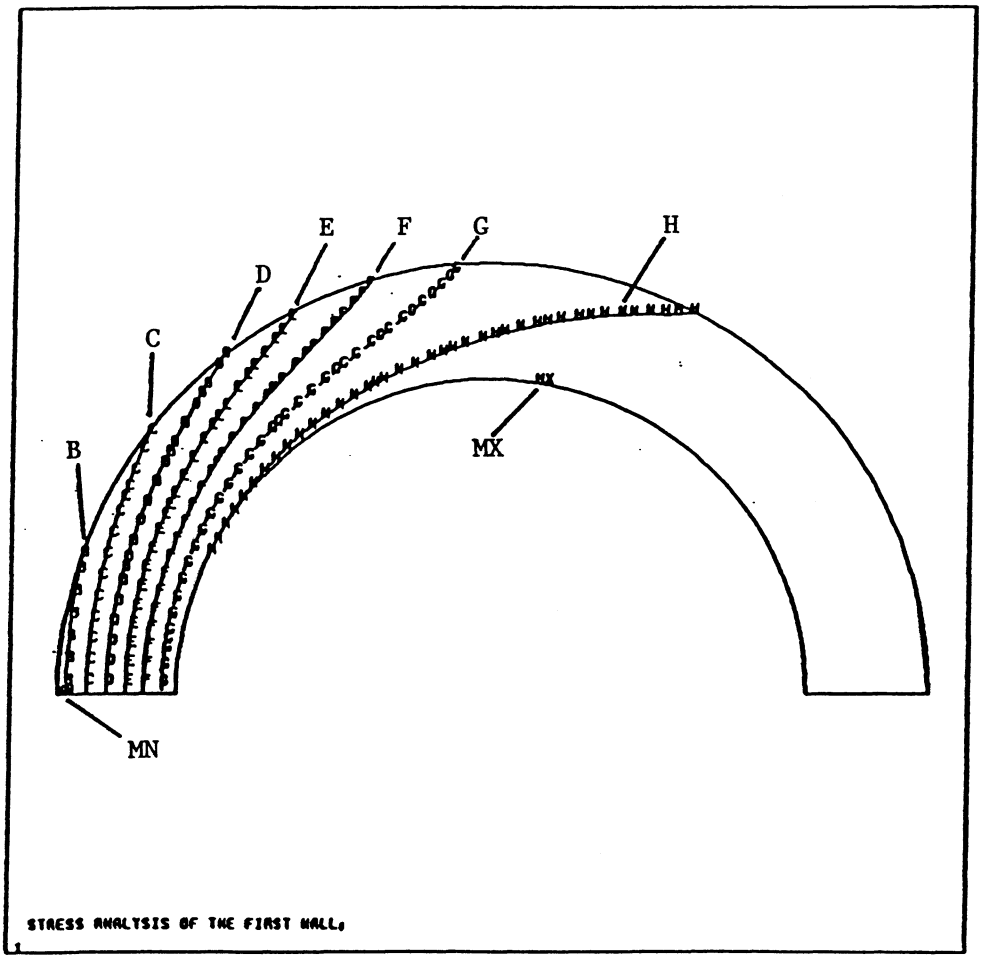

POLOIDAL STRESS CONTOURS (MPa)

B=-250	F=-50
C=-200	G=0
D=-150	H=50
E=-100	MX=83.9
MN=-268	

Fig. 8.2.-24. Poloidal stresses in the first wall of the lithium design.

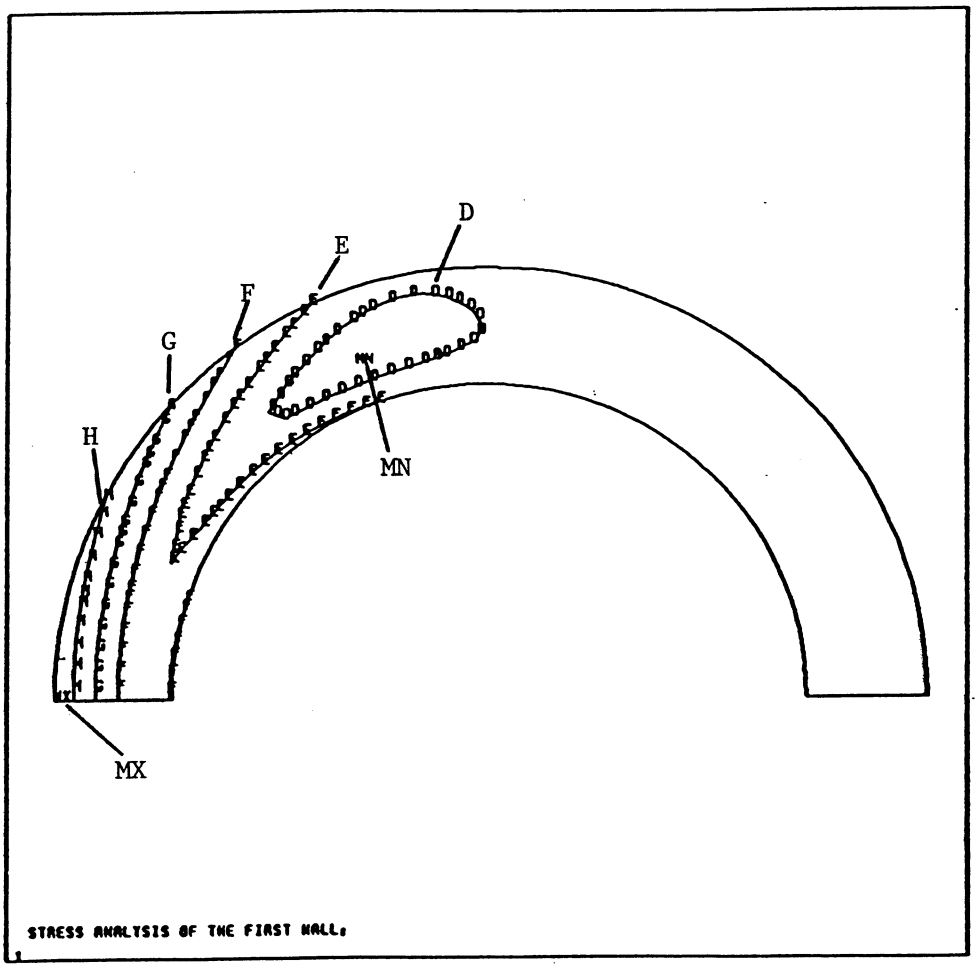

EQUIVALENT STRESS CONTOURS (MPa)

D=40	G=160
E=80	H=200
F=120	MN=11.5
MX=235	

Fig. 8.2.-25. Equivalent stresses in the first wall with axisymmetric analysis.

Table 8.2.-IX

Baseline Dimensions

R_p = 70 cm	R = 30 cm	W = 68
t_1 = 1 cm	t_2 = 1 cm	t_3 = 1 cm
t_4 = 1 cm		

Material Properties

E = 140 GPa	ν = 0.36	S_{mt} = 100 MPa

peak hoop stress did not change significantly but the maximum equivalent stress increased from 398 to 539 MPa. This increase is significant, but its effects can be mitigated by decreasing the bending through selective strengthening of the structure.

To reduce both the hoop and bending stresses, the back thickness, t_1 was increased to 2 cm and the side thickness, t_4 was increased to 1.5 cm. It is desirable to keep the other thicknesses small because increased structure in the portions of the module nearest the plasma will decrease the tritium breeding ratio and the high volumetric heating in this region will increase temperatures in the thickened structure. For this selectively reinforced blanket, the peak equivalent stress of 244 MPa occurred at the plasma-side corner, and the peak hoop stress was 112 MPa. The excessive bending can be reduced by filling the corner, so minimal design modifications should yield a blanket module capable of withstanding the coolant pressure with peak equivalent stresses within the limit of 100 MPa.

The blanket module must also tolerate the nuclear heating (81 MW/m^3 at the front for the 18 MW/m^2 wall loading case). Preliminary calculations indicate that the peak temperature (rather than the thermal stress) is the limiting factor and that a 10 mm thick front section is unacceptable because of the high heating rate and poor heat transfer in such large channels. The present design approach is to attempt to reduce the coolant pressure at inlet and outlet, thus allowing thinner walls and correspondingly lower peak temperatures. The thermal analysis of this blanket is being performed.

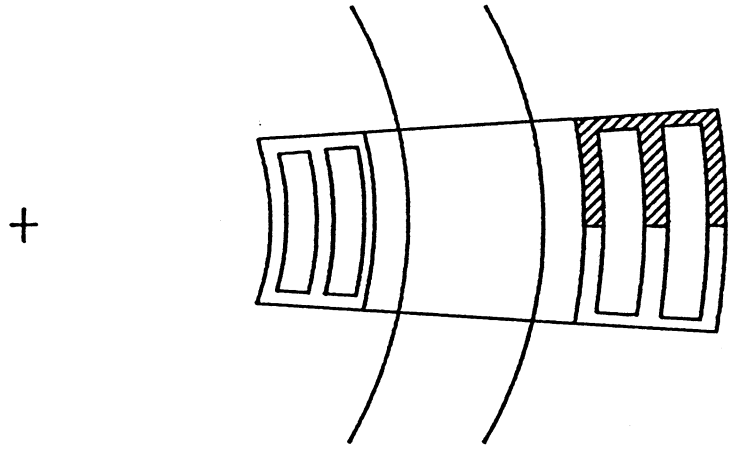

(a)

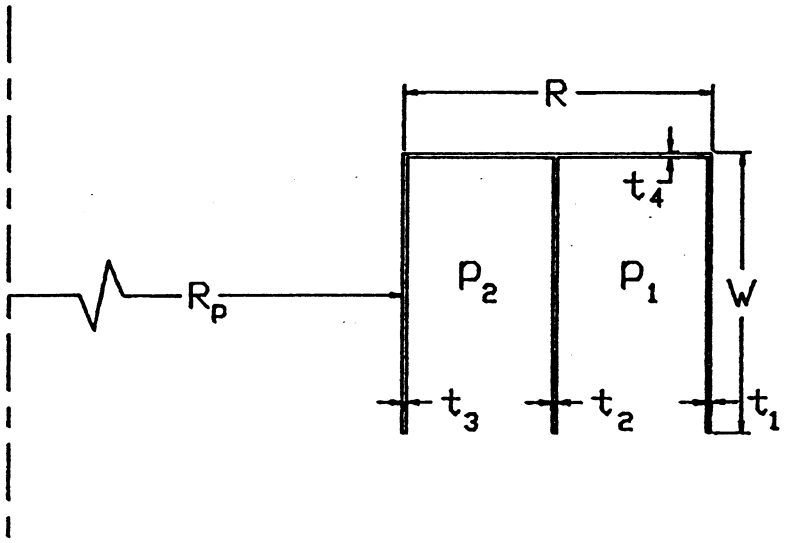

(b)

Fig. 8.2.-26. Model used for axisymmetric blanket stress analysis.

8.2.7. Tritium

In this section the tritium inventory and permeation in the high-heat-flux components near the plasma, i.e., the first wall and divertor is discussed. Calculations of inventory and permeation are made using the DIFFUSE code [26], which is based on a one-dimensional diffusion equation with various source and boundary conditions [26]. Calculations of first-wall inventory and permeation require estimation of high-energy triton implantation from the plasma, for which the TRIPOS code was used [27]. This code estimates the implantation fraction and range distribution of charged particles impinging on a solid material. The results are used as initial input for a DIFFUSE analysis.

The vanadium alloy V-3Ti-1Si is proposed for the first-wall and blanket structure. Since experimental values of permeation constants for these alloys are not available, permeation and material data for pure vanadium is used as an approximation.

First-wall calculations require an estimate of the impinging plasma flux and energy. The first-wall tritium flux is assumed to be about 1.6×10^{16} $cm^{-2}s^{-1}$. An energy of 50 eV and an incident angle of 45 degrees is assumed, which gives a TRIPOS result of 38.8% of impinging particles retained by the vanadium first wall. The implantation profile is used as input to DIFFUSE. A thickness of 0.15 cm for both first wall and divertor is used for calculations. First-wall temperatures of 700°C toward the plasma side and 500°C toward the blanket side near the lithium outlet are used. The lithium temperature is set at 600°C at the outlet and 400°C at the inlet. DIFFUSE allows the use of several boundary conditions. As was used in BCSS [6] for first-wall inventory and permeation calculations, a boundary condition of tritium diatomic molecular recombination at the surface is used. A coefficient used to reflect the ease of recombination is required by DIFFUSE: a value of 1 represents fast recombination (i.e., a clean surface), while lower values represent rougher surfaces. With a sputter-cleaned inner surface and an outer surface in contact with the lithium (with its large affinity for hydrogen isotopes), recombination coefficients of 1 are used for both surfaces, as was assumed in BCSS. All DIFFUSE runs simulate steady-state values after 30 days of continuous reactor operation.

At the first wall near the lithium inlet, a permeation rate of 47 g/d (scaled up to the total first wall area of 103 m^2) and a first wall inventory of 0.16 wppm is computed. Near the hotter lithium outlet, a total first-wall permeation rate of 44 g/d and inventory of 90 wppb is calculated. Thus, the

first wall will have a net permeation rate of approximately 45 g/d of tritium into the coolant. With the first wall represented as a sheet of area 103 m^2 and thickness 1.5 mm, the total first-wall inventory will be between 0.08 and 0.15 g. Actual volumetric first-wall calculations (considering the geometry of the first-wall pipes) might double this inventory.

For divertor calculations, the plasma flux at the plates is taken as 2×10^{20} $cm^{-2}s^{-1}$ and the particle energy as 75 eV (after acceleration through the sheath potential). For an incident angle of 45 degrees, TRIPOS indicates 42.2% of the impinging tritons are retained by the divertor. For a 1.5 mm thick divertor plate with 1 m^2 area, front and back temperatures of 700 and 500°C give a permeation rate to the coolant of 62 g/d and an inventory of 9.0 wppm (0.08 g) while a temperature profile of 600 to 400 °C gives 83 g/d permeation and 14 wppm (0.13 g) inventory. Since vanadium has a negative heat of diffusion, higher temperatures actually inhibit tritium diffusion, an advantageous effect in high temperature operation. Future design evolution and refinements of the flux and divertor models will alter the first estimates given above, particularly when the edge-plasma and divertor-plate conditions become better resolved.

To evaluate permeation through the outer shell of the lithium-containing structure, a Sievert's law boundary condition on the lithium-side is used in DIFFUSE; this condition considers solubility effects arising from an ambient gas pressure. Shell temperatures of 600°C toward the plasma and 650°C away are used. A tritium partial pressure is used typical of that for a lithium system containing about one wppm tritium at 600°C (i.e., about 2.9×10^{-12} atm [28]). The outer side of the shell employs a recombination boundary condition with an assumed recombination coefficient of 0.01. With vanadium known to oxidize to vanadium pentoxide, an outer permeation-resistant oxide layer is assumed. For an oxide layer resulting from a water-cooled first wall, BCSS assumes a low recombination coefficient of 5×10^{-5}. For a shell area of 190 m^2 and a thickness of 0.5 cm, a permeation rate of 0.047 g/d and a total shell inventory of 0.031 g tritium (5.4 wppb) are obtained. Varying the recombination coefficient does not significantly change the inventory, but the permeation rate does vary proportionately, (i.e., 0.73 g/d permeation for a coefficient of one and 5.1×10^{-4} g/d for a coefficient of 0.0001).

For blanket piping of 0.15 m diameter, a wall thickness of 3.0 mm and surface area of 400 m^2 (200 m^2 for the hot leg and 200 m^2 for cold leg) are assumed. Two temperature profiles are assumed: 550°C wall temperature for the hot leg and 300°C for the cold leg. As for the shell, Sievert's law is used for

the inside boundary condition and recombination outside (coefficient of 0.01). The hot-leg temperature gives a permeation rate of 0.61 g/d and average pipe inventory of 3.9 wppb (0.014 g), while the cold-leg conditions give a permeation rate of 2.7×10^{-3} g/d and an average inventory of 1.5 wppb (0.005 g). Total permeation of 0.61 g/d and inventory of 0.02 g can be expected for this piping. It should be noted that the effects due to the thermal insulation on the pipe and outer metal sheaths were not taken into account. These additional permeation barriers should reduce the net tritium leakage as was found in the MARS design [16].

In summary, first wall and divertor permeation rates of more than 100 g/d can be expected. Fortunately the tritium will pass into the lithium coolant, where it is recoverable with the bred tritium, mitigating permeation hazards but increasing extraction requirements. Permeation through the shell into the shield region may be 0.05 g/d, and permeation through blanket piping may be as much as 0.6 g. Total inventories within these structures should be less than 1 g. A greater concern may be long-term permeation through the shell and piping, with contamination of shielding and pipe insulation and subsequent release to the reactor hall environment. This possibility requires further study. All numerical results are tentative given further design advance and/or changes.

8.2.8. Conclusions

The preliminary engineering studies have shown the lithium-vanadium design to be feasible for the compact RFP reactor. Main features of the design are as follows:

1. Single heat transfer medium for first wall, blanket and shield. High-velocity liquid lithium appears adequate to cool the first wall with surface heating rates up to 4.5 MW/m^2. The favorable magnetic-field topology of the RFP reactor allows the use of high-velocity liquid-metal coolant without severe MHD problems.

2. Use of the vanadium alloy V-3Ti-1Si shows good resistance to the effects of neutron irradiation, in particular to helium embrittlement, relative to V-15Cr-5Ti.

3. Tritium breeding ratio $\geq$ 1.2 is easily achieved and with further

neutronics optimization the blanket energy multiplication can be increased from its present value of 1.21 to a value optimized for this design.

4. Because of the low toroidal-field requirements of the RFP reactor, the IBC concept is readily adapted to this configuration for both the toroidal-field coils and the divertor coils. The power-supply and bussing requirements do not appear to present an insurmountable problem and several options are being investigated.

5. The maximum vertical lift required during maintenance is ~300 tonnes which is well within the limits set for single-piece maintenance (Sec. 7).

Engineering analysis of this design has continued beyond the initial scoping phase and the design has evolved greatly from the results reported herein. Several key areas have been identified where further detailed engineering analysis is required to evaluate the attractiveness of this overall design. Efforts are continuing in the areas of single-piece maintenance and time-motion studies, tritium removal and processing systems, first wall, blanket and shield optimization, safety analysis of the consequences of off-normal events, and evaluation of the engineering requirements for start-up.

8.3. AQUEOUS LOOP-IN-POOL BLANKET DESIGN

In the early period of the scoping phase of this study, the safety advantages of the pool-type concept, introduced by D. K. Sze [29], and the aqueous-solution lithium breeder concept identified by D. Steiner [30], were recognized. Also the basic safety design principle of the Swedish PIUS fission reactor design [31], which proposes to submerge the hot-water loop of a PWR in a cold pool of water, appears attractive. Based on these designs, an aqueous "loop-in-pool" design emerged as part of the TITAN study.

Both the hot-water loop and the cold-water pool are at the high pressure of 9 MPa in the PIUS design. The pressure would be contained in a pre-stressed Concrete Reactor Vessel (PCRV). This pressurized "loop-in-pool" approach is essential for PIUS, since the fast introduction of borated water from the cold pool into the hot loop is necessary for emergency reactor shutdown. The loop

and pool mass transfer is controlled by density-gradient valves. The proper functioning of these density valves is a design issue that has received criticism from the fission industry. Another criticism for the PIUS reactor is the size of the PCRV, which is defined by the submersion of the fission core and primary heat exchangers. These requirements would not apply to the TITAN aqueous loop-in-pool blanket design, since fast introduction of the water from the cold pool to the hot loop is not necessary. Furthermore, an atmospheric pressure pool rather than a pressurized pool was chosen for the aqueous blanket design; density valves and construction of a large high pressure pool, therefore, will not be needed. The cold pool fulfills the functions of diluting the thermal and afterheat energy, thereby providing assurance against a loss of coolant accident and controlling the concentration of radioactivity, mainly tritium, under a loss-of-coolant-accident (LOCA) condition.

8.3.1. Concept Description

Figure 8.3.-1 shows the design approach. The high-pressure primary loop, including the torus and heat exchangers operating at 15.8 MPa, is submerged in a water pool at 0.1 MPa (atmospheric pressure). The reactor design characteristics are given in Table 8.3.-I. The parameters of the power-conversion loop were selected to be those of the advanced PWR design [32] being

TABLE 8.3.-I
DESIGN CHARACTERISTICS OF THE AQUEOUS BLANKET DESIGN

Major radius (m)	3.9
Minor first wall radius (m)	0.65
Neutron wall loading (MW/m^2)	20.0
Surface heat loading (MW/m^2)	5.0
Thermal power (MW)	2,948.
Net electric power (MW)	1,000.
Tritium breeder	$LiNO_2$ or $LiNO_3$
Neutron multiplier	Be
Tritium breeding ratio	1.25
Blanket energy multiplication	1.39
Coolant	water at 15.8 MPa
Inlet temperature (°C)	291.
Outlet temperature (°C)	326.
First wall material	Cu-Al25
Structural material	PCA or HT-9
First wall thickness (mm)	1.5
First wall temperature, peak (°C)	425.
Gross thermal efficiency	35%

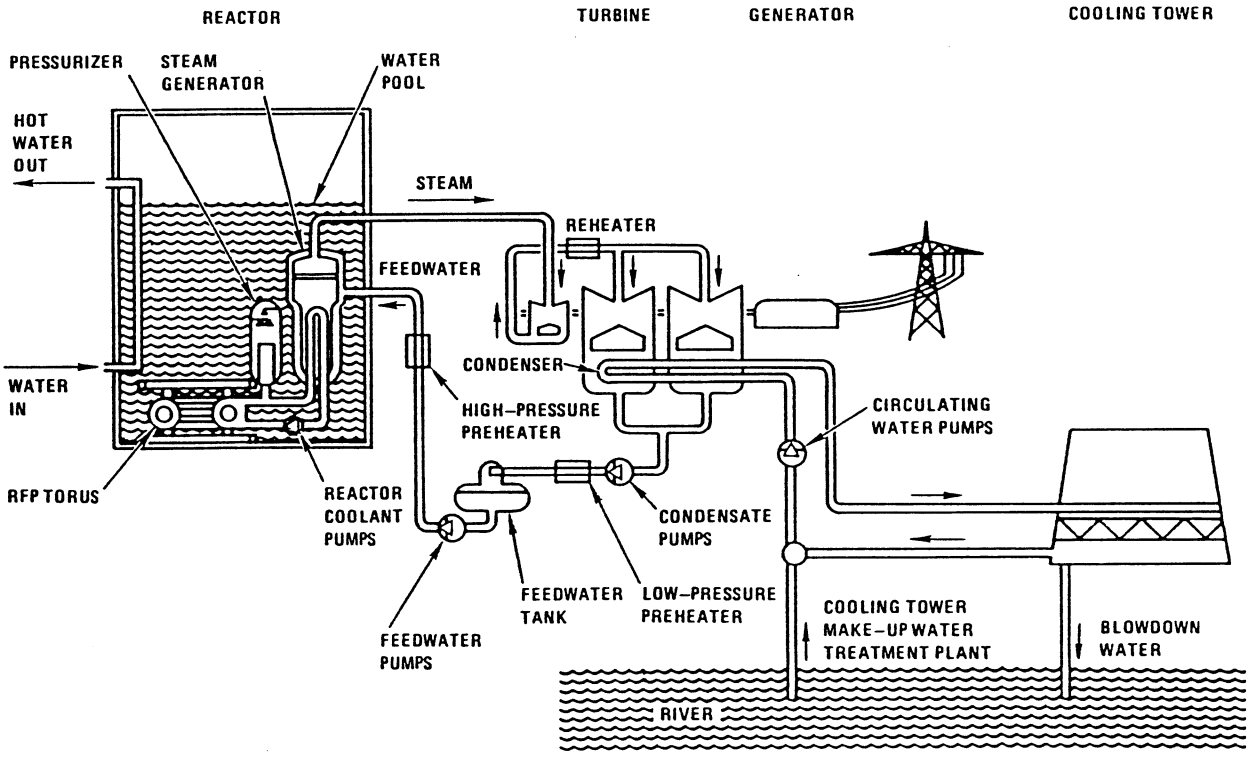

Fig. 8.3.-1. Schematic plant layout for TITAN aqueous blanket design.

constructed in Germany. To breed tritium, a lithium compound ($LiNO_2$ or $LiNO_3$) is dissolved into the hot-water loop.

As shown in Fig. 8.3.-2, the coolant at 291°C enters the bottom of the torus and exits at the top. The inboard and outboard channels are physically separated, as is illustrated in Fig. 8.3.-3, to satisfy the physics requirement that there be a poloidal non-conducting break in the first wall and blanket surrounding the plasma.

To make a thin first wall with high heat flux removal capability, a copper-alloy lobe construction is used, where the main structure supporting the vacuum wall is some distance behind that wall, as is shown in Fig. 8.3.-4. Between this main structure and the first wall is an open poloidal channel to permit high-speed coolant flow; immediately behind this channel is a 0.1 m thick zone containing beryllium for neutron multiplication. The lobes balance lateral pressure forces against each other and are tied back to washer-like poloidal rings made of stainless steel, which in turn take the short-direction compression.

The torus is divided into four quadrants by divertor chambers, which interrupt the lobed surface, effectively dividing the first wall and blanket into four separate pressurized assemblies. The back of these assemblies is not a pressure shell, but is only a sealing membrane that butts against the hot shield, as is shown in Fig. 8.3.-5. The massive hot shield serves as the main pressure-containing structural member.

The hot shield is an assembly of stainless-steel castings with integral cooling passages and forms a structural, but non-sealing, shell that contains the blanket assembly. The four toroidal quadrants will be further split in the toroidal direction to allow installation of the blanket assembly. The large forces on these pieces make it necessary to join them with machined serrated straps, to avoid major bolting problems.

Investigations show that care is required to ensure that the poloidal stainless steel rings are sufficiently rigid to inhibit the development of toroidal compressive stresses in the first-wall lobes. One of the possibilities considered for improving the design is to bolt the washer plates to the hot shield. This arrangement would assist the task of jointing the cast hot shield and also reduce the first wall toroidal stress. These bolts would require neither penetration of the blanket pressure boundary nor great precision in the shield.

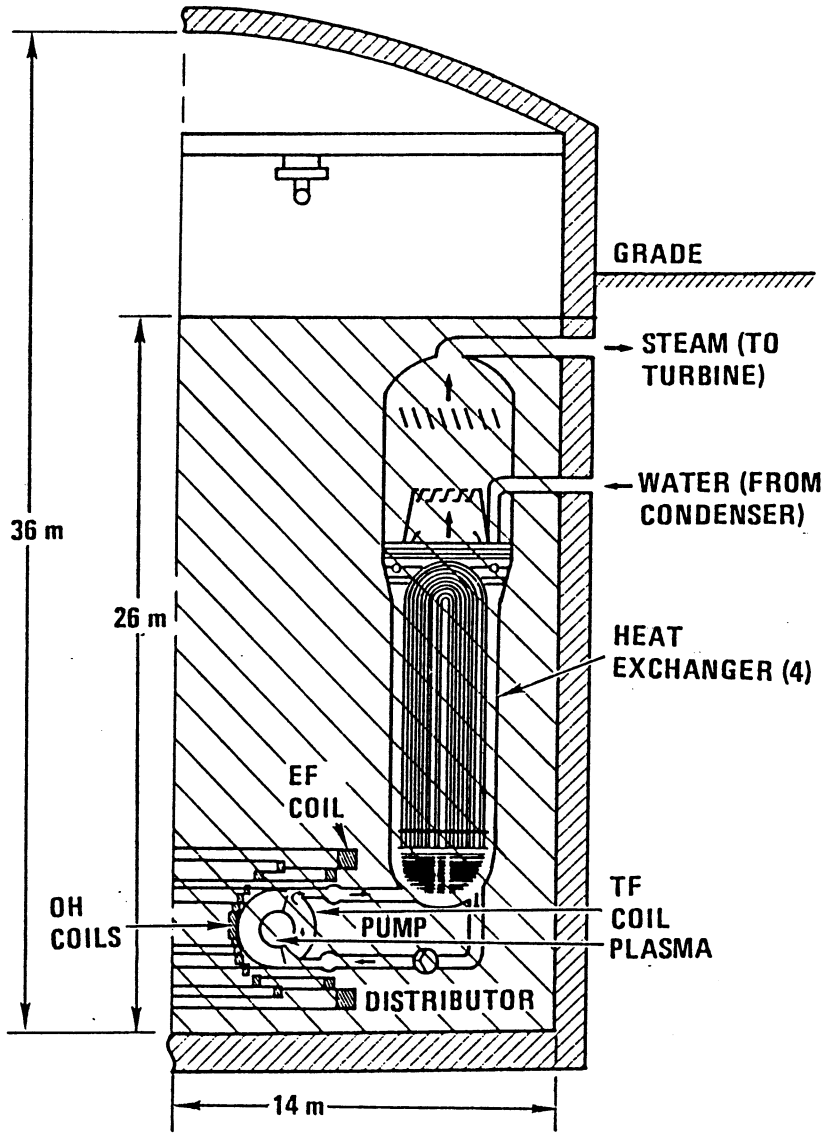

Fig. 8.3.-2. The torus and heat exchanger of the TITAN aqueous blanket design.

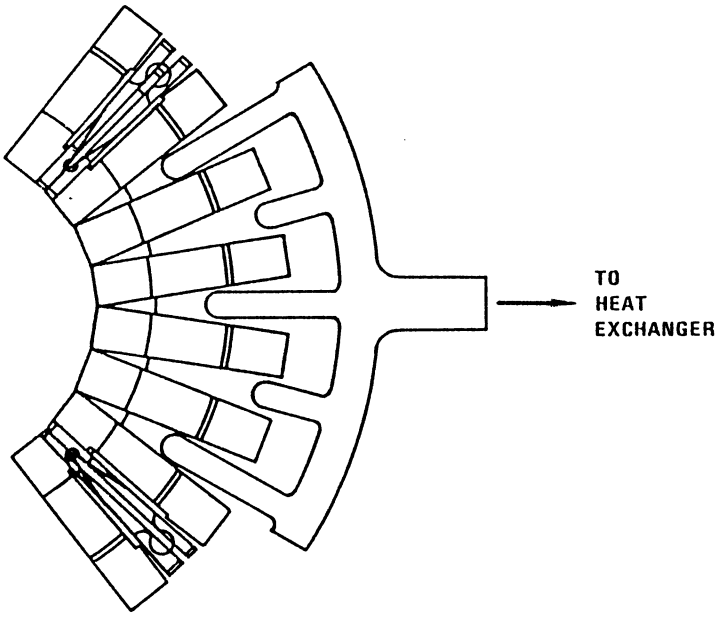

a. TOP VIEW, DISTRIBUTOR SCHEMATIC

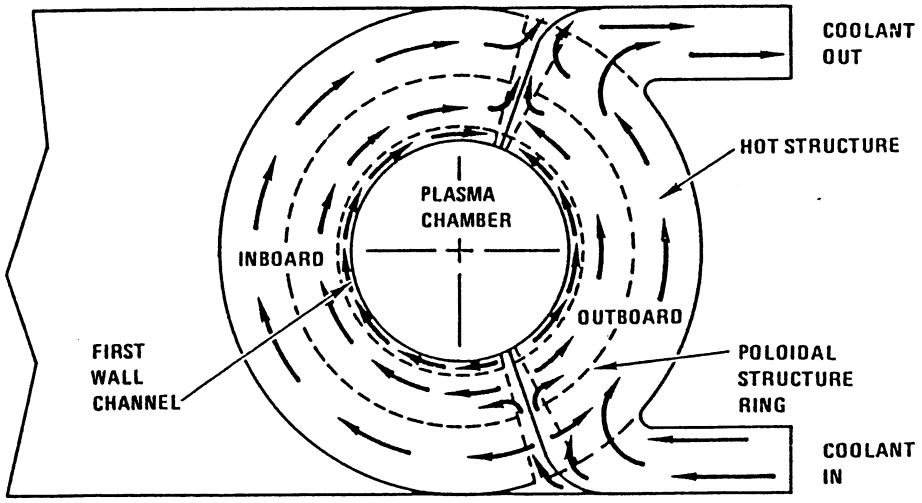

b. SIDE VIEW, INBOARD / OUTBOARD MODULES

Fig. 8.3.-3. Coolant flow distribution in the aqueous blanket design.

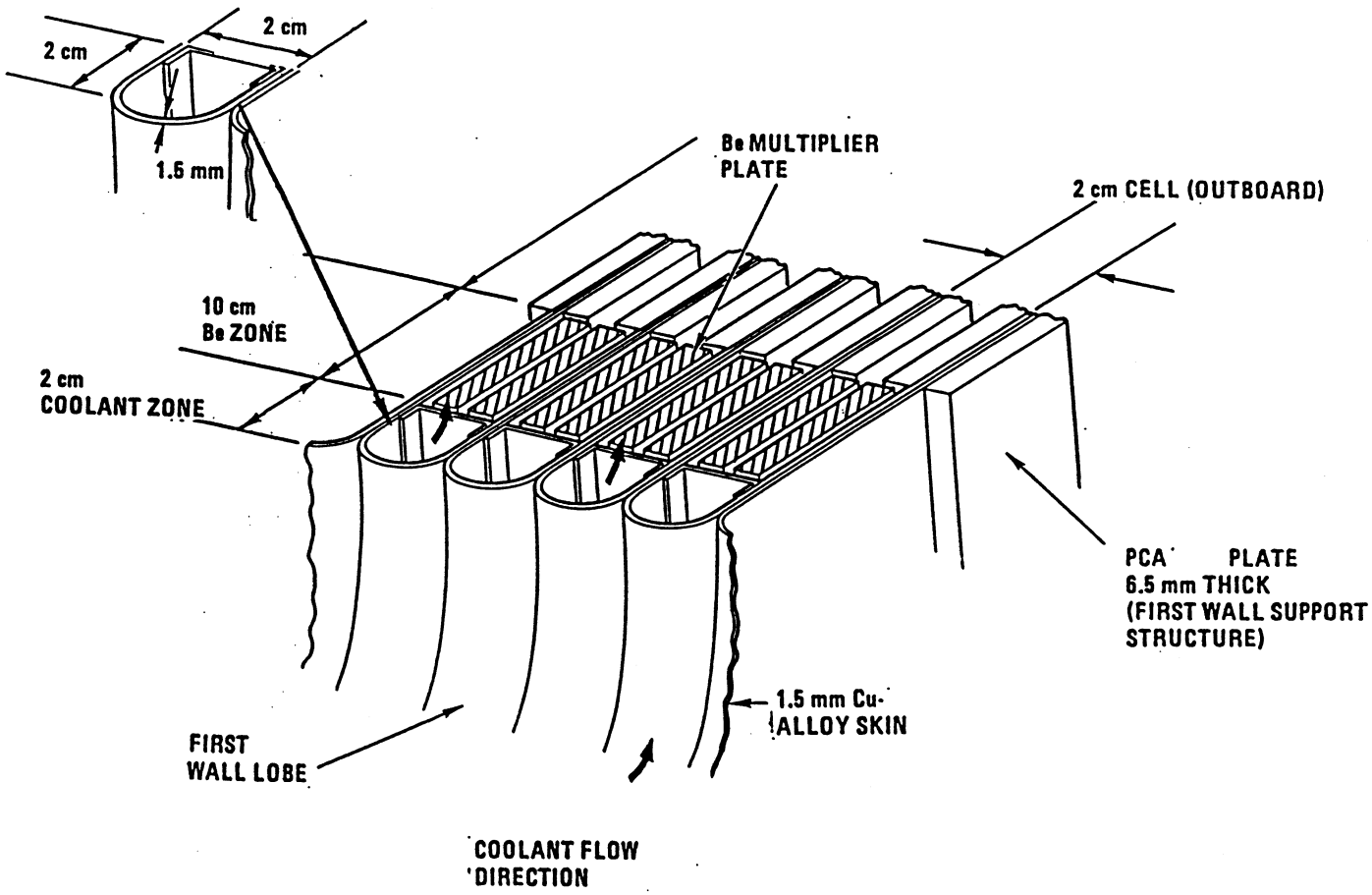

Fig. 8.3.-4. Aqueous blanket first wall and breeder structure.

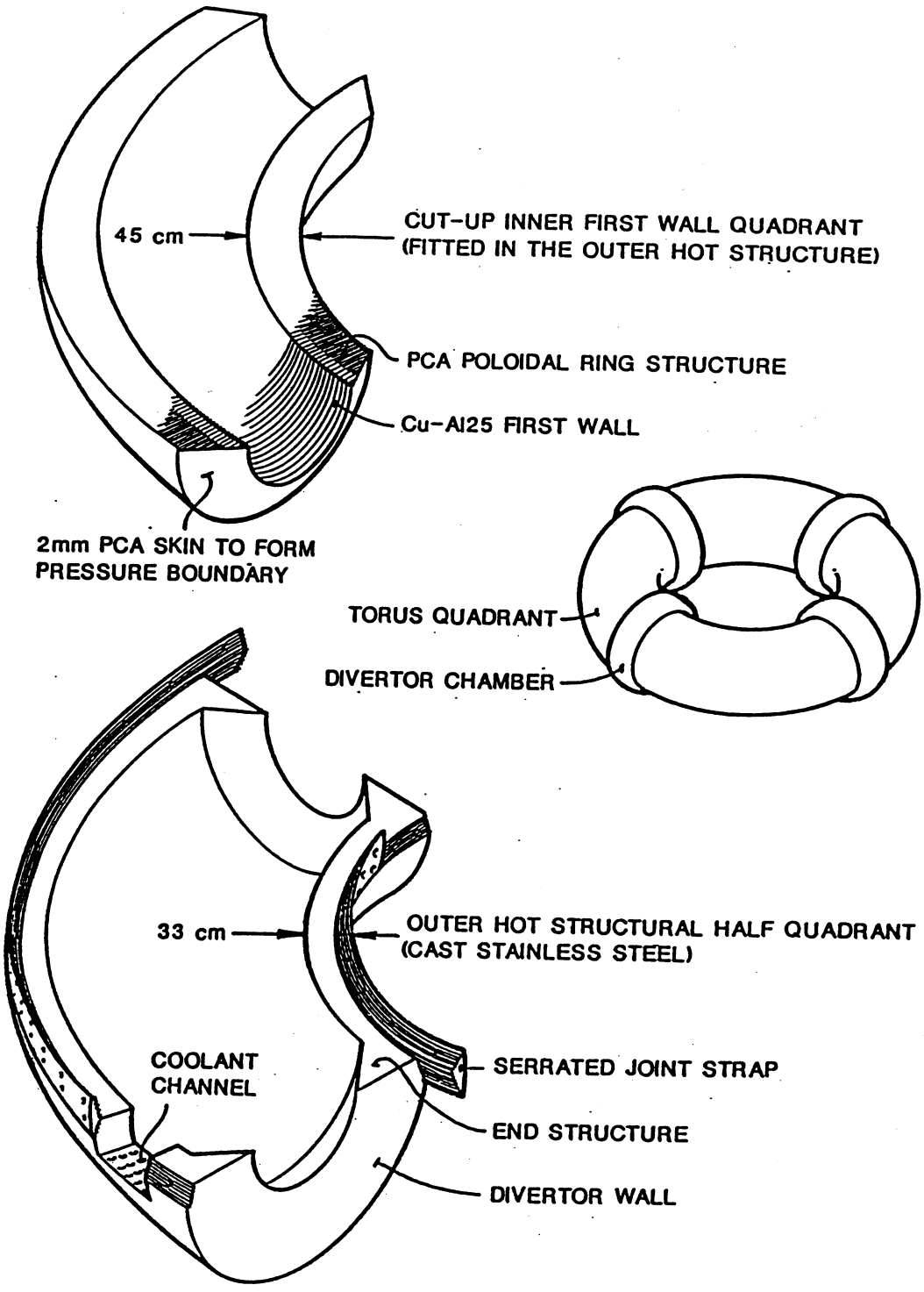

Fig. 8.3.-5. Torus structure of the aqueous blanket design.

8.3.2. Materials

8.3.2.1. Breeding Materials

Breeding in the TITAN aqueous blanket concept is accomplished by dissolving 5 to 10 wt.% ^{6}Li in the water circulating through the first wall and blanket. A summary of solubility limits of various lithium compounds is given in Table 8.3.-II. Short-lived radionuclei of Cl, I, and Br would increase shielding requirements up to and including primary loop heat-exchangers. Using LiOH would avoid this problem, but LiOH has a relatively low solubility and increases the pH value of the solution. Copper tends to form a corrosion inhibiting oxide layer in water. Since the stability of this oxide layer is a function of temperature and the pH value of the solution, as is shown in Fig. 8.3.-6, LiOH cannot be considered as a primary breeding candidate. The most promising candidates are lithium compounds containing N and C. However, ^{14}C is produced from these compounds, and the design implications of this radionuclide needs to be studied.

8.3.2.2. Structural Materials

The structural materials proposed for the TITAN aqueous blanket concept are combinations of Cu-alloys and/or vanadium alloys with PCA. Experimental results have shown good compatibility between water and V-15Cr-5Ti, mainly as a result

TABLE 8.3.-II
CANDIDATE LITHIUM COMPOUNDS

Compound	Solubility limits (at.%)	pH	Remarks
LiCl	7.2 at 160°C		Potential problems
LiBr	4.6 at 100°C		of induced radio-
LiI	3.6 at 120°C		activity
$LiNO_2$	6.4 at 99°C	~7.25	Most promising
$LiNO_3$	4.5 at 71°C	~7	Promising
$LiCHO_2$	5.1 at 120°C	~7.4	Promising
$LiC_2H_3O_2$	4.3 at 158°C	~7.9	Promising
LiOH	3.4 at 322°C	~14.8	Too basic

of the formation of protective Cr_2O_3 and rutile (TiO_2) layers [33,34]. The stability of these layers is sensitive to the coolant pH level; the minimum solubility of Cr_2O_3 occurring at a pH of approximately 7 [35]. Fluctuation of the pH level above or below 7 must be suppressed to avoid breakdown of the protective layer followed by further oxidation. Other vanadium-based alloys (V-20Ti and VANSTAR-7) have shown unacceptable corrosion levels in 288 °C water [34], while the V-15Cr-5Ti (the vanadium alloy most compatible with water) has less desirable radiation resistance behavior [36] compared with V-3Ti-1Si and VANSTAR-7 (Sec. 8.2). The use of copper alloys as a first-wall and structural material was therefore investigated.

Copper is known to be corrosion resistant in pure water because of the formation of a CuO layer. The stability diagram of CuO (Fig. 8.3.-6) shows a minimum solubility for a pH of 9 at 25°C. Increasing the temperature to 300°C would reduce the pH level of water by about unity. Furthermore, it is apparent form Table 8.3.-II that a solution of a lithium compound containing nitrogen or carbon will increase the pH level only slightly above 7. To assure a pH value of about 9, controlled amounts of LiOH could be added to the solution.

The question of candidate Cu-alloys for fusion applications has been investigated in detail [37-44]. The effect of radiation on mechanical and physical properties has been documented up to 63 dpa at 450 °C by Brager et. al. [37]. The most promising candidate alloys considered in this study are Cu-A125 (Cu, 0.25 at.% Al_2O_3), Cu-Be (Cu, 2.0 at.% Be), and MZC (Cu, 0.025 at.% Mg, 0.1 at.% Zr, 0.9 at.% Cr). Irradiation data up to 10^{23} neutrons/cm^2 ($E > 0.1$ MeV) show low swelling (< 0.3%) for all candidates (up to 63 dpa at 450°C). Experiments on yield strength at 16 dpa and 450°C [38] show a modest decrease in candidate Cu-alloys (see Fig. 8.3.-7).

The hard neutron spectrum at the first wall produces Ni and Zn from transmutation reactions in Cu. Rough estimates for 20 MW/m^2 neutron wall loading using Butterworth's neutronics results [39] indicate the production of approximately 3.9 wt.% Ni and approximately 0.8 wt.% Zn. Figure 8.3.-8 shows the effects of the Ni and Zn contents on the thermal conductivity of copper. Although the conductivity drops from about 350 W/m K to about 100 W/m K with a 5 wt.% Ni content, it is still approximately 3 times higher than that of HT-9.

The thermal conductivity can also be estimated from the electrical conductivity using the Wiedemann-Franz relationship ($k\rho/T$ = constant where k is the thermal conductivity, ρ is the electrical resistivity, and T is the absolute temperature). Experimental data [37] up to 63 dpa are available as shown on

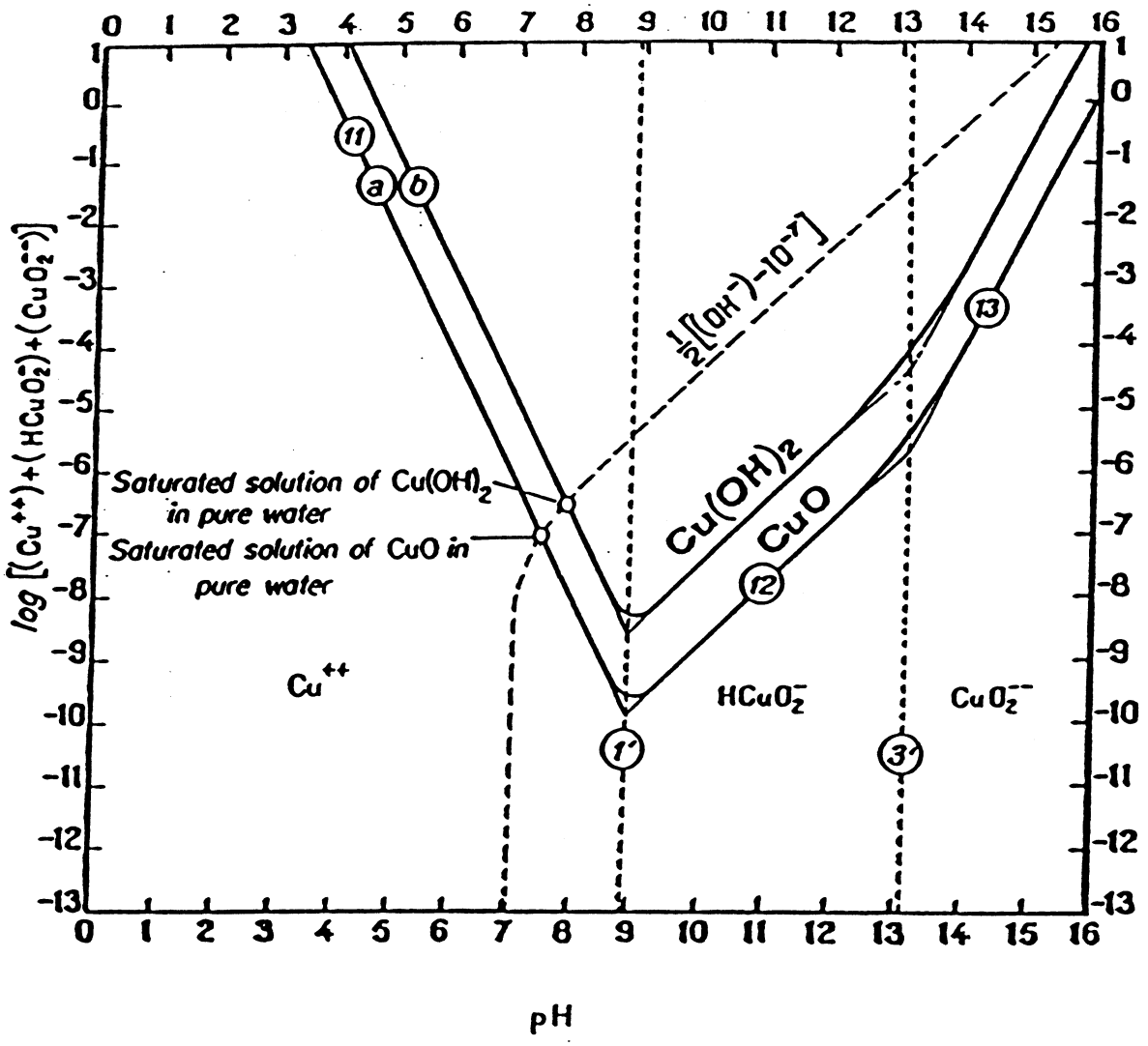

Fig. 8.3.-6. Influence of pH on the solubility of CuO and $Cu(OH)_2$, at 25°C [35].

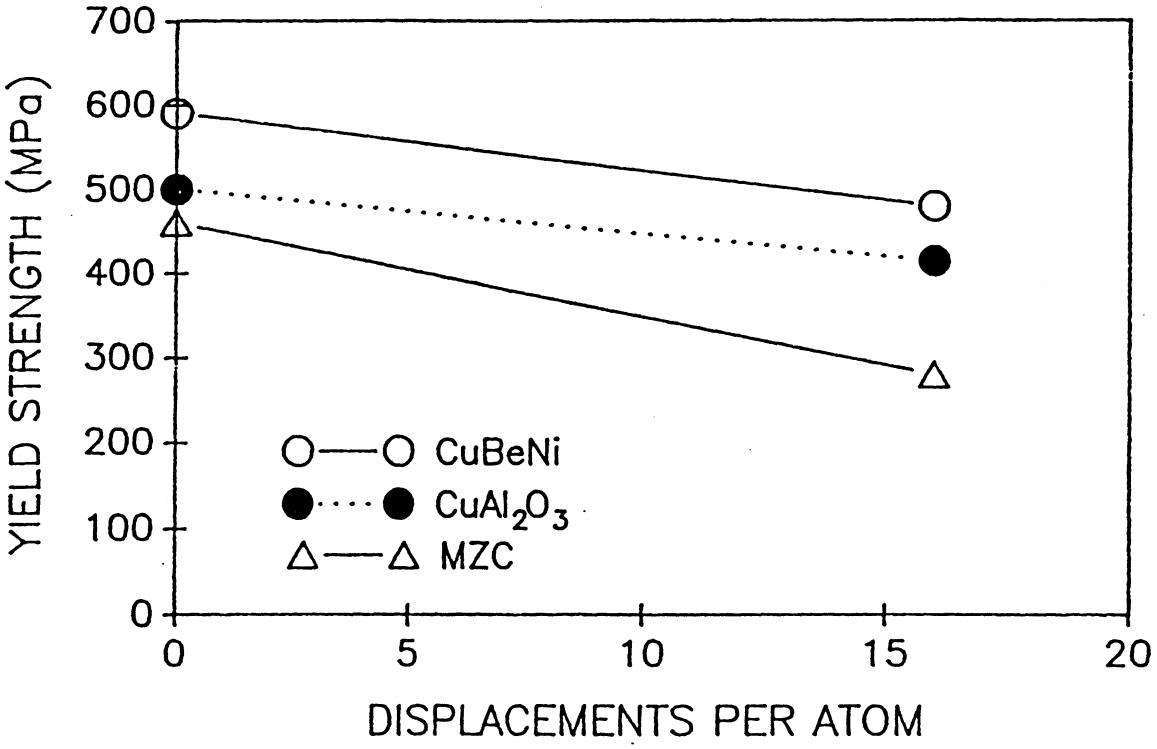

Fig. 8.3.-7. Yield strength behavior of commercial copper alloys irradiated at 450 °C to 16 dpa [38].

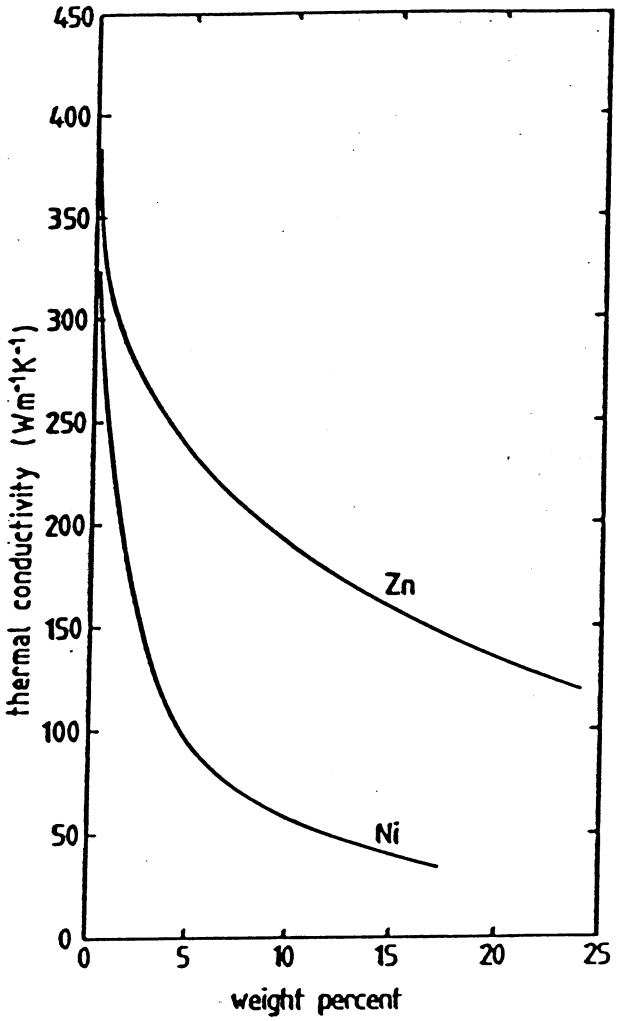

Fig. 8.3.-8. Effect of nickel and zinc contents on the room temperature thermal conductivity of copper [39].

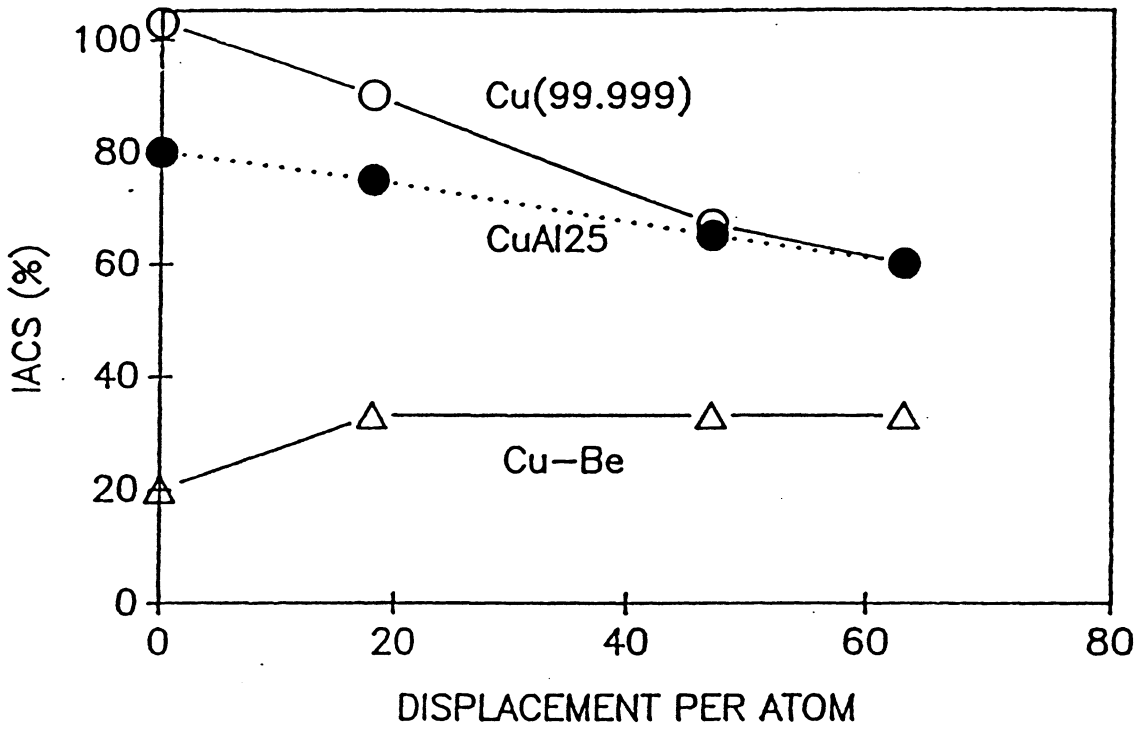

Fig. 8.3.-9. Effect of neutron irradiation on the electrical conductivity of commercial copper alloys at 450 °C to 63 dpa [37].

Fig. 8.3.-9. Cu-A125 shows a better electrical conductivity behavior than Cu-Be.

The potential material compatibility problems related to electrolytic and radiolytic effects in the presence of solution of Li-compounds, Cu-alloy, Be-metal and PCA in the blanket module at elevated temperature will need to be addressed in the future.

In summary, copper corrosion levels in water are minimized at a pH of approximately 9. Solutions of lithium seem possible from a corrosion view point The alloy Cu-Al25 appears to be a good choice for a high-conductivity, high-strength, and irradiation resistant material. At 450°C and 63 dpa this alloy shows: (1) low swelling (approximately 0.3%), (2) a small drop in yield strength (approximately 90 MPa), and (3) a acceptable loss of electrical conductivity. Further investigation would require examination of (1) the electrolysis and radiolysis of water and consequent effects on the mechanical and physical properties of Cu-alloys, (2) the effects of the electromagnetic environment on a Cu-PCA-water system, and (3) the buildup of ^{14}C in the coolant loop.

8.3.3. Neutronics

The neutronics calculations were performed using both a deterministic transport code, ANISN [1], and Monte Carlo code, MCNP [3]. The nuclear-data libraries employed are 30-group neutron and 12-group gamma-ray MATXS5, and continuous energy RMCCS coupled neutron-gamma ray libraries, both processed at Los Alamos National Laboratory, based on the basic ENDF/B-V general purpose data files. The comparison of tritium breeding values calculated from these codes and nuclear-data libraries revealed large discrepancies between the results of the two calculations. These differences are attributed to the self-shielding effect in the absorption cross section in copper. Because the multigroup cross-section library processed from the MATXS5 data set is not self-shielded, it overestimated the copper absorptions. All subsequent neutronics calculations were then performed with the Monte Carlo code, MCNP, and the continuous energy nuclear data library, RMCCS. Only the results obtained from these Monte Carlo calculations are presented.

Table 8.3.-III describes the one-dimensional zones and material compositions of the neutronics model employed in the calculation for the aqueous blanket design. As shown in Table 8.3.-III, the model consists of a 20 mm first wall made of 15% Cu and 85% H_2O, a neutron multiplier zone of variable thickness (70 to 140 mm), a reflector/shield made of 15% Cu, 70% stainless steel, 15% H_2O,

TABLE 8.3.-III

ZONES AND MATERIAL COMPOSITIONS OF THE ONE-DIMENSIONAL NEUTRONICS MODEL FOR THE TITAN AQUEOUS BLANKET DESIGN[a]

Zone	Thickness (m)	Composition
Plasma	0.6	Void (neutron source)
Vacuum	0.05	Void
First wall	0.02	15% Cu + 85% H_2O[b]
Neutron Multiplier	x (variable)	15% Cu + Be + H_2O[c]
Reflector/shield	0.41-x	15% Cu + 70% PCA[d] + 15% H_2O
TF/OH magnets	0.4	10% H_2O + 10% insulator + 80% Cu

[a] minor-radius model in cylindrical geometry

[b] 5 at. % ^6Li is assumed in all water coolants except in the TF/OH coils

[c] beryllium and water volume fractions change as desired

[d] Primary Candidate Alloy: a titanium-modified stainless steel.

and a magnet zone. Beryllium is selected as the neutron multiplier because of its superior neutron multiplication compared with any other nonfissionable multipliers. The content of beryllium in this neutron multiplier zone can be determined according to design options. One of these options is to recycle beryllium because of resource considerations. This option would lead to a pellet design approach for the beryllium material and result in a 60% - 40% volume fraction distribution for the beryllium and water coolant, respectively, in the neutron multiplier zone, excluding the 15% of volume space taken up by the copper structure. The other design option for the beryllium material is a plate design which maximizes the volume fraction of beryllium in this multiplier zone. This could lead to a 80% - 20% volume fraction distribution for beryllium and water coolant, respectively. The tritium breeding ratio and nuclear heating rate of these two design options are discussed later in this section.

The tritium breeder in the TITAN aqueous blanket design is a lithium compound dissolved in the water. The ^6Li content in water is an important parameter to determine whether the reactor system is able to breed adequately. Preliminary studies showed that a aqueous solution containing 5 at.% ^6Li is

probably acceptable from the viewpoint of tritium breeding. For lower ^6Li concentrations it is difficult to achieve a TBR greater than 1.15 because of the large fraction of copper in this system. Many lithium compounds such as LiOH, $LiNO_2$, and $LiNO_3$ show 3 to 7 at.% ^6Li solubilities in water at the desired operating temperatures. In the present design the solute is chosen to be $LiNO_2$, on the grounds of adequate solubility and compatibility with the structural materials. A value of 5 at.% ^6Li concentration in water was used in all neutronics calculations. The tritium breeding ratio and nuclear heating rate are given in Table 8.3.-IV for different beryllium multiplier zone thicknesses and compositions.

As shown in Table 8.3.-IV, a tritium breeding ratio of 1.2 can be obtained for the beryllium pellet design with 42.5% and 42.5% beryllium and water volume fractions at a multiplier zone thickness of 0.14 m. The effective beryllium thickness is about 0.06 m. The blanket energy multiplication is 1.32 for this design. For the same thickness but a higher beryllium content of 68%, the tritium breeding ratio becomes 1.32. The blanket energy multiplication also

TABLE 8.3.-IV
TRITIUM BREEDING RATIOS AND NUCLEAR HEATING RATES IN THE AQUEOUS BLANKET DESIGN BY VARYING NEUTRON MULTIPLIER ZONE COMPOSITION AND THICKNESS

Neutron Multiplier Zone composition	15% Cu 42.5% Be[a] 42.5% H_2O[b]		15%Cu 68% Be 17% H_2O	
Zone thickness (m)	0.14	0.07	0.14	0.10[c]
Tritium Breeding (T per DT neutron):				
First wall	0.22	0.38	0.37	0.39
Neutron multiplier	0.80	0.51	0.68	0.51
Reflector/shield	0.18	0.22	0.27	0.35
Total TBR	1.20	1.10	1.32	1.25
Nuclear Heating (MeV per DT neutron):				
First wall	3.24			4.23
Neutron multiplier	10.87			8.13
Reflector/shield	4.47			7.31
Total blanket/shield	18.6			19.7
Blanket energy multiplication	1.32			1.39
Heating to magnets	0.02			0.02

[a] 90% dense
[b] 5 at. % ^6Li in H_2O for all cases
[c] Reference design

increases to 1.4. The neutron-multiplier zone thickness, therefore can be reduced to optimize the beryllium inventory in the blanket while maintaining an adequate tritium breeding ratio. The tritium breeding ratios of 1.10 and 1.25 are obtained for multiplier-zone thicknesses of 0.07 and 0.10 m, respectively (Table 8.3.-IV). A 0.1 m thick neutron multiplier zone is necessary to assure a TBR of 1.2. Note that for the reference design, the aqueous blanket energy multiplication is about 1.39, of which 21% is deposited in the first wall, 41% in the neutron multiplier zone, and the balance in the reflector/shield zone. The energy deposited in the TF/OH magnets is only 0.1% of the blanket energy (0.021 MeV per DT neutron).

Because of the excellent neutron moderation in the beryllium/water blanket, the neutron flux at the TF coil, which is 0.45 m from the first wall, is ~ 10^{21} n/cm^2/yr (E>0.1 MeV) at 20 MW/m^2 neutron wall loading. Based on the design lifetime limit of 4×10^{22} n/cm^2 for the spinel insulator in the magnet coil, the TF coil can survive for 40 FPYs.

8.3.4. Thermal Hydraulics

The TITAN aqueous blanket design shown in Figs. 8.3.-4 and 8.3.-5 consists of approximately 1400 poloidal ring units, which form the first-wall and blanket assembly. The cross section of these segments resembles a narrow U with the lobe acting as the first wall. The cooling of this lobe section could impose thermal restrictions on the concept. Calculations are performed with an assumed neutron wall load of 20 MW/m^2 and the surface heat flux (or, f_{RAD}) as a parameter.

Each ring unit is divided into an inboard and an outboard channel. Cooling water enters at the bottom and exits at the top of the torus; this configuration is suitable for natural circulation under loss-of-flow accident (LOFA) conditions. The water inlet temperature is set to T_{in} = 291°C, and the outlet temperature is T_{out} = 326°C at a coolant pressure of 15.8 MPa similar to the KWU PWR [32]. The mass flow rate is adjusted accordingly. Because of the difference in the inboard and outboard areas, and, hence, power, the channel separation in the segments is shifted outboard to 80.6° poloidal elevation from the torus midplane, as illustrated in Fig. 8.3.-3. For the given torus aspect ratio, this geometry assures equal power at equal mass flow rate in all channels, but results in a higher pressure drop at the inboard side. As an alternative, calculations show that this difference in the pressure drop could be avoided by separating the ring segment at exactly the top and bottom

positions. The difference in inboard/outboard frictional losses then adjusts the mass flow in compliance with the temperature requirements. The former option was selected, because of the relative ease of positioning the inlet/outlet coolant pipes without disturbing the magnetic coil set, as is shown in Fig. 8.3.-3.

The location of the coolant-channel lobe which faces the plasma directly experiences the maximum local heat flux. This maximum heat flux varies between 0.24 MW/m^2 and 5.24 MW/m^2 (corresponding to f_{RAD} ranging from 0. to 1.0); the former value is from volumetric power generation. To evaluate the design, a one-dimensional heat-transfer analysis was performed for this maximum-heat-flux location at the channel outlet. The temperature difference in the wall includes a minor contribution for the volumetric heat production in copper, 160 MW/m^3 at 20 MW/m^2 neutron wall loading.

Where applicable, a standard Nusselt correlation is used for convective heat transfer. High heat fluxes, however, are likely to lead to subcooled flow boiling (SFB) heat transfer. This mode change substantially improves the water-side heat transfer. With the above-mentioned coolant outlet condition, the bulk water never reaches saturation. Therefore, SFB can develop when the bulk temperature exceeds the criterion for the onset of nucleate boiling (ONB) [45]. This requires a certain overheat at the interface surface to overcome the coolant surface tension. The ONB condition is satisfied at the coolant-channel exit when the heat flux exceed about 1 MW/m^2 ($f_{RAD} > 15\%$); it applies for the whole channel when the heat flux is greater than about 3 MW/m^2 ($f_{RAD} > 55\%$). With the comparatively long hydraulic lengths of L/D = 150 for the inboard and L/D = 110 for the outboard channel, the initial SFB could transform into an annular-flow boiling. The determination of the exact regime is not well established and the subject of ongoing research [46]. This uncertainty particularly applies to the proposed design, which features a curved coolant channel with varying, non-circular cross sections and is exposed to non-uniform heat flux around the tube surface. Annular film boiling, however, shows excellent heat-transfer properties as well. Thus, it is not expected to affect considerably the above-estimated wall temperatures. The nucleate-boiling heat transfer is calculated following a procedure by Kutateladze [47], which superimposes a forced convective and a boiling term, the latter being a function of pressure and heat flux. Based on the formulation by Jens and Lottes [48], the present design operates below the critical heat flux (CHF) for the entire range of first-wall heat flux (or f_{RAD}) values.

The resulting temperature differences, the interface temperature and the maximum wall temperature are plotted in Fig. 8.3.-10. It should be noted that the SFB temperature difference refers to the saturation temperature of 346°C while the convective heat transfer refers to the bulk temperature of 326°C at the coolant channel exit. As shown in Fig. 8.3.-10, the calculated maximum wall temperature is below the 450°C limit of the proposed copper alloy.

According to Ref. 45, the pressure drop is only marginally affected by SFB. Although the coolant velocity is relatively high (minimum of 4 m/s outboard at 0.24 MW/m^2 heat load at $f_{RAD} = 0$, maximum of 12 m/s inboard at 5.24 MW/m^2 at $f_{RAD} = 1.0$), the relative pumping power for the first-wall channels remains on the order of 0.1% of the heat removed. High water speeds (~ 10 m/s) are also required in the manifolds, which have to cope with the restricted space available between the toroidal coils. Total pumping-power requirements have not been assessed, but are expected to be relatively small.

8.3.5. Structural Analysis

Because of the high water pressure and the high thermal gradients, with potential for thermal stress, stress analysis of the first wall is important for the aqueous blanket design. To calculate pressure stresses, the first-wall lobe is calculationally lumped as a ring with a stiffness based on the cross-sectional area. The notation and the coordinate system are shown on Fig. 8.3.-11. Neglecting the stresses in the annulus along the y direction (i.e., plane-stress condition), the general solution for the displacement in the supporting annulus in the x direction is given by,

$$U = C_1 + \frac{C_2}{x} , \qquad (8.3.-1)$$

where C_1 and C_2 are solution constants.

By imposing a continuity condition between the ring and the annulus at the inner radius and by prescribing the radial stress at the outer radius, C_1 and C_2 can be determined, and stresses can be estimated in the annulus. The displacement at the inner radius is calculated and imposed on the finite-element model of the first-wall lobe as is shown on Fig. 8.3.-12.

Since a uniform temperature does not cause stresses, thermal strains leading to thermal stresses are calculated using the coolant bulk temperature as

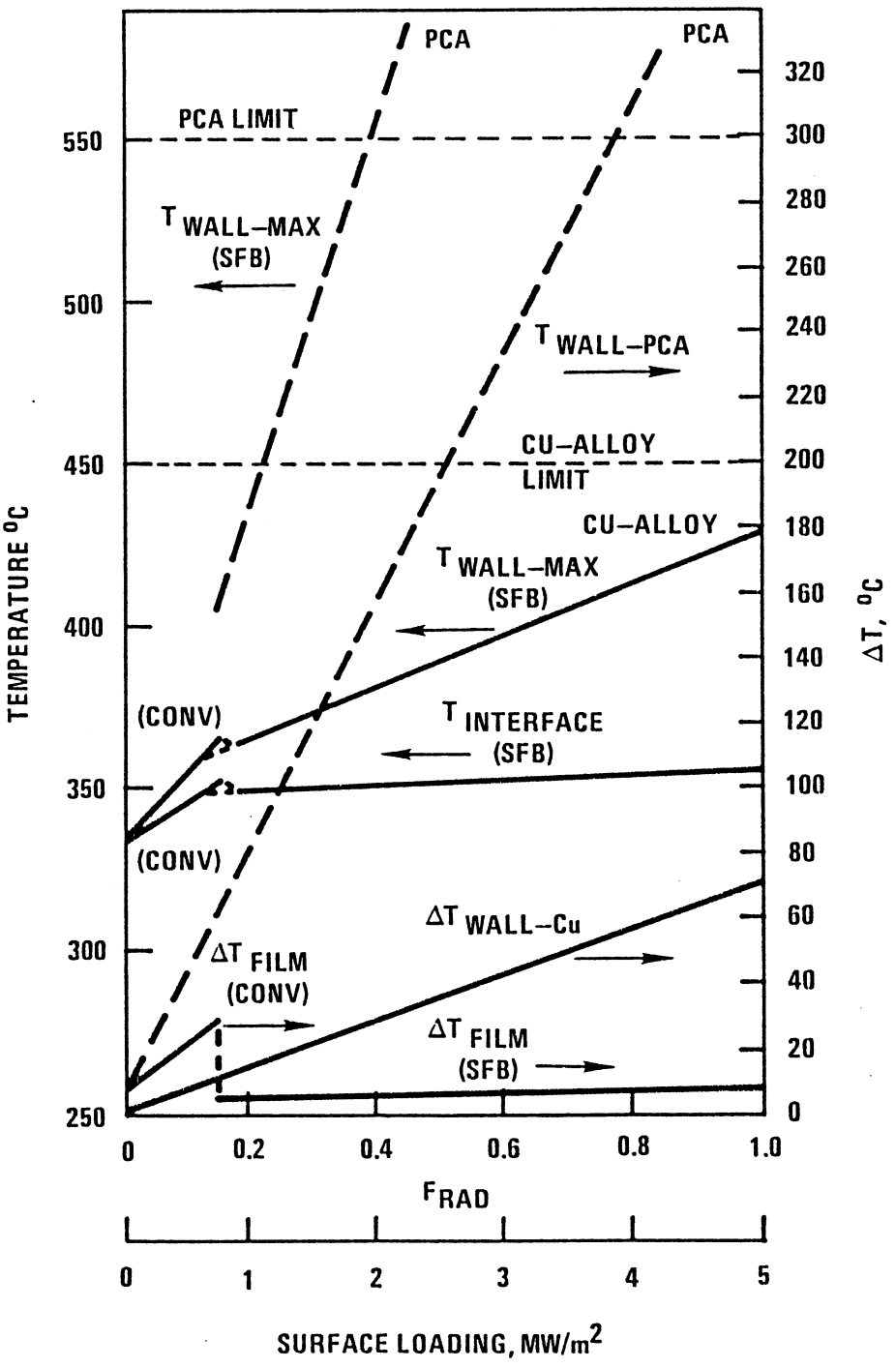

Fig. 8.3.-10. Temperature differences across first wall, water-wall interface temperature, and maximum wall temperature as a function of the first wall heat flux or the radiation fraction, f_{RAD} (CONV: convective heat transfer; SFB: Subcooled flow boiling heat transfer).

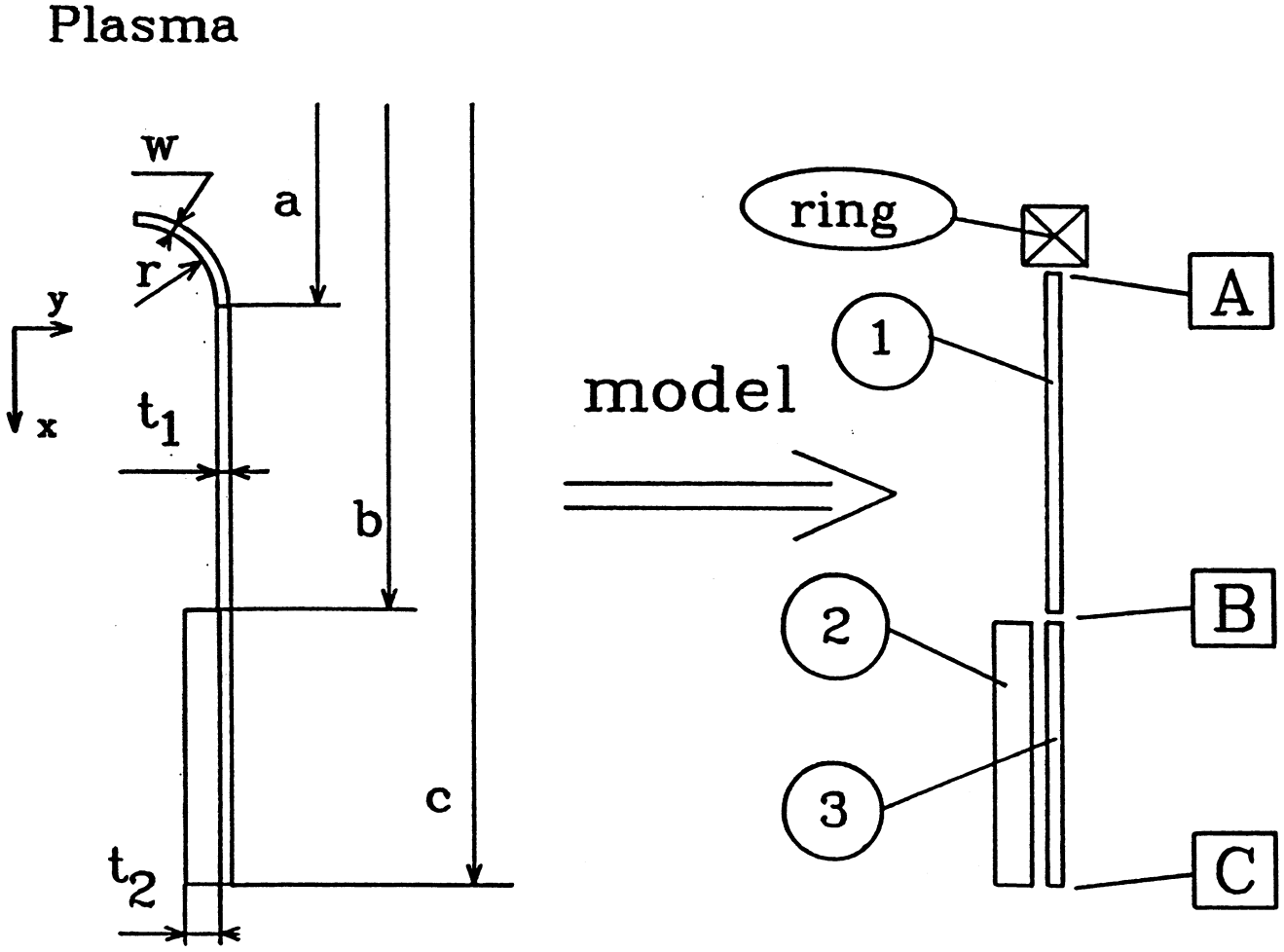

Fig. 8.3.-11. First wall structural analysis model for the aqueous blanket.

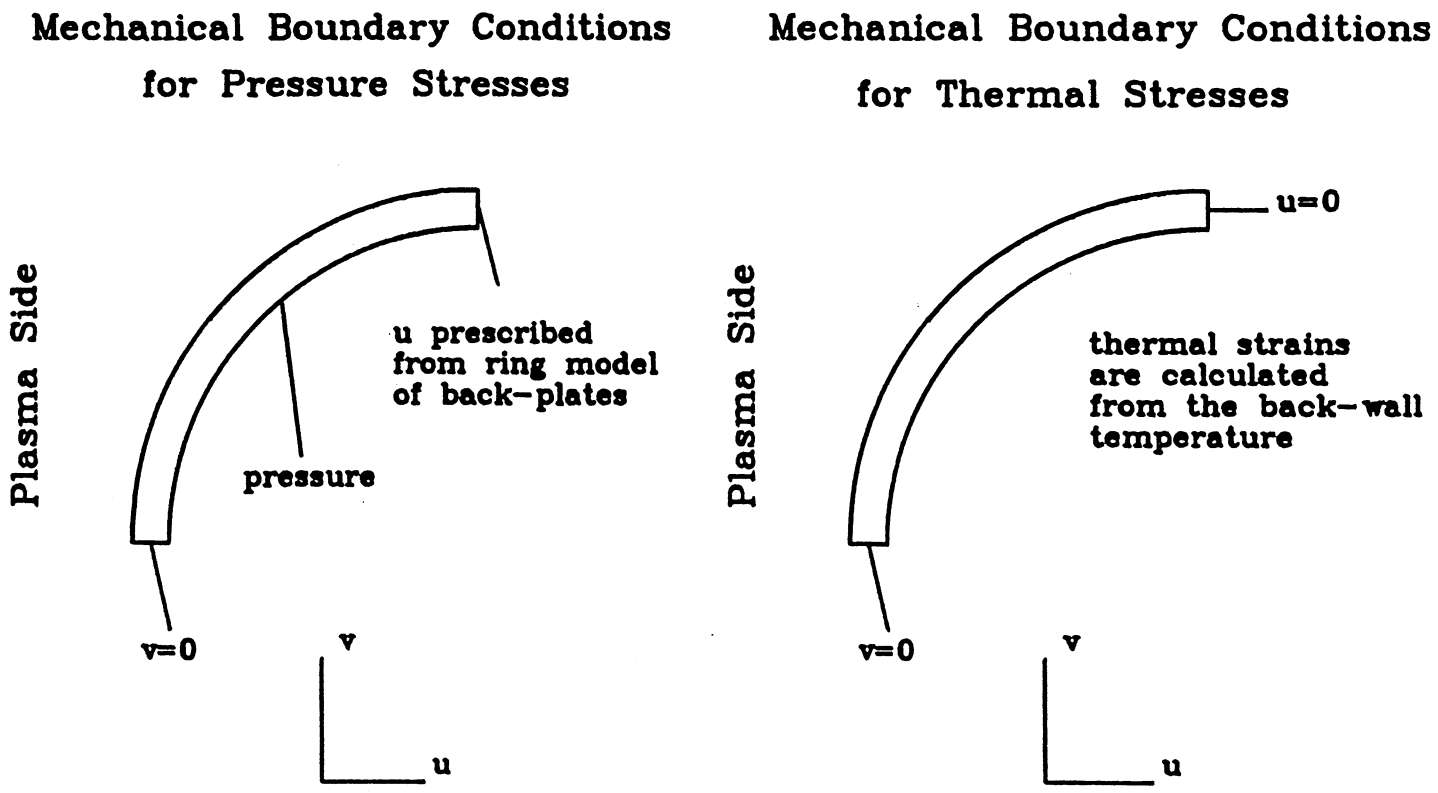

Fig. 8.3.-12. Boundary conditions for the stress calculation for the aqueous blanket design.

the reference temperature. Also, in calculating thermal stresses, the displacement boundary condition at the junction specifies no motion in the x direction rather than the displacement found calculating the pressure stresses. Heat-transfer boundary conditions are shown in Fig. 8.3.-13.

It is assumed for the buckling analysis that the first-wall lobes do not add significant resistance against buckling, thereby requiring that the annuli be stable under the pressure load. Two possible modes of buckling failure are a) collapse by circumferential creasing or b) an axisymmetric buckling mode when displacements perpendicular to the plane of the annulus become unstable. The critical loads for these modes are given by Timoshenko [49]. The axisymmetric buckling mode model, however, is overly conservative for the present design, since this model ignores the inward forces acting on the inner edge.

Pressure and thermal stresses in the inner first-wall poloidal ring structure are obtained by varying the thickness of the poloidal ring. When the displacement is artificially constrained at the junction of the stiffening ring, pressure stresses are marginally acceptable based on the 100 MPa allowable design limit for the Cu alloy. More realistic modeling accounting for the flexibility of the plates, however, will yield higher pressure stresses. The equivalent pressure stresses can be reduced to acceptable levels by simply increasing the poloidal ring radial dimension (Fig. 8.3.-14) and/or by connecting the first-wall structural poloidal rings to the back structure and prestressing, as is shown in Fig. 8.3.-15. The first-wall thermal stress was found to be acceptable even with high surface heat flux of 5.24 MW/m^2 (f_{RAD} = 1.0).

8.3.6. Tritium

Most blanket concepts seek to minimize the leakage of tritium into the water coolant because of the difficulty of isotopically separating small amounts of tritium. Tritium recovery from water, however, is a well-established technology, although the TITAN aqueous blanket design would demand an increased capacity from present systems. This situation is in contrast to proposed tritium-recovery systems for other blanket concepts, where the extraction technology is at best experimental, the demonstrated scale is orders of magnitude below that required for a fusion device, and the costing and attractiveness is correspondingly uncertain.

For the TITAN aqueous blanket design, tritium is extracted from water by first transferring the tritium into a hydrogen-gas flow, and then isotopically

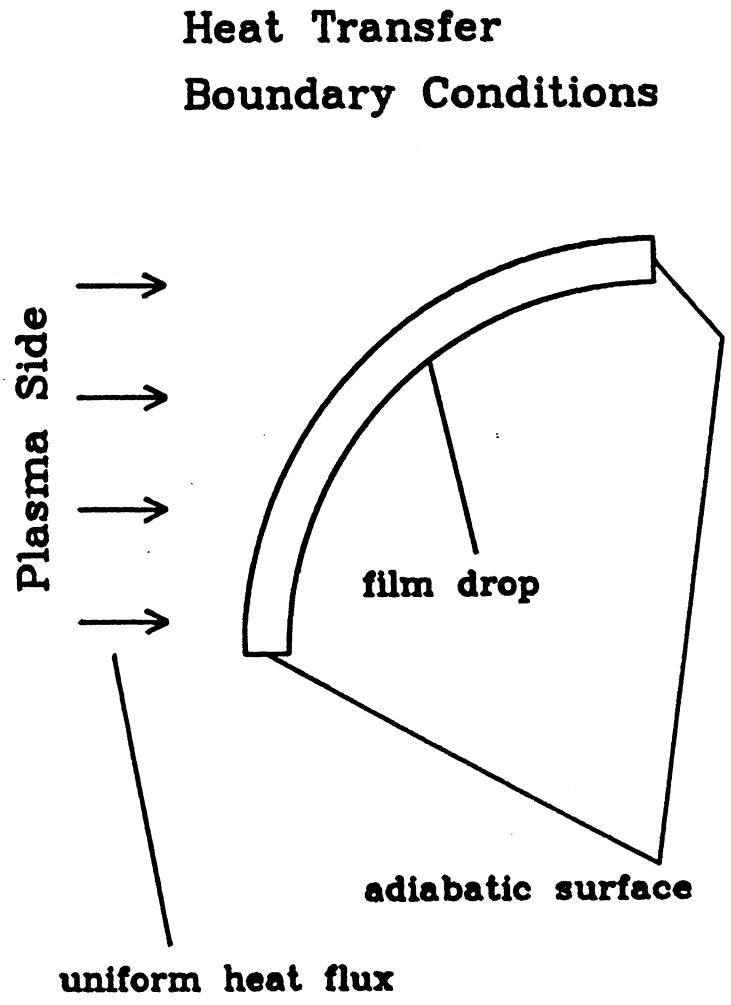

Fig. 8.3.-13. Boundary conditions for the heat transfer calculation for the aqueous blanket design.

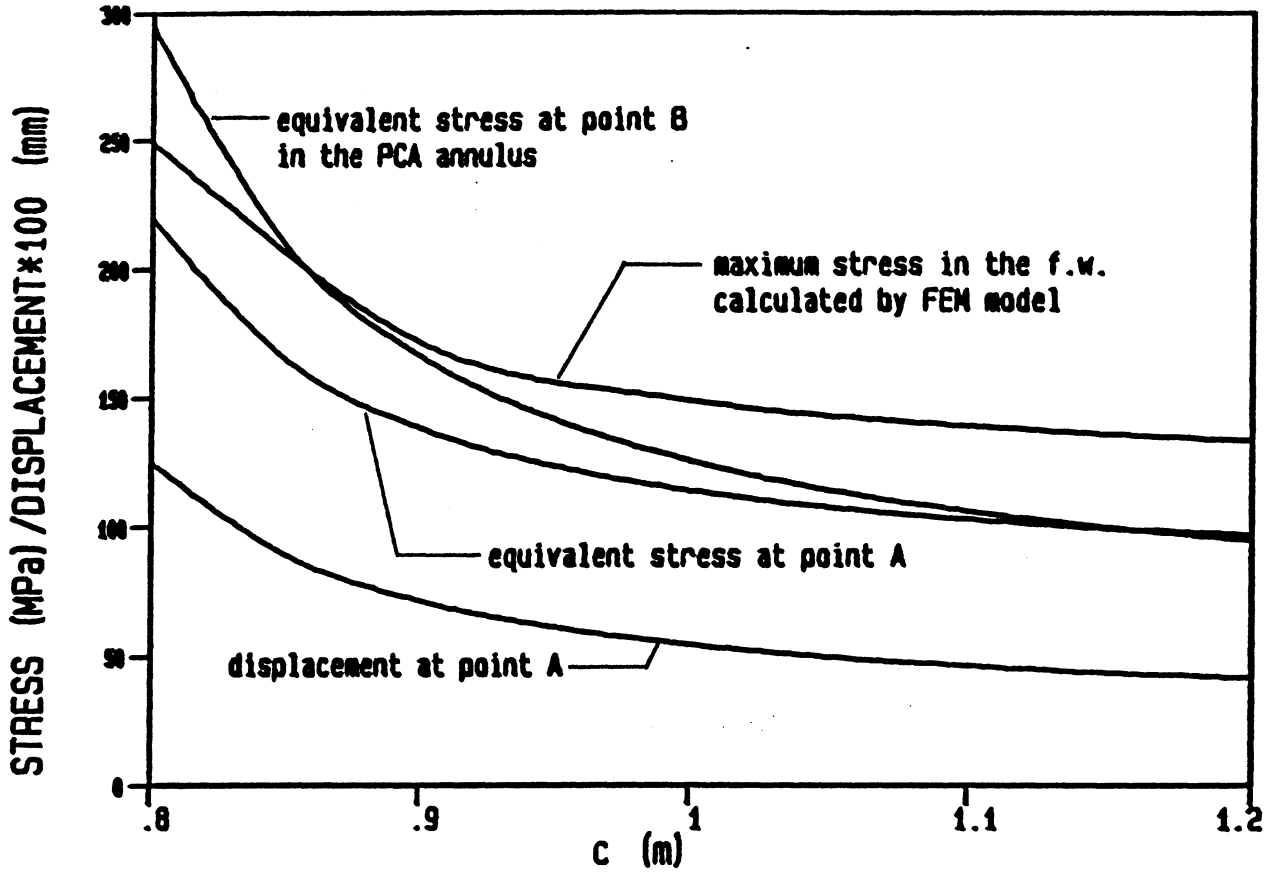

Dimensions: $a = 0.65$ m

$b = 0.72$ m

$w = 0.0015$ m

$t_1 = 0.002$ m

$t_2 = 0.0065$ m

$r = 0.01$ m

Load $p = 15.8$ MPa

$p_{pre} = 0$ MPa

c - Dimension from the plasma axis to the back of the first wall

Fig. 8.3.-14. Sensitivity of the structural response to changes in the dimension of the first wall and blanket segment.

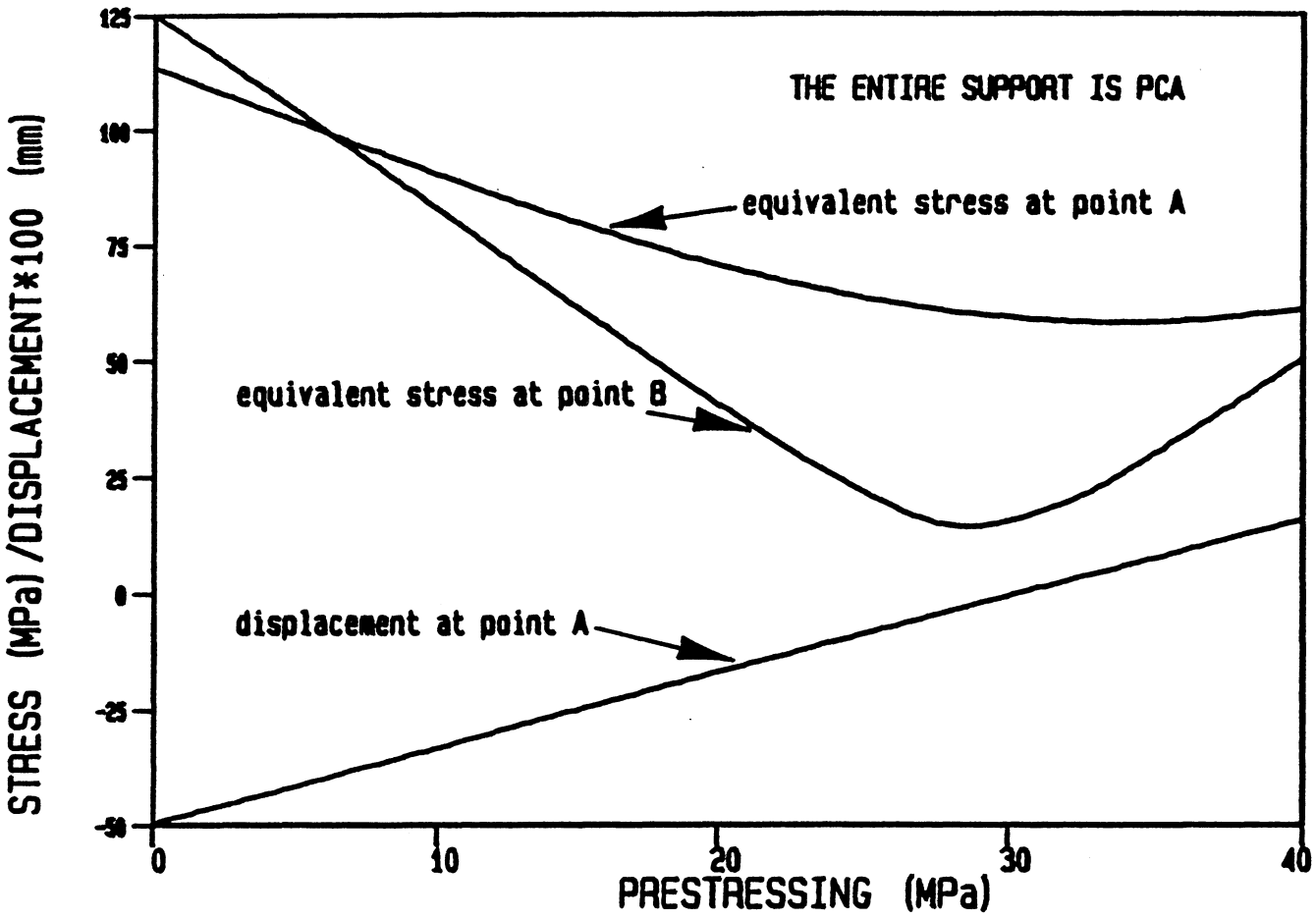

Dimensions: $a = 0.65m$ **Load** $p = 15.8$ MPa

$b = 0.72$ m

$c = 1.0$ m

$w = 0.0015$ m

$t_1 = 0.002$ m

$t_2 = 0.0065$ m

$r = 0.01$ m

Fig. 8.3.-15. Effect of prestressing on the stress levels which develop in the inner first wall poloidal ring structure.

separating the tritium. The preferred process depends on the tritium level, the water feed rate, and whether the feed stream is light or heavy water. For reactor systems, the options include pre-enrichment by Water Distillation (WD), followed by Vapor Phase Catalytic Exchange (VPCE), Liquid-Phase Catalytic Exchange (LPCE), Direct Electrolysis (DE), or a new combination called Tritiated Water Upgrading Process (TWUP) [50]. The isotope separation would best be accomplished by Cryogenic Distillation (CD). Some energy for electrolysis could be recovered by recombining the detritiated hydrogen with oxygen in a Fuel Cell (FC), or by selling the hydrogen as chemical feedstock.

For the 1000 MWe(net) TITAN reactor, the tritium production rate is about 120 kg/yr for an 80% availability. For average tritium levels in the water coolant of 10-20 Ci/l, the water feed rate to the tritium-extraction facility would be 8000-17,000 l/hr (500-1000 kmol/hr). For comparison, maintaining 0.1 Ci/l in a water-cooled solid breeder or liquid-metal blanket with 0.2-2 g/d permeation of tritium into the coolant [6,51] would require a water detritiation system with 44-440 kmol/hr water feed rate (the higher value assumes tritium permeation barriers are not successful). The plasma exhaust processing will use a CD system with a 0.1 kmol/hr throughput of DT.

Table 8.3.-V summarizes existing large-scale water isotope separation facilities. Both the VPCE and CD processes will be demonstrated on a large scale at the Darlington Tritium Removal Facility. The LPCE (and CD) process will be demonstrated on a smaller scale at the Chalk River Tritium Extraction Plant. Direct Electrolysis is a commercial technology at large feed rates without tritium and at modest feed rates with relevant tritium concentrations. Chalk River uses an electrolytic cascade process to enrich diluted reactor heavy water. These systems are not based on full electrolytic cells, in that they do not separate the oxygen and hydrogen, but they do provide experience with handling multiple cells and tritiated electrolyte. Water distillation is a mature technology at large feed rates. The Pickering and Bruce CANDU reactors have several WD-based heavy-water upgraders on-site. These systems process heavy water with tritium concentrations typical of those of the moderator or primary coolant. The Bruce plant produces heavy water from light water using WD. Although it does not contain tritium, the carrier/exchange gas is H_2S, which requires leak-tight design because of its chemical toxicity. Several fuel-cell demonstration units of 1-5 MWe capacity are in operation.

Several process combinations have been considered for TITAN, assuming either heavy or light-water coolant. A detailed description of these options is

TABLE 8.3.-V

PARAMETERS OF VARIOUS LARGE WATER PROCESSING SYSTEMS

Site	Feed fluid	Product fluid	Pro-Process	Feed rate (kmol/hr)	Startup date
Darlington (Canada)	D_2O	T_2	VPCE/CD	18	1987
Grenoble (France)	D_2O	T_2	VPCE/CD	1	1972
Chalk River (Canada)	D_2O	T_2	LPCE/CD	1	1987
Mound Lab (US)	H_2O	T_2	CECE/CD	0.06	1986
Chalk River (Canada)	D_2O	D_2	DE	0.13	1985
Chalk River (Canada)	D_2O/H_2O	D_2O	Electrolytic cascade	3-30	1950
Aswan Dam (Egypt)	H_2O	H_2	DE	1700	1984
Norsk Hydro (Norway)	H_2O	H_2	DE	180	1950
Pickering (Canada)	D_2O/H_2O	D_2O	WD	1-6	1972
Bruce (Canada)	H_2O	D_2O	H_2S Exchange	110,000	1975
Bruce (Canada)	H_2O	D_2O	WD	20	1975
Los Alamos (US)	DT	T_2	CD	0.02	1985
Tokyo (Japan)	H_2	H_2O	FC	150	1984

not included here. However, the direct installed cost for the tritium-extraction hardware for the aqueous blanket design has been estimated at between 80 and 150 M$ US (1986), depending on the particular cost and the assumed cost scaling. The corresponding energy requirement would include low-grade steam and electricity. The electricity consumption is generally larger and also more important, since low-grade steam can be readily available in a power reactor. Electric-power consumption is largest in electrolysis and cryogenic-distillation systems. A DE front end with no pre-enrichment for TITAN would require about 100 MWe. This energy could be partially recovered in fuel cells, or the hydrogen could be sold. Other alternatives that use VPCE, LPCE or WD front-end processes, alone or to enrich the feed stream before electrolysis, lead to overall system electricity requirements on the order of 30-80 MWe for TITAN. Both the capital and operating costs can be reduced by operating at higher tritium concentrations, scaling roughly as the square root of the tritium concentration. These cost estimates do not include advantages from integrating

the water-coolant system with others, particularly the waste-water treatment, plasma-fuel processing, and cryogenic refrigeration systems.

Control of the tritiated water coolant would be important, but only one part of the overall occupational and public safety aspects of the fusion device. Considerable nuclear utility operating experience with such tritium levels is available [52]. For example, the Pickering Nuclear Generating Station uses eight 550 MWe CANDU reactors. The heavy-water moderator (70°C and 0.1 MPa) contains 20-30 Ci/l tritium, while the heavy-water primary coolant (300°C and 10 MPa) contains 1.5-2 Ci/l. The total tritium inventory in the station is about 4 kg, and is located primarily in the moderator. This inventory is larger than in TITAN aqueous blanket. However, the total tritium-release rate from this multi-unit power station has averaged only 50 Ci/d in air and 50 Ci/d in water over the past several years. These tritium release rates are comparable to those envisaged as being allowable for a fusion facility.

In CANDU reactors, it is observed that a small number of components contribute the bulk of the leakage, and that leakage is related more to the component mechanical environment (e.g., closeness to pump vibrations, constantly cycling valves) than to temperature and pressure conditions. The dominant loss is through seals, as opposed to cracks or by permeation.

Many directions are possible for reducing water leakage from present CANDU levels. The improvements are being incorporated into the new reactors, and could certainly be used in a fusion reactor. These include [52,53] the following:

- Improve component testing procedures and leak-tightness requirements
- Improve installation during construction and maintenance
- Minimize piping joints and components, use welds where possible
- Make fixing of leaks a high maintenance priority
- Use live-loading and bellows seals on valves and flanges
- Improve room sealing
- Fill/empty drums using piping, avoiding air exposure.

The TITAN aqueous blanket allows convenient external control of the blanket tritium. For example, during the initial reactor commissioning phase, the blanket could use pure water to allow testing of plasma and heat-transport systems without tritium being present in the coolant circuits. Under these conditions, the salt could be gradually added until full operating conditions

were reached. During operation, the tritium-production ratio and recovery would be unaffected by partial power operation. During maintenance, the tritiated water could be removed from the blanket to a dump tank and replaced by cleaner (and possibly unpressurized) water, thereby minimizing tritium release during blanket replacement. Tritium levels in the reactor blanket could be externally controlled at any time by reducing the amount of lithium salt to minimize production.

8.3.7. Safety

The key distinction between the TITAN aqueous blanket design and conventional fusion reactor design is the cold pool of water at atmospheric-pressure selected for the submersion of the primary coolant loop, which includes the torus and primary heat exchangers. This cold pool is designed to handle the loss of coolant accident (LOCA) by diluting the energy content of the hot loop to low enough temperature (< 100 °C) such that significant radioactivity release by vaporization is impossible. The Cu-alloy first wall with its vertical flow configuration enhances natural convection in case of the loss-of-flow-accident (LOFA), as is shown in Fig. 8.3.-3.

Table 8.-VI summarizes various accident scenarios for the aqueous blanket design and the means by which inherent safety can be achieved, with detailed calculations and evaluations being needed. An interesting possibility for handling first wall and blanket, as indicated in Table 8.3.-VI, is by designing a thermally leaky primary loop; i.e., by making use of the temperature difference between the hot loop (300°C,) and the cold pool (30°C). The blanket afterheat power can be transferred to the cold pool by completely natural and passive means of conduction in the cold pool. To control the desired amount (< 5%) of steady state thermal power to be released, a stagnant layer of water at < 5 mm thick can be used as thermal insulation around the hot loop. Loss of high-temperature heat from the primary loop to the cold pool is wasteful, but there may be passive-safety advantages. More detailed analysis will have to be done to determine the minimum heat-loss rate during normal operation that will allow complete passive safety under accident conditions. It is estimated that at most, this will be a few percent of the full operating thermal power.

More detailed evaluations and calculations are needed to support the safety scenarios suggested in Table 8.3.-VI, but it seems that the aqueous blanket design has the potential to achieve level 2 of safety assurance.

TABLE 8.3.-VI
SAFETY SCENARIOS FOR THE AQUEOUS LOOP-IN-POOL BLANKET DESIGN

- Normal Operation
  - Active cooling.

- Loss of Primary Coolant Flow:
  - Natural circulation to primary HX (passive).

- Loss of Secondary Flow:
  - Natural circulation in secondary loop may be possible,
  - Conduction of primary loop through insulation to cold pool,
  - Natural circulation through cold pool safety loop.

- Loss of Primary and Secondary Flow:
  - Natural circulation in primary loop,
  - Natural circulation in secondary loop may be possible,
  - Conduction from primary loop through insulation to cold pool.
  - Natural circulation through cold pool safety loop.

- Loss of Secondary Coolant:
  - Conduction from primary loop through insulation to cold pool,
  - Natural circulation through cold pool safety loop.

- Loss of Primary Coolant Pressure:
  - Primary loop vents to cold pool,
  - Cold pool will reach 50 °C after mixing,
  - Cold pool can reach 100 °C after 5.8 weeks following shutdown (adiabatic),
  - Natural circulation through cold pool safety loop.

- Catastrophic Destruction of the Fusion Power Core:
  - Primary loop vents to cold pool,
  - Cold pool will reach 50 °C after mixing with hot loop,
  - Cold pool can reach 100 °C after 5.8 weeks following shutdown (adiabatic),
  - Earth as ultimate heat sink,
  - Potential release of only a fraction of hot loop tritium inventory (1.3 kg) due to transient events and diffusion.

8.3.8. Conclusions

The following features can be identified for the TITAN aqueous loop-in-pool blanket design:

1. Good combination of structural material and coolant to handle high surface heat flux of 5 MW/m^2 at steady state, because of the high thermal conductivity of Cu-alloy and the high heat flux capability of water-cooled SFB heat transfer. This feature is useful in the design of the divertor and other high-heat-flux components (i.e., divertor plate cooling).

2. Potential to achieve the Level 2 of safety assurance. The cold-water pool limits the potential release of radioactivity.

3. The technologies related to the use of Cu-alloy, PCA materials, aqueous breeder, pressurized-water power conversion, and tritium extraction, need less extrapolation from existing technologies than for most blanket designs, which can significantly impact the development cost of a commercial fusion reactor.

The power conversion performance of the aqueous blanket design measured by the product of blanket energy multiplication, M, and thermal power conversion efficiency is $1.45 \times 0.35 = 0.51$. This is quite good, despite the low power conversion system efficiency due to the good blanket energy multiplication.

Uncertainties that need to be addressed are: the irradiation properties of Cu-alloy at high fluence, the material compatability problems of aqueous lithium coolant with blanket materials, the cost of tritium extraction, and the further development of SFB heat transfer for the TITAN first-wall geometry.

8.4. FLIBE POOL DESIGN (IPFR)

8.4.1. Concept Description

The basic configuration of a fusion reactor blanket and shield has not been changed in the past three decades. Layers of structural material, including the first and/or second wall, blanket, reflector and shield are located between the plasma and magnets. Each subsystem has its own unique function and, therefore, unique design and possibly different structural material and coolant. For most cases, each subsystem is cooled by high pressurized coolant in long, small-sized, and thin-walled tubes. Very high reliability is required by each subsystem.

During the past few years, a number of innovative ideas have been developed to remove or combine reactor systems to simplify the reactor design and to improve the attractiveness of fusion. The integral pool fusion reactor (IPFR) has been developed as part of the TPSS program [54] with a similar spirit. The basic principle is to use FLiBe (Li_2BeF_4) to serve the multiple functions of cooling, breeding and shielding. If such a system can be proved feasible, significant improvements in the simplicity of the reactor systems would result.

The safety, reliability and maintainability of the nuclear island could also be improved.

The IPFR system concept is a pool-type configuration. The fusion power core, including only the first wall and the magnets, is submerged under a molten FLiBe pool as shown in Fig. 8.4.-1. The FLiBe will fill the space between the first wall and the magnets and will provide the necessary magnet protection. As such, the FLiBe serves the multiple functions of breeding, cooling and shielding eliminating the need for a separate blanket and shield. Therefore, the only structural layer remaining between the plasma chamber and the magnets is the first wall.

The FLiBe-to-FLiBe intermediate heat exchanger (IHX) is also located in the pool. The IHX is needed for safety and tritium containment. Since the working fluid is FLiBe on both sides of the IHX, the IHX can continue to operate with small leaks. One or more pumps are also submerged in the pool to generate a FLiBe flow upward around the first wall and downward through the IHX for the purpose of heat transport. By such design, the need for a primary loop is also eliminated.

The attractive features of the IPFR concept are as follows:

1. By eliminating a separate blanket, shield and the primary loop, the cost of the system can be reduced.

2. After draining the FLiBe, the first wall is exposed. The replacement of the first wall is easy. The amount of radioactive waste to be disposed is reduced.

3. Coolant connection in the reactor are not required. The IHX is from FLiBe-to-FLiBe and, therefore, can operate with leaks. The reliability of the blanket should be high.

4. A pool-type reactor has the potential to achieve Level 2 of safety assurance.

On the other hand, first wall cooling, corrosion, and tritium breeding, extraction, and containment are some of the critical issues for this concept.

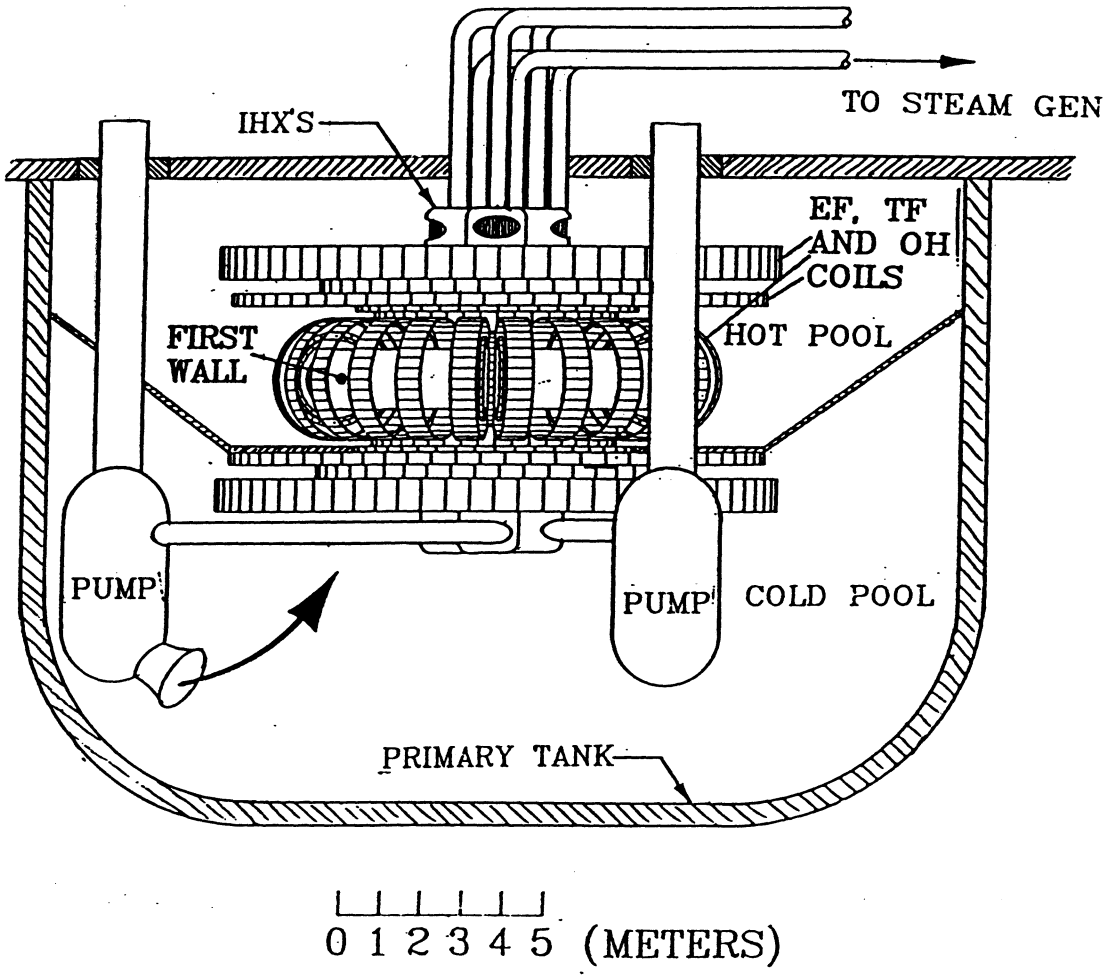

Fig. 8.4.-1. The FLiBe pool concept.

8.4.2. Materials

FLiBe is chosen as the tritium breeding material because of its low induced activation, low electrical conductivity, high-temperature stability and inertness toward air and water. However, some critical issues exist for using FLiBe. It has been generally accepted that FLiBe will not breed without additional neutron multiplier. However, in recent calculations [1], Cheng concluded that by careful material selection, FLiBe can yield a breeding ratio of 1.2. Other critical issues associated with FLiBe are corrosion and tritium containment. It seems that either the corrosion or the tritium containment problem can be handled, but it may be difficult to solve both simultaneously. A possible solution for tritium and corrosion has been developed and presented in Sec. 8.4.4, however.

A high-nickel alloy is the structural material for Molten Salt Breeder Reactor (MSBR) [55]; it is also a logical choice for the structural material for fusion application. Because of radiation-damage, however, a high-nickel alloy cannot be used in the fusion environment (i.e., close to the plasma chamber). The high-nickel alloy can still be used outside the neutron environment, (i.e., magnet casings, IHX, etc).

The preferred first wall material requires high operating temperature, long life, low neutron absorption cross-section, and low activation. A vanadium-based alloy fulfills most of these requirements and is chosen for the first wall.

Another important issue for the FLiBe pool is the question of Be resources. The U.S. and World reserves of beryllium have been recently estimated [56] and are listed in Table 8.4.-I. For the TITAN configuration, the total beryllium inventory is 230 tonnes, which should be compared to the beryllium burnup rate of 18 kg/year for a 1000 MWe (net) fusion reactor [1]. The FLiBe in the reactor, therefore, does not need to be reprocessed; one only has to make up for the burnup rate. Comparing the Be burnup rate with the Be resources of Table 8.4.-I shows that sufficient beryllium exists in the U.S. reserve for hundreds of 1000 MWe (net) reactors for an extended period of time.

Klein has pointed out that one of the problems in estimating the beryllium reserve is caused by the small demand [57]. The known reserve is disproportionally small compared to the abundance of the material. Erickson [58] reports that the potential recoverable resource for most elements in the earth's crust should approach

TABLE 8.4.-I
Be RESOURCES

TITAN FLIBE POOL:	
Total volume of FLiBe (m^3)	1,260.
Total mass of FLiBe (tonnes)	2,520.
FLiBe cost (M$)	95.
Be required (tonnes)	230.

BE RESOURCES:	U.S. Resource (tonnes)	World Resource (tonnes)
U.S. Bureau of Mines (USBM)	73,000. (320[a])	1,185,000. (5200[a])
U.S. Geological Survey (USGS)	282,000. (1200[a])	678,000. (3000[a])

[a] Number of reactors that can be built with the total resource.

$$R \text{ (tonnes)} = 2.43 \times 10^6 \, A \, , \qquad (8.4.-1)$$

where A is the abundance of material in the earth's crust in wppm, and R is the potential resource in tonnes. Table 8.4.-II lists the reserves and potential resources for different materials. For materials in greatest demand, the ratio is close to 1 but for beryllium the ratio is about 100. It is reasonable, therefore, to speculate that at least 10 times as much beryllium as the reserve number may be available. If this is the case, sufficient beryllium will be available for a fusion economy.

8.4.3. Thermal Hydraulics

The first-wall cooling is an inherent problem associated with the pool configuration. It is difficult to force the coolant to the first wall in such an open geometry. A finite-element analysis of heat transfer in a pool configuration with an unrestricted first wall is in progress, with some encouraging results reported [59].

A baffled first wall can also be used to enhance the first-wall cooling, as shown in Fig. 8.4.-2. The concept involves a first-wall channel with a 10 mm gap. The first-wall channel rests on a supporting structure with a flow restriction device to limit the coolant flow in the back of the blanket. The

TABLE 8.4.-II

Abundance-Reserves-Resources Relationship in U.S. and Earth Crust[9]

Element	United States			World		
	Reserve[a] ($MTx10^6$)	Recoverable Resource Potential[c] ($MTx10^6$)	Ratio of Potential to Reserve	Reserve[b]	Recoverable Resource Potential[c]	Ratio of Potential to Reserve
Lead	31.8	31.8	1.0	0.54	550.0	1000
Copper	77.8	122.0	1.6	200.0	2120.0	10
Zinc	31.6	198.0	6.3	81.0	3400.0	42
Silver	0.05	0.16	3.2	0.16	2.75	18
Gold	0.002	0.0086	4.1	0.011	0.15	14
Molybdenum	2.83	2.7	1.0	2.0	46.6	23
Beryllium	0.073	3.7	50.0	0.016	64.0	4000
Beryllium	0.025[d]	3.7	148.0	0.38[d]	64.0	170

[a]U.S. Bureau of Mines (1970).

[b]U.S. Bureau of Mines (1970), does not include U.S. reserve.

[c]Recoverable resource potential = 2.45 A x 10^6 (abundance A expressed in g/mt).

[d]U.S. Bureau of Mines (1982).[3]

pressure balance, in this case favors coolant flow to the first wall. Table 8.4.-III lists the thermal-hydraulic parameters for the first wall region. The maximum heat flux capability of this design is about 1.3 MW/m^2.

The design goal for TITAN is a neutron wall load of ~ 20 MW/m^2. It is not clear that a FLiBe pool will be able to handle the surface heat load associated with such a high neutron wall load. It should be pointed out that the thermal conductance of a 2 mm thick wall structure is 1.3×10^4 W/m^2K, which is comparable to the heat transfer coefficient of FLiBe. Any improvement of the heat transfer coefficient of the pool coolant, whether it is FLiBe, water or other fluids, is not effective as long as the first wall is a vanadium alloy because the heat transfer is controlled by thermal resistance of the structure.

8.4.4. Material Compatibility and Tritium Containment

The problems associated with corrosion and tritium containment may be resolved by formation of a molybdenum coating on the surfaces of the structural components. The formation of the coating has been demonstrated at ORNL by dissolving MoF_6 in FLiBe [60]. Table 8.4.-IV lists the free energy of formation of different fluoride compounds. It can be seen that MoF_6 is the most unstable of all the listed materials. Therefore, V, Ni and tritium will react with MoF_6 to form VF_4, NiF_2 and TF, respectively. In reaction with V or Ni, the Mo is precipitated out and forms a continuous coating to prevent further reaction. If the MoF_6 concentration is carefully monitored, then this coating is self

TABLE 8.4.-III
PARAMETERS OF THE BAFFLED FIRST WALL

Surface heat flux (MW/m^2)	1.3
Volumetric heat generation (MW/m^3)	150.
First wall channel width (mm)	10.
First wall channel length (m)	2.
Coolant temperature (°C)	550./600.
Coolant velocity (m/s)	2.23
Heat transfer coefficient (W/m^2K)	1.37×10^4
Coolant pressure drop (MPa)	0.03
Maximum interface temperature (°C)	690.
First wall thickness (mm)	2.

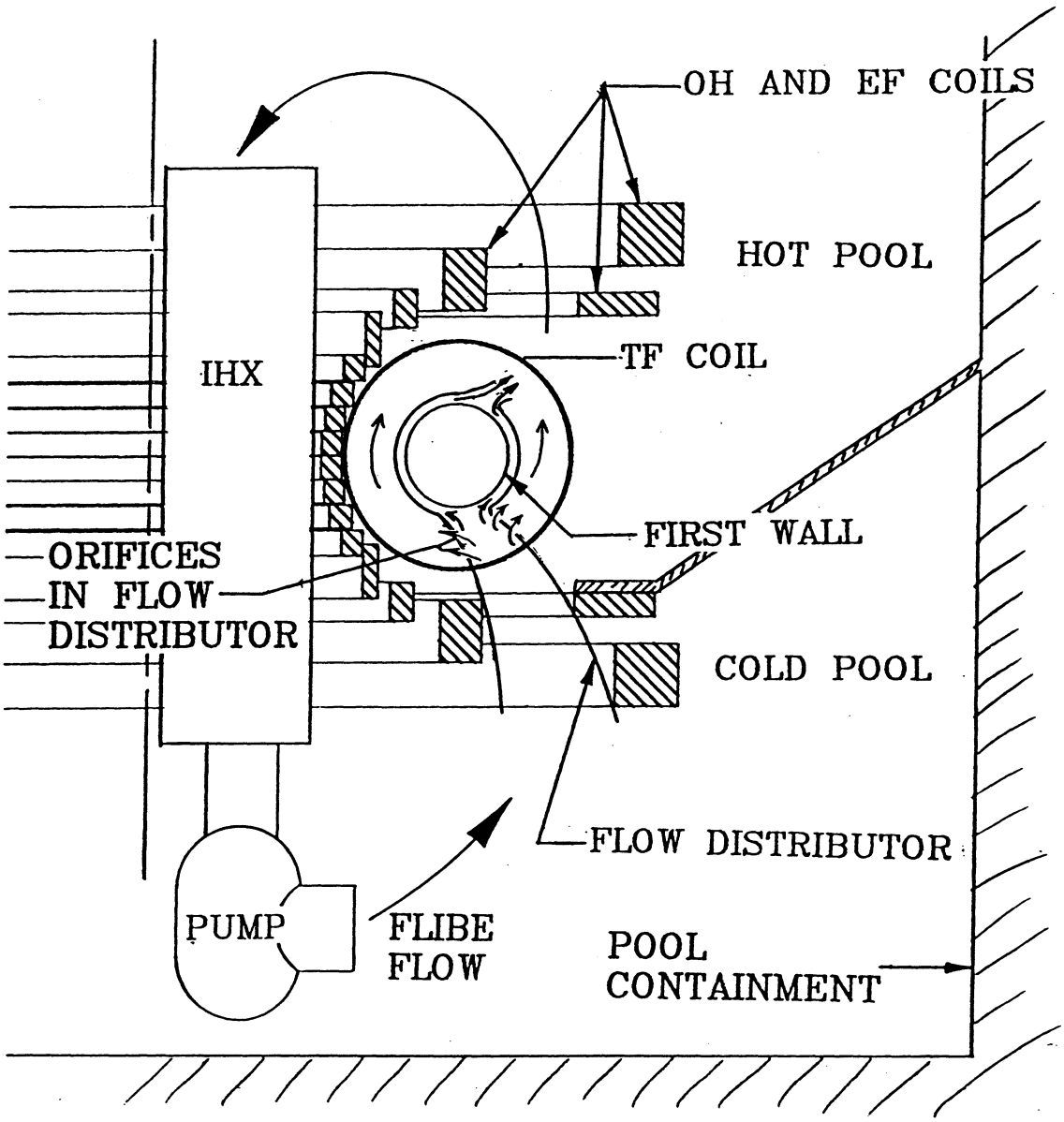

Fig. 8.4.-2. Baffled first wall cooling scheme for FLiBe pool concept.

TABLE 8.4.-IV

FREE ENERGIES OF FORMATION OF FLUORIDES

	ΔG^f at 1000 K (kcal/g-atom of fluorine)
MoF_6 [a]	-50.2
WF_6 [a]	-56.8
NiF_2 [b]	-55.3
VF_5 [a]	-58.0
VF_4 [c]	-66.0
HF [a]	-66.2
FeF_2 [b]	-66.5
NbF_5 [a]	-72.5
CrF_2 [b]	-75.2
TaF_5 [a]	-82.5
TiF_4 [a]	-85.4
LiF [d]	-125.2
BeF_2 [d]	-106.9

a) Gaseous.
b) Dissolved (aqueous).
c) Crystalline.
d) Liquid.

healing. The formation of TF will greatly reduce the mobility of tritium and reduce its permeation rate.

The pressure ratio of TF to that of T_2 can be calculated by the free energy of formation and is summarized in Table 8.4.-V. If 1 ppm of MoF_6 is dissolved in FLiBe, then the partial pressure of T_2 is 10^{-8} Pa, and tritium permeation is no longer important. If the MoF_6 concentration is higher, the situation is more favorable. The total tritium inventory in the reference design is 6 g, which can be relaxed by a factor of 10.

TABLE 8.4.-V
TRITIUM SUMMARY

X_{MoF_6} (ppm)	1.
P_{TF} (Pa)	13.
P_{T_2} (Pa)	1.7×10^{-8}
Tritium inventory (g)	5.
Tritium leakage rate (Ci/d)	4.
Purge gas flow rate (l/s)	$\sim 10^3$

8.4.5. Safety

The combination of the material selection and the configuration of the IPFR provides this reactor concept with a large safety margin. The control of the tritium is a key safety concern with the use of FLiBe. As has been discussed earlier, the addition of MoF_6 is expected to reduce the scope of this problem considerably.

For most fusion reactor systems, thermal transients may lead to the release of considerable amounts of radioactivity from the reactor. The use of the pool configuration together with structural and breeding materials with low decay heat minimizes the potential problems associated with thermal transients. The establishment of natural convection in the blanket region, made possible by the open configuration, makes the problem of thermal transients even less threatening.

FLiBe has no exothermic reactions with water or air and is unlikely to have any significant reaction with concrete. This lack of reactivity is a distinct advantage over either lithium or $Li_{17}Pb_{83}$-cooled blankets. Furthermore, FLiBe has low electrical conductivity, and MHD problems are eliminated. Therefore, FLiBe has the advantages associated with these liquid metal blankets (e.g., combined coolant and breeder functions) without the potential problems of the chemical reaction or MHD effects.

The degree of safety involves the level of protection which a reactor concept can provide to the public. Since the IPFR concept has no chemical or thermal transient problems, a high level of safety can be assured. In fact, there may not be any plausible pathway for radioactivity mobilization which

could be sufficient to cause any acute fatalities. Therefore, the FLiBe pool design has the potential to achieve Level 2 of safety assurance.

8.4.6. Conclusions

A unique concept of improving the attractiveness of fusion, the FLiBe pool design, was described in this section. The concept has the potential to significantly improve the safety, simplicity, reliability and maintainability of a typical fusion reactor. However, this concept is still in the development stage, feasibility issues remain, and applicability to high wall loading (>10 MW/m^2) and high surface heat flux (up to 4 MW/m^2) reactors is limited by heat transfer considerations.

8.5. HELIUM-COOLED CERAMIC DESIGN (FISC)

8.5.1. Concept Description

The Fusion Inherently Safe Ceramic design (FISC) is based on the Low Activation Fusion Reactor concept pioneered by G. Hopkins [61]. The low activation concept attempts to use materials in the regions of the reactor that are exposed to a significant fluence of neutrons, that exhibit only a low level of short-lived activation if exposed to fusion neutrons. If this can be done, then significant safety, maintenance and waste management advantages may be achieved [62]. If the total hazard inventory and afterheat level can be kept low enough that no significant dose would occur at the site boundary, regardless of what happened to the physical integrity of the reactor, then many or even all of the N-stamp requirements imposed on fission reactors would be unnecessary. Avoiding these requirements could result in an approximately 30% savings in the capital cost of the plant [63].

The materials choices that will allow very low activation to be achieved are very limited. Only low-Z elements such as H, He, B, Be, C, Li, Si, O may be used in the high flux zones. This restricts the materials choices. Previous studies [61] have concluded that the most promising possibility is SiC as the structural material, solid lithium compounds for breeding tritium and helium as the coolant. The FISC design started with this concept.

The FISC concept places the fusion power core and high-pressure-helium primary heat transport loop inside a prestressed concrete reactor vessel (PCRV) filled with pressurized helium as shown in Fig. 8.5.-1. This configuration places the first wall/vacuum chamber torus under a compressive load.

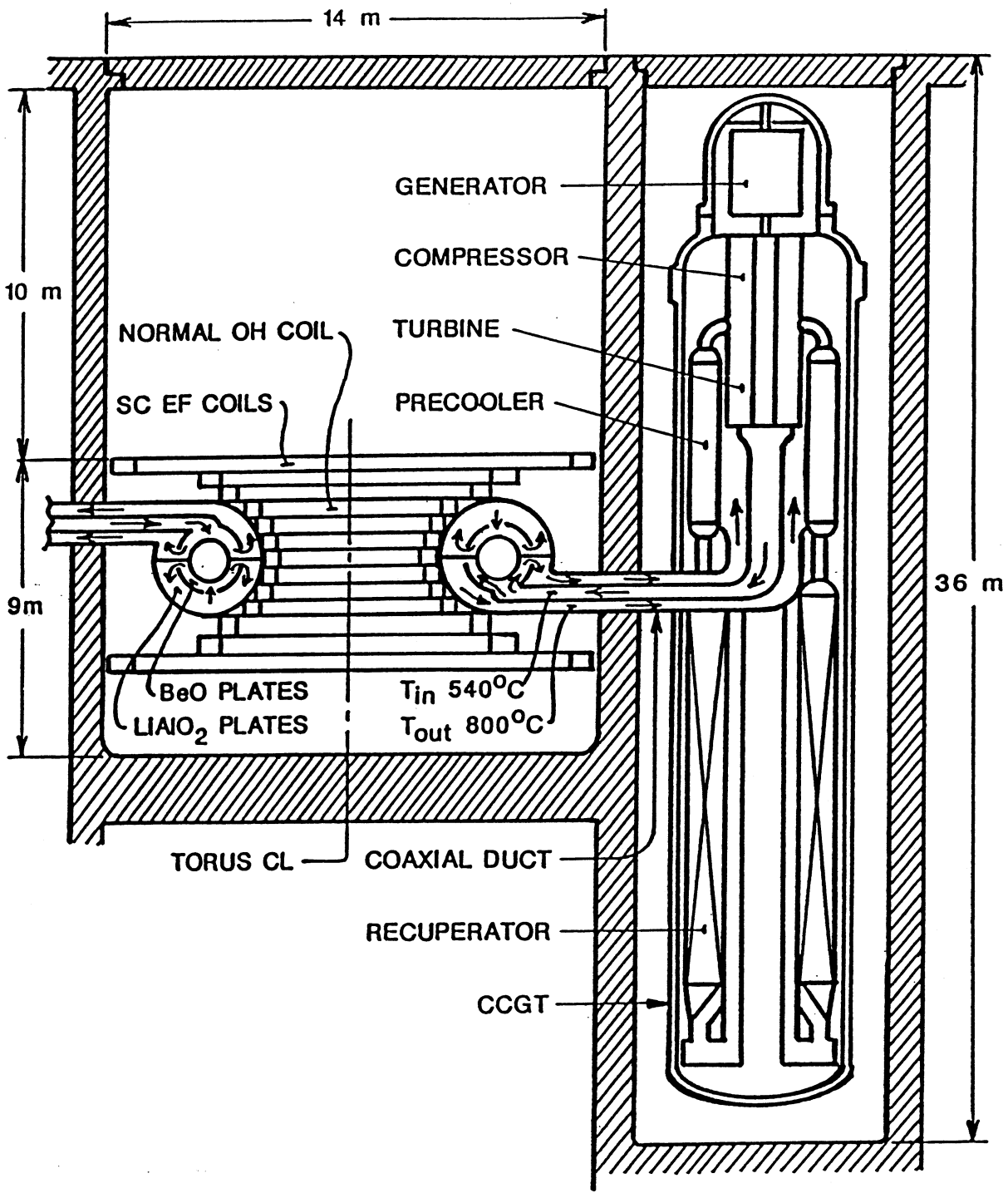

Fig. 8.5.-1. Helium-cooled ceramic blanket (FISC) Design.

Furthermore, the entire primary loop is under the same compressive, load which balances the tensile load created by the high pressure, high temperature helium coolant. The result is a ceramic design with only compressive primary stresses (Fig. 8.5.-2).

The TITAN FISC design characteristics are given in Table 8.5.-I. To take advantage of the high temperature capabilities of the helium-cooled ceramic design, a Closed-Cycle Gas Turbine (CCGT) power conversion system is used. This concept has been developed for use with the advanced high temperature gas-cooled fission reactor (HTGR) and is integrally located inside the PCRV. It is ideally suited for coupling to the FISC reactor [64].

For the 20 MW/m^2 TITAN strawman design, the vacuum chamber is of sufficiently high aspect ratio to allow fairly uniform compressive stresses to be developed. The torus, however, is divided by the four divertors, requiring that an extra load path be provided to support the major axis compression. As proposed, this configuration consists of two rings at a tangent to the top and bottom surface, as is shown in Fig. 8.5.-3, on to which the four toroidal segments can butt; an abutment face is provided on the chamber top and bottom tangent points. The butting force is 0.876 MN/m (5000 lb/in), which will require grinding of the mating surfaces. Temperature control or slitting of the ring will avoid thermal stress problems. It is proposed that the torus be composed of 0.5 m long poloidal rings (Fig. 8.5.-2). The first wall cooling passages must be incorporated in the "green" stage of the ceramic manufacturing, using a non-refractory filler which melts out in subsequent firing of the composite. Joints between these rings will require reliable SiC braze joints but brazing of SiC to a metal has been demonstrated.

The pressure-induced compressive stress on the ring is 145 MPa. The tensile stress in the axial direction that is induced by the divertor chamber is similar in magnitude in the smallest sections. Because of its shape, the divertor shell carries its load as a beam, one support being at the outside diameter and the other at the torus intersection. The supports will tend to provide some bending support, but this situation is undesirable because of the vacuum sealing requirement. The beam stiffness is such that the joints will not rotate significantly. To achieve this, the depth of the divertor beam (wall) must be at least 80 mm thick, as is shown in Fig. 8.5.-3.

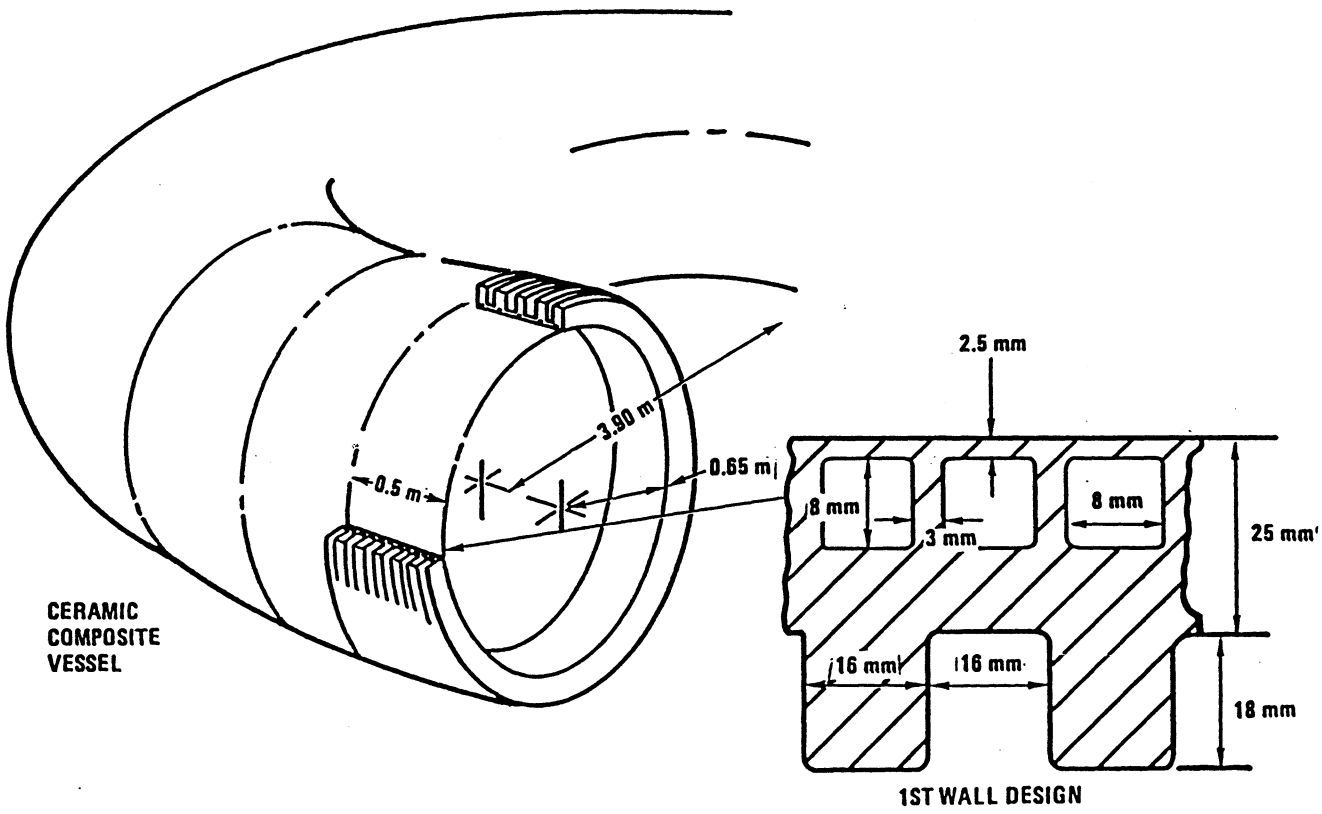

Fig. 8.5.-2. FISC ceramic first wall torus which is compressively loaded.

TABLE 8.5.-I
CHARACTERISTICS OF TITAN FISC DESIGN

Major radius (m)	3.9
Minor first wall radius (m)	0.65
Neutron wall loading (MW/m^2)	20.0
Surface heat loading (MW/m^2)	1.5
Thermal power (MW)	2,351.
Net electric power (MW)	1,000.
Tritium breeder	Solid breeder
Neutron multiplier	BeO
Tritium breeding ratio	1.17
Blanket energy multiplication	1.20
Coolant	Helium at 5 MPa
Inlet temperature (°C)	540.
Outlet temperature (°C)	800.
First wall material	SiC
Structural material	SiC
First wall thickness (mm)	1.9 to 2.5
First wall temperature, peak (°C)	1,198.
Power conversion system thermal efficiency	40%

8.5.2. Material

Desirable characteristics of ceramics used as structural material for fusion applications are: (1) high strength at high temperatures; (2) high elastic modulus; (3) electrical properties range from insulator to semiconductor and can be tailored by dopants; (4) fabrication of odd shapes can be handled; (5) low density. Table 8.5.-II summarizes some of the physical properties for monolithic SiC. On the other hand, some of the undesirable characteristics are: (1) brittle fracture; (2) unpredictable failure point (the fracture tensile strength has a wide statistical distribution); (3) failure is usually catastrophic with rapid crack propagation through the stressed region. By using a ceramic/ceramic composite, both the unpredictability and catastrophic nature of failure can be avoided. The lack of strong bonding between the fiber and the

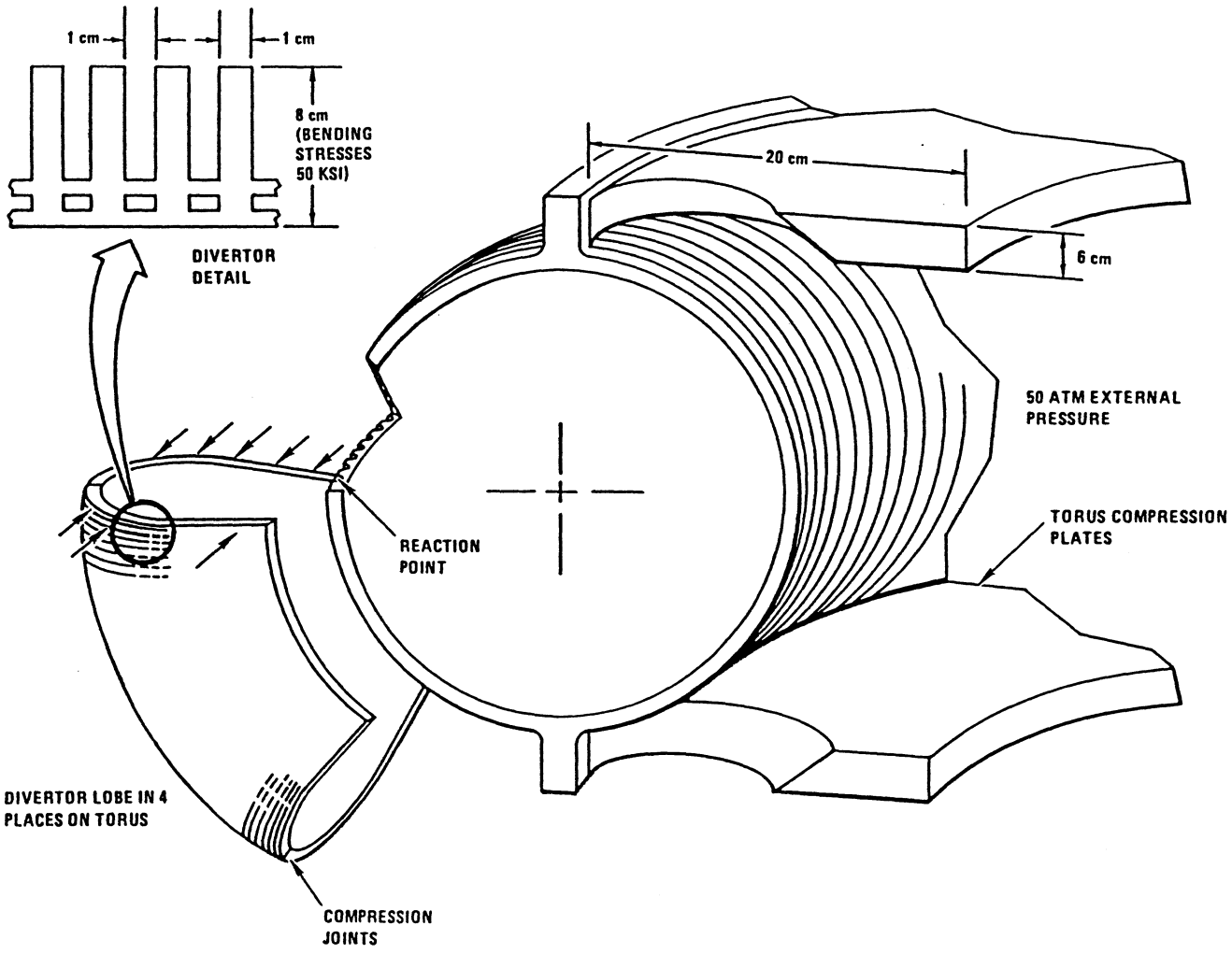

Fig. 8.5.-3. Ceramic divertor design.

TABLE 8.5.-II
PHYSICAL PROPERTIES OF SiC AT 1000°C [65]

Melting point (i.e., decomposition, °C)	2600
Specific heat (J/kg°K)	1286
Density (Mg/m^3)	3.21
Coefficient of thermal expansion ($10^{-6}/K$)	4.9
Thermal conductivity (W/mK)	50
Young's Modulus (GPa)	360
Flexural strength (MPa)	500-1000

matrix forces both fiber and matrix to behave somewhat independently as far as crack propagation is concerned.

8.5.2.1. Manufacturing

The manufacturing process for SiC/SiC composite components is well developed using the chemical vapor infiltration (CVI) process. First, a preform of the component (tube, sphere, dome, torus etc.) is woven from SiC fibers. The preform is then suspended in a CVI-furnace. Chlorinate silanes (silicon source) and hydrocarbon gas (methane, ethane, propane; carbon source) are vented into the CVI-chamber. Silicon and carbon infiltrate the fiber preform and combine to create the SiC matrix imbedding the fibers. Reaction rates, bonding strength between fiber and matrix, and matrix density are controlled with furnace temperature and by using a cover gas (argon) to regulate flow rates. Matrix densities of 95% theoretical SiC density have been achieved using CVI.

The composite nature allows a high degree of predictability, which enhances reliability in structural designs. Three-point bend tests have shown that the composite fracture characteristic results from the independent fracture of fiber and matrix. The matrix cracks propagate up to the fiber and either stop or run along the fiber direction. This structural independence leads to "fiber-pullout" from the matrix upon fracture.

8.5.2.2. Composite Material Description

The NIPPON Carbon Corp. of Japan has been successful in producing long SiC fibers (NICALON). These fibers have ~12 μm diameter and can be woven

successfully into two-dimensional patterns. Shapes of performs manufactured are circular and hexagonal cross sectional (thin walled) tubes, domes, and nozzles.

Tests on the physical property of the SiC/SiC-composite material has shown that the limiting strengths were tensile not compressive (compressive strength is about 3 to 4 times that of tensile). Upon fracture, the ends of fibers extended into the matrix, which implies that some fiber-matrix frictional forces exist, which can be tailored by CVI control. Table 8.5.-III summarizes some of the physical properties measured during CVI process development [66]. Apparently, in these measurements, the ultimate bend strength of the composite is a factor of 5 to 6 lower than that of individual fibers. This difference may be due to the fact that the CVI-process is still in the development phases. Thus, improvements in CVI-processes and optimum fiber strength utilization, therefore, promise even better physical properties.

8.5.2.3. Irradiation Effects

Chemical Vapor Infiltration of SiC consists of high-density β-SiC, which tends to be stable under irradiation because of the cubic crystal structure. However, the irradiation behavior of SiC/SiC-composites is not known.

TABLE 8.5.-III
SiC/SiC COMPOSITE PHYSICAL PROPERTY DATA [66]

	Unidirectionally Wound, 1-D	Two-dimensional Braid, 2-D
SiC/SiC Composite (~ 50% Fiber by volume):		
Ultimate bend strength, MPa (ksi)	620 (90)	350 (50)
Elastic modulus, GPa (Mpsi)	240 (35)	240 (35)
Strain to failure	~ 1%	1-2.5%
Linear elastic limit	0.1-0.4%	0.1-0.4%
Density, Mg/m^3	2.5	2.5
Nicalon SiC fibers (ceramic grade):		
Tensile strength, MPa (ksi)	3290 (470)	
Elastic modulus, GPa (Mpsi)	245 (35)	
Density, Mg/m^3	2.6	

Silicon-Carbide shows a good retention of strength under irradiation. The dimensional stability under irradiation is optimum around 1000°C with a linear expansion of 0.1% or less at fluences exceeding 10^{26} n/m^2 [64]. The most drastic effect of fast neutron irradiation is the reduction of thermal conductivity. Several authors have measured an 80% reduction of thermal conductivity after irradiation to 2×10^{26} n/m^2 at 540 to 740°C [64]. Recent experiments at room temperature indicate an increase in thermal conductivity of SiC from 50 W/mK to 270 W/mK with the addition of 2 at.% BeO to the SiC. Higher temperature results for this material are also encouraging. Irradiation effects on this mixed ceramic at high fluence will be evaluated in the future [66].

Silicon Carbide is considered as a structural material for FISC because of its thermal stress resistance, strength, creep resistance, irradiation stability, commercial availability, shaping capability and tritium retention. Low activation makes this material very attractive from a maintenance and waste management point of view; and low afterheat promise the potential for a high level of safety assurance [67].

8.5.3. Thermal Hydraulics

The thermal hydraulics analysis of the FISC design has used standard heat transfer and pressure drop correlations to evaluate a suitable helium flow path and peak temperature levels throughout the first wall and blanket area. The power rating and geometry are based on a 19 MW/m^2 neutron wall load design. With a blanket energy multiplication of 1.2, the total first wall and blanket power is 2803 MWt. Helium at inlet pressure of 5 MPa and temperature of 813 K and outlet temperature of 1073 K is circulated through the torus assembly. These temperature levels were selected to achieve an efficient power conversion [68] with a He flow rate of 8123 kg/s. Four parallel modular power conversion systems, one for each torus quadrant, share this mass flow. For this calculation, $LiAlO_2$ was chosen as the solid breeding material, because of a high temperature capability (1000°C). In retrospect, $LiAlO_2$ has the drawback of relatively high afterheat and induced radioactivity. Solid breeders such as Li_2O, Li_2SiO_3, Li_4SiO_4 and Li_2TiO_3 should be evaluated.

The cross-section of each torus quadrant is divided up into four poloidal route sectors. Figure 8.5.-4 shows the configuration and helium flow paths for one of these sectors. The coolant flows in the poloidal direction in the first wall channels as well as in the gaps between the multiplier and breeder plates. The helium flow enters radially and splits into two streams (routes A and B in

Fig. 8.5.-4). The multiplier route, A, cools the 100 mm deep breeder zone located nearest to the plasma (solid breeder zone I) on the way back to the manifold. Route B cools the first wall and returns in a parallel flow through solid breeder zone II (300 mm deep) and solid breeder zone III (400 mm deep). The high local surface heat fluxes in the rectangular coolant channels, which are integrated in the first wall, require high velocity and, therefore, cause the dominant pressure drop in first wall channels. However, combining this pathway with the low-power solid breeder zones II and III allows the pressure differential in the primary system to be held below 4% of the system pressure of 5 MPa. The pressure drops are calculated for average conditions of the respective zone (Fig. 8.5.-5 and Table 8.5.-IV). These values do not include additional losses associated with bends and turns, as well as 3-D effects related to the poloidal flow.

The one-dimensional heat transfer calculations are made at critical locations, (i.e., evaluation of peak temperatures in the first wall and the multiplier/breeder plates). Of primary concern is the first wall, which is exposed to a 1.5 MW/m^2 surface heat flux (corresponding to a radiation fraction of $f_{RAD} = 0.3$). An additional 0.4 MW/m^2 is added to simulate the volumetric heating in the coolant channels near the plasma. With high coolant velocity,

TABLE 8.5.-IV

THERMAL HYDRAULICS PARAMETERS OF THE FISC DESIGN

			Solid Breeder		
	First Wall	Multiplier	Zone I	Zone II	Zone III
$\dot{Q}$ (MW)	230	1028	760	331	116
Power fraction	9.3%	41.7%	30.8%	13.4%	4.7%
T_{in} (K)	813	813	946	946	946
T_{out} (K)	946	946	1073	1073	1073
$\dot{m}$ (kg/s)	333	1490	1148	500	175
$\bar{V}_{He}$ (m/s)	215.	83.2	100.	14.5	9.5
ΔP_{He} (MPa)	0.1416	0.0310	0.1086	0.0011	0.0012
k (W/m-K)	16.0	15.0	1.0	1.0	1.0
T_{limit} (K)	1475	1760	1275	1275	1275
T_{max} (K)	1466	1053	1271	1276	1274

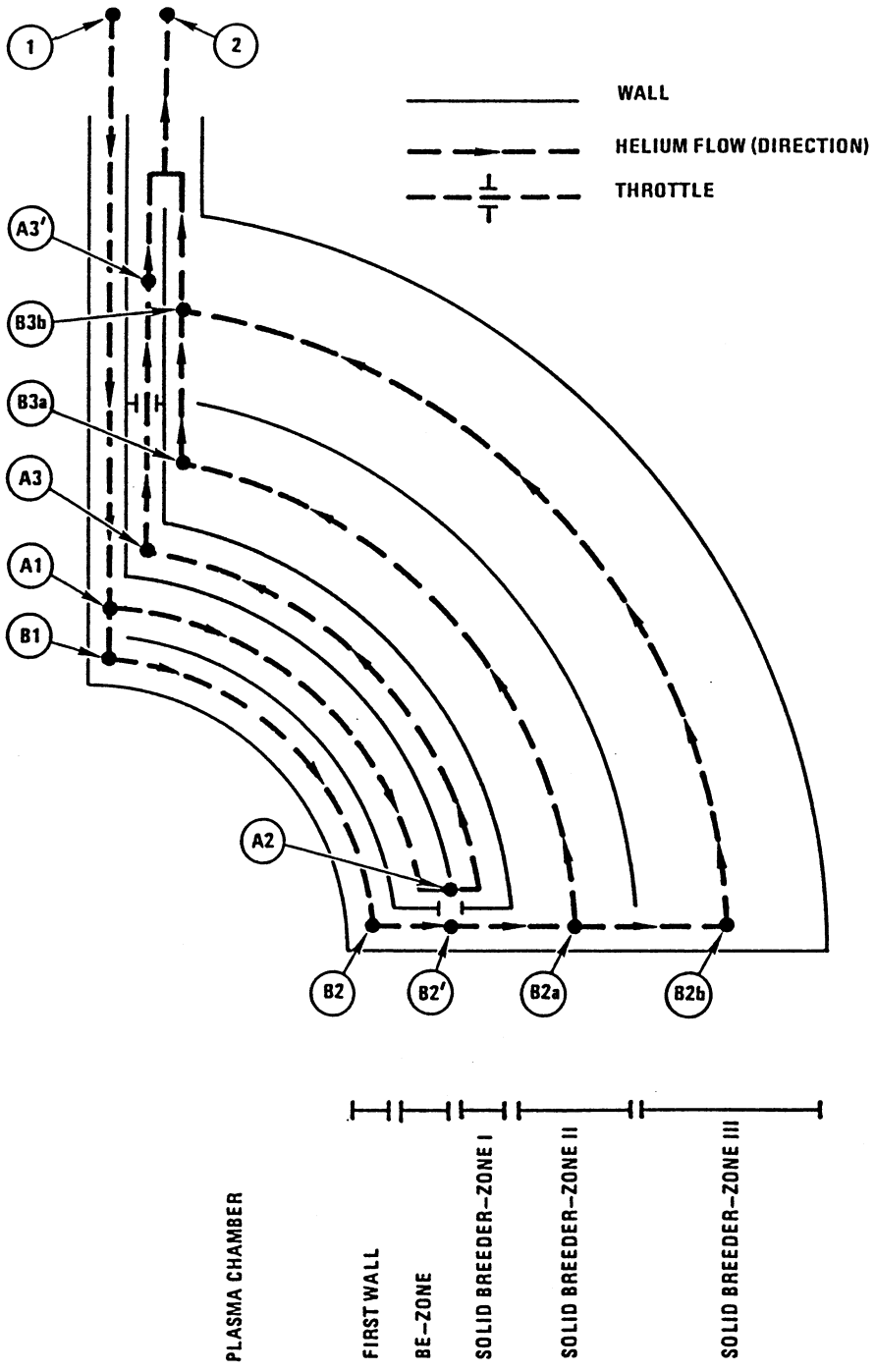

Fig. 8.5.-4. Quarter section of FISC torus with coolant routing.

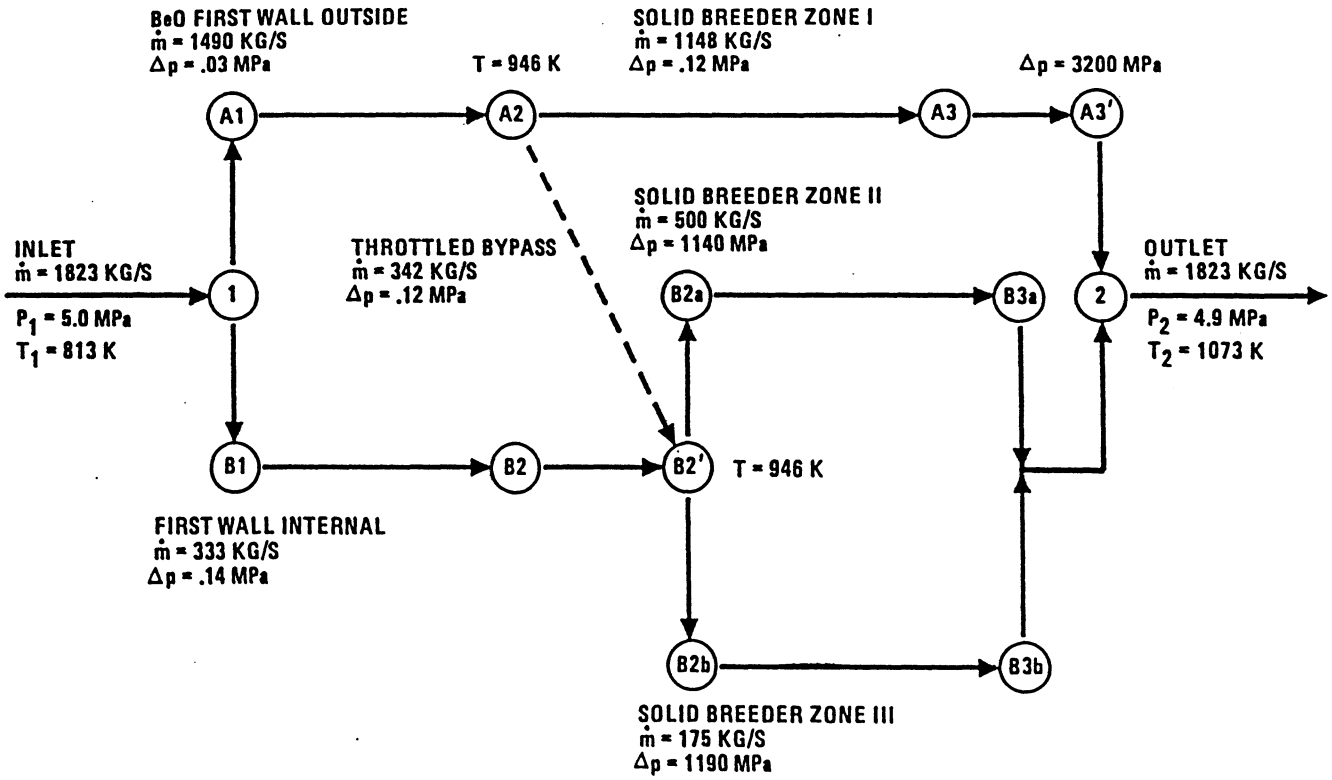

Fig. 8.5.-5. Schematic representation of helium flow path with mass flow rates, pressure drops and temperatures.

however, the heat transfer conditions can satisfy the 1475 K temperature limit for SiC-composites [68].

The second problem area is the breeder zone closest to the plasma, where the peak volumetric heat production is about two orders of magnitude higher than average value. Furthermore, the thermal conductivity of sintered $LiAlO_2$ plates is poor (1 W/m-K), and the maximum temperature is limited to 1000°C. To solve this problem, a design with thin plates (2 mm) and narrow gaps between the plates was chosen in order to maintain high coolant velocities and, therefore, good gas-side heat transfer. The corresponding high pressure drop is not of concern because the system pressure drop is dominated by the first wall.

Table 8.5.-IV shows that the temperatures of various components are close to or below their respective temperature limit. The pressure drops in the different cooling zones are also acceptable and match well. However, routing of the flow routing should be further optimized. The dominance of the first wall pressure drop, on the other hand, indicates that the system cannot sustain much increase in surface heat flux; the upper bound for the proposed design appears to be at a heat flux of 2 MW/m^2.

8.5.4. Neutronics

The neutronics calculations were performed with the Monte Carlo transport code, MCNP, [3] with statistical errors for all integral quantities limited to less than 1%. The Los Alamos Recommended Monte Carlo Cross Section set was used for all calculations. This set of cross sections was processed primarily from the basic ENDF/B-V data files [2].

Figure 8.5.-6 shows the one-dimensional model used in the neutronics calculation. This model is a full-coverage cylindrical blanket model and consists of a 40 mm thick SiC first wall, a 0.2 m thick BeO neutron multiplying zone, a 0.8 m thick Li_2O tritium breeding zone, and copper magnets. Silicon carbide is used as the 5% by volume structure in both BeO and Li_2O zones. The Helium coolant takes up 50% by volume in the first wall zone and 45% by volume in both the BeO and Li_2O zones. The density factor for both BeO and Li_2O compounds is assumed to be 80% in this design. Natural lithium is employed in the Li_2O compound. The performance of this reactor system is summarized in Table 8.5.-V and Fig. 8.5.-7.

Table 8.5.-V summarizes the neutronics performance of the blanket system described above. The total tritium breeding ratio is 1.17, 8.4% of which is attributable to the $^7Li(n,n'\alpha)T$ reaction in lithium, 0.5% to the Be(n,T)

TABLE 8.5.-V

NEUTRONICS PERFORMANCE OF THE HELIUM-COOLED FISC DESIGN

Tritium breeding (tritons/DT neutron)

$^6Li(n,\alpha)T$	1.065
$^7Li(n,n'\alpha)T$	0.098
Be(n,T)	0.006
Total TBR	1.17

Nuclear Heating (MeV/DT neutron)

Zone	Neutron Heating	Gamma-ray Heating	Total
SiC (FIRST WALL)	1.22	0.56	1.78
BeO	4.49	1.56	6.05
Li_2O	7.32	1.17	8.50
Magnet	0.005	0.18	0.18
TOTAL	13.04	3.47	16.51

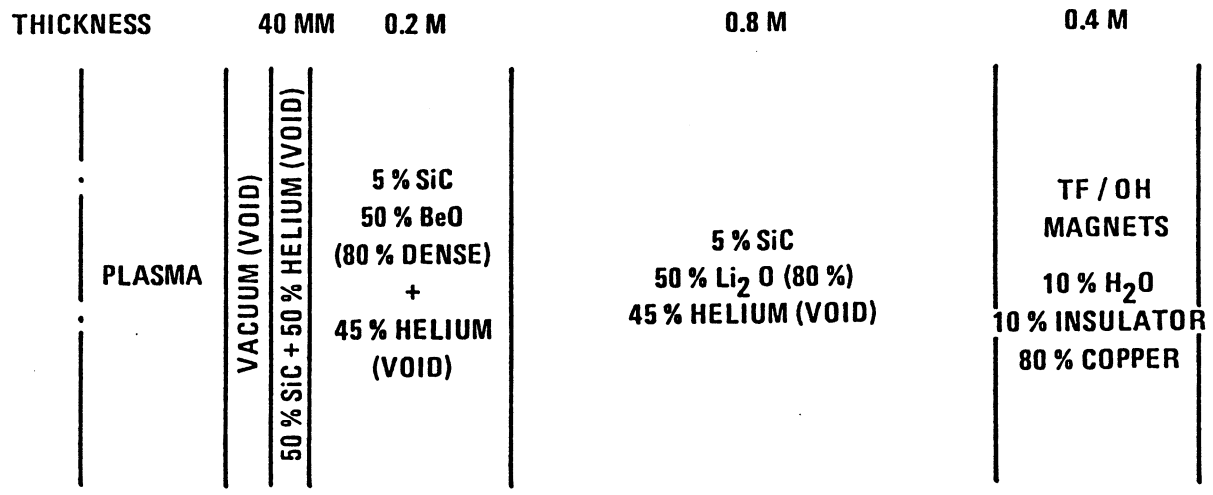

Fig. 8.5.-6. Schematic of the one-dimensional neutronics model for the helium-cooled ceramic TITAN reactor design.

reaction in beryllium, and the remainder is from the $^6Li(n,\alpha)T$ reaction in lithium. Also shown in Table 8.5.-V is the total nuclear heating rate in the system which is 16.5 MeV, of which about 82% of that is from neutron nuclear heating. The total recoverable heat in the blanket system will amount to about 16.9 MeV if the decay heat, estimated to be about 3.5% of the direct blanket heat, is taken into account. A blanket energy multiplication of about 1.2 results. The decay heat in this system results primarily from very short half-life radionuclides and would decay away quickly after shutdown.

It should be noted that Li_2O is used as the solid breeder in this neutronics calculation. To use the higher temperature capability of the blanket design $LiAlO_2$, was later selected for the heat transfer calculation. However, with the presence of Be as the neutron multiplier, the neutronics performance of the previous design can be achieved by simply adjusting the thicknesses of the different zones in the new design.

Figure 8.5.-7 presents the volumetric nuclear heating rate as a function of distance from the first wall and is normalized to 10 MW/m^2 neutron wall loading. The nuclear heating is about 60 MW/m^3 at the SiC first wall, and decreases to 31 MW/m^3 in the BeO compound at 0.1 m from the first wall. The volumetric heating peaks in the Li_2O compound at 136 MW/m^3 immediately behind the BeO zone due to significant neutron absorption in ^6Li in the soft neutron spectrum moderated by BeO. However, the heating rate in the Li_2O zone decreases rapidly as the location moves away from the BeO zone. It is about 2 MW/m^3 at 0.4 m from the BeO zone, as shown in Fig. 8.5.-7. The maximum nuclear heating rate in the magnet is about 0.4 MW/m^3 in the location immediately behind the Li_2O zone.

Figure 8.5.-8 shows the neutron flux distribution in the BeO zone, Li_2O zone, and the copper-alloy TF magnets. It appears that the maximum fast flux in the TF coils will be no more than 2×10^{20} n/cm^2-yr at 10 MW/m^2 neutron wall loading. Based on the fluence limit of 4×10^{22} n/cm^2 for spinel [16] insulator, then the lifetime of the TF coils will be about 200 years at 10 MW/m^2 wall loading, or 100 years at 20 MW/m^2. It is noted that the thickness of the Li_2O zone in this design is not optimized. The lifetime estimate indicates that an optimization study is possible to reduce the Li_2O zone thickness and still enjoy a plant life of the TF and OH coils of about 40 years operation.

8.5.5. Structural Analysis

In this section the pressure and thermal stresses of the SiC pressure vessel are calculated using the finite element code, ANSYS [25]. The most

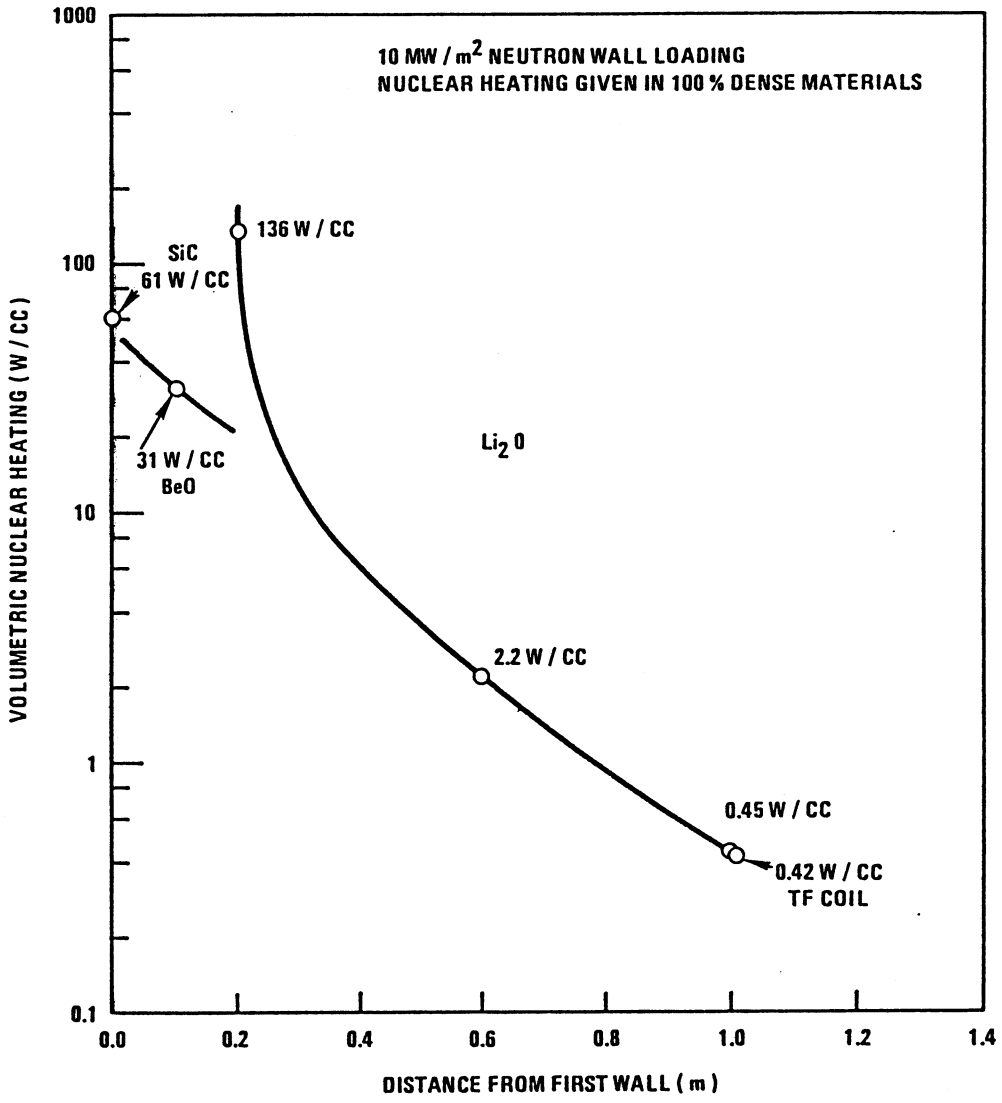

Fig. 8.5.-7. Volumetric nuclear heating rate in the helium-cooled ceramic blanket design (FISC).

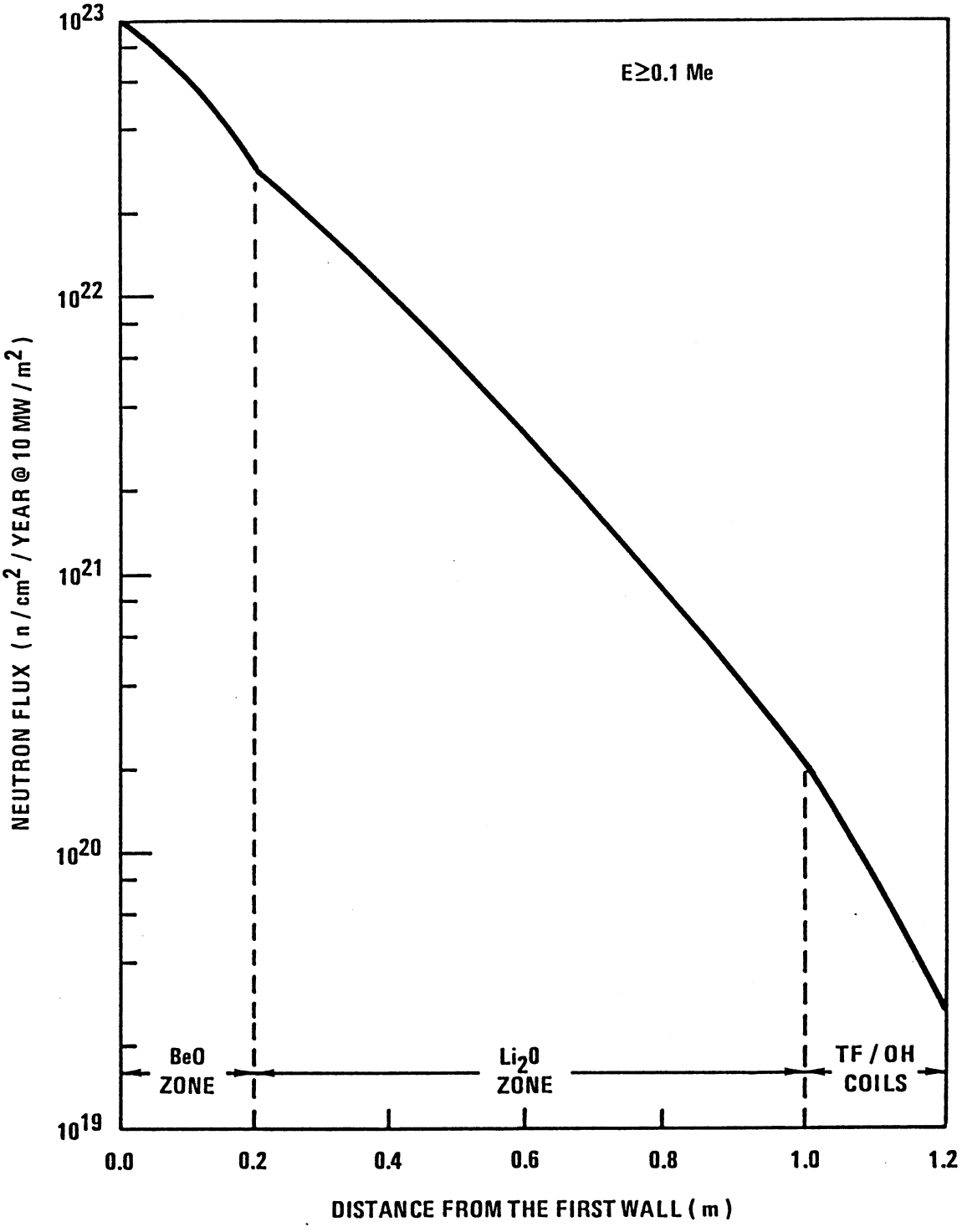

Fig. 8.5.-8. Neutron flux ($E \geq 0.1$ MeV) distribution in the helium-cooled ceramic design. The fluxes are given at 10 MW/m^2 neutron wall loading.

difficult aspects of the analysis are the material and structural modeling, which are complicated by the anisotropic, layered nature of the composite and by the toroidal shape of the vessel. These complications are dealt with by various means described below, providing adequate results for this initial scoping phase. Because high heat fluxes require thin walls and high pressures require relatively thick walls, the first wall stresses are crucial to the choice of the plasma-side wall thickness. To assess the viability of this concept, a preliminary design is first analyzed and subsequent modifications are incorporated as needed.

8.5.5.1. Modeling

Because of the difficulties associated with analysis of anisotropic layered structures, the results presented here are for a homogeneous, isotropic material with higher strength in compression than in tension. Because ceramic laminates incorporates many layers with fibers in different directions, this model should yield good results for the global behavior of the structure, but the possibility of delamination cannot be addressed.

The first wall is modeled as a poloidally axisymmetric ring using 2-D axisymmetric finite elements. This is coupled with analytical results for the toroidal pressure stresses to approximate the full toroidal shell. The model consists of 132 nodes and 96 quadrilateral elements, using the loadings and boundary conditions shown in Fig. 8.5.-9. It should be noted that subsequent design evolution from thermal-hydraulics analysis (Sec. 8.5.3) indicated a first wall channel dimension of 8 mm (Fig. 8.5.-2). Therefore, the results indicated here which are based on the longer span of 12 mm channels should be conservative. For the thermal analysis, a uniform heat flux is imposed on the plasma-facing surface and convective heat transfer to the coolant is included in the channel and on the shield-side surface. Uniform volumetric heating is also assumed, although it has little effect on either the temperatures or the stresses. Due to symmetry, the surfaces formed by making a poloidal "cut" are assumed to be adiabatic. For the stress analysis, the channel surfaces are pressure-loaded and toroidal symmetry is again used to establish the displacement conditions at the sides.

The material properties and strengths used in the analysis are given in Table 8.5.-VI. The high allowable strengths are typical of high-strength fiber-matrix ceramics, providing one of their major advantages. The thermal conductivity after irradiation, though, is quite low and a fairly conservative

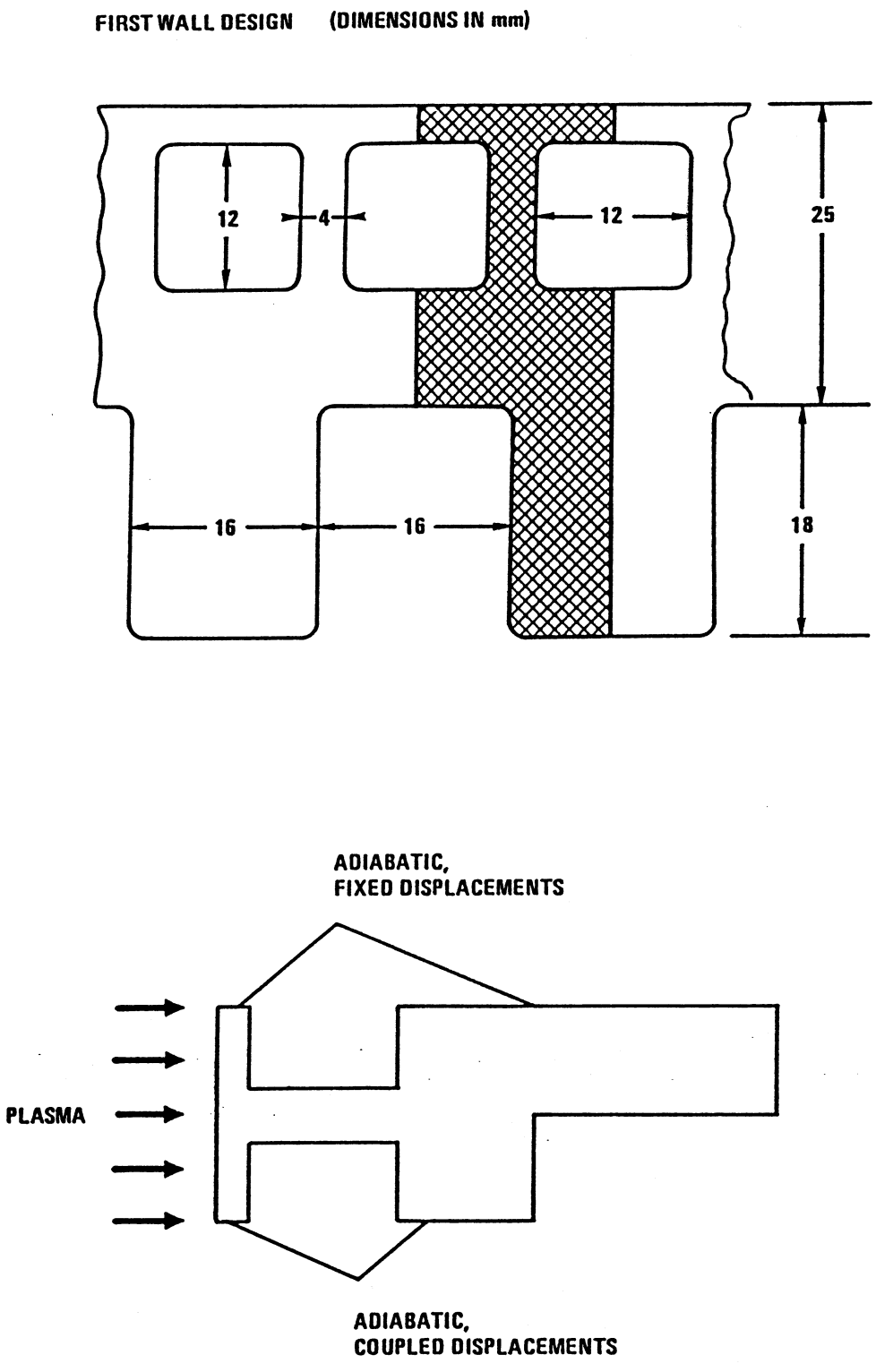

Fig. 8.5.-9. First wall structural analysis model for the helium-cooled ceramic design.

TABLE 8.5.-VI
PROPERTIES OF SIC

Young's modulus (GPa)	317
Coefficient of thermal expansion (K^{-1})	4.9×10^{-6}
Poisson's ratio	0.18
Thermal conductivity (W/m-K)	16
Design Allowable Stresses:	
σ_{comp} (MPa)	-700
σ_{tens} (MPa)	350

value of 16 W/mK has been adopted [68]. A higher conductivity would decrease the peak temperatures and stresses significantly.

8.5.5.2. Results

In all the discussion and contour plots that follow, the stresses presented are in the "z" or "hoop" direction because these are the most severe in all cases. The "severity" is determined by the likelihood to cause failure and its determination is complicated by the difference between the compressive and tensile strengths of the SiC. The failure criterion used here is a distorted Tresca criterion, which has been shown to work quite well for isotropic ceramics [69]. Equivalent stresses are not presented because they are meaningless for materials (such as SiC) that behave differently in tension and compression.

For the base design, which features a 2.5 mm thick front section, the pressure stresses (due to a pressure of 50 atm) are quite low. As shown in Fig. 8.5.-10, the peak compressive stress is about -145 MPa and the minimum is -132 MPa; there are no tensile stresses. Using shell theory [70] one can easily show that the radial stresses are negligible and the toroidal stresses are given by pa/t, where a is the first wall radius, p is the coolant pressure and t is the wall thickness. In this case, the toroidal stress is about -70 MPa and is again compressive everywhere. These pressure stress levels are within the design limits given in Table 8.5.-VI.

The thermal stresses are calculated following a heat transfer analysis which includes a 2 MW/m^2 surface heat load and a uniform volumetric heating of 122 MW/m^3. The bulk fluid temperature used for the analysis is 673°C and the

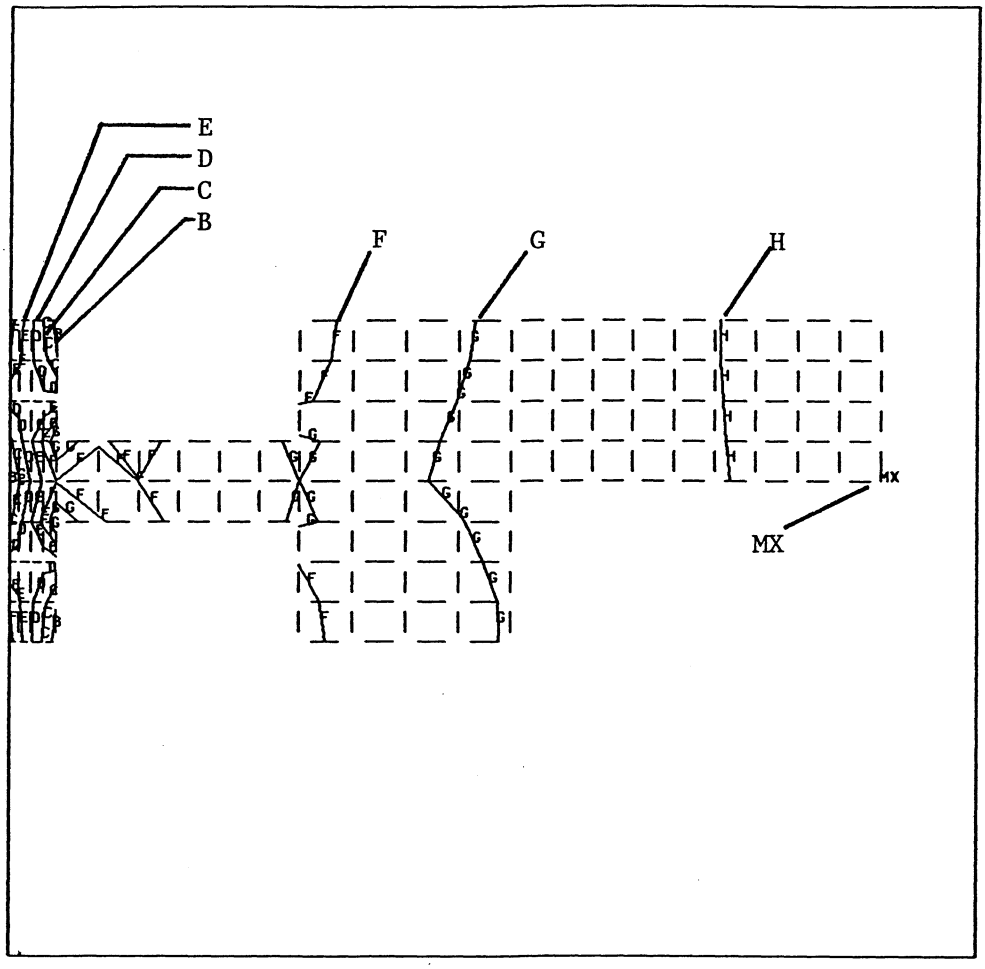

PRESSURE STRESS CONTOURS (MPa)

B=-144	F=-136
C=-142	G=-134
D=-140	H=-132
E=-138	MX=-131
MN=-145	

Fig. 8.5.-10. Pressure stresses in the FISC design.

heat transfer coefficients for the small channel and the multiplier side of the first wall are 9300 and 8180 W/m^2-K, respectively. The peak temperature of 1289°C, which occurred at the plasma-side surface, is slightly above the limit. The peak compressive stresses are also too high, as shown in Fig. 8.5.-11, which shows the combined pressure and thermal hoop stresses. Unfortunately, the toroidal thermal stresses are unknown, so a complete 3-D failure analysis cannot be done. It is clear, though, that the stresses must be reduced.

In order to reduce the peak temperature and peak stresses, the front (2.5 mm thick) section between the coolant channels and the plasma-side surface is reduced to 1.9 mm. Then, the peak temperature is 1196°C and the peak compressive and tensile stresses are -723 MPa and 159 MPa, respectively. These values are close to the allowable and compressive toroidal stresses may reduce the severity of the stress state, so this design appears feasible, pending the detailed 3-D analysis and multi-axial failure assessment.

8.5.6. Tritium

In this design, the bred tritium is to be released from the solid breeder to the main helium stream and removed in the tritium extraction circuit. After diffusing out from the solid breeder, the elemental tritium is first oxidized in a CuO bed before being extracted in a molecular sieve as shown in Fig. 8.5.-12. As indicated, to reduce thermal power losses, counter-current thermal regenerators will be needed in the helium extraction circuit. By assuming a side stream extraction of 1% of the primary coolant flow, the tritium inventory in the hot helium loop was estimated at 1.6 g, which is quite acceptable. The tritium extraction characteristics are also summarized in Fig. 8.5.-12.

8.5.7. Safety

This design has the best combination of low activation blanket materials to achieve inherent safety, namely SiC, helium, BeO and solid breeder. The induced activities in the blanket are about 5 to 6 orders of magnitude lower than for corresponding metallic designs reducing the waste disposal problem considerably. The induced activities would be dominated by impurities. Even though hands-on maintenance could not be possible in the plasma chamber, however, one week after shutdown, hands-on maintenance behind the blanket should be possible. Afterheat generation from the first wall blanket would be negligible shortly after shutdown. Coupled with the high temperature capability of the selected materials, no safety problem related to the afterheat is expected.

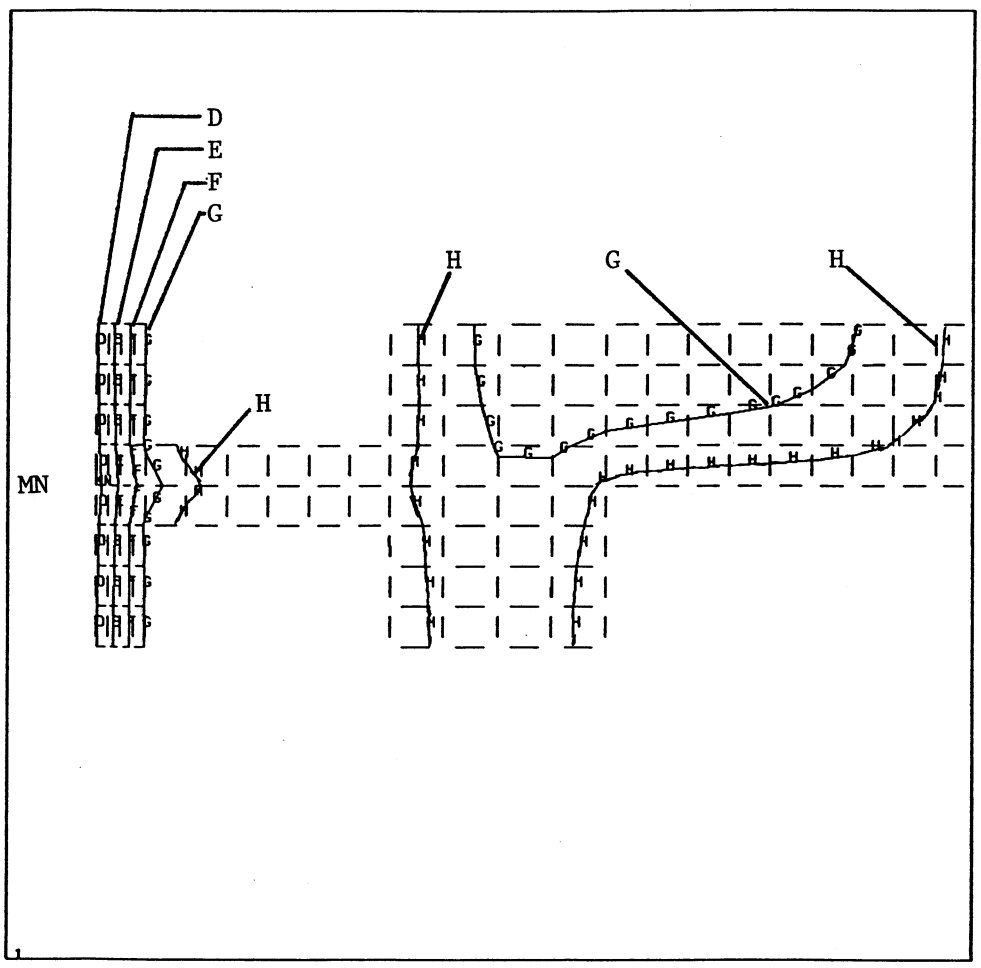

PRESSURE PLUS THERMAL STRESS CONTOURS (MPa)

D=-800
E=-600
F=-400
MN=-868
G=-200
H=0
MX=177

Fig. 8.5.-11. Pressure plus thermal stress in the FISC design.

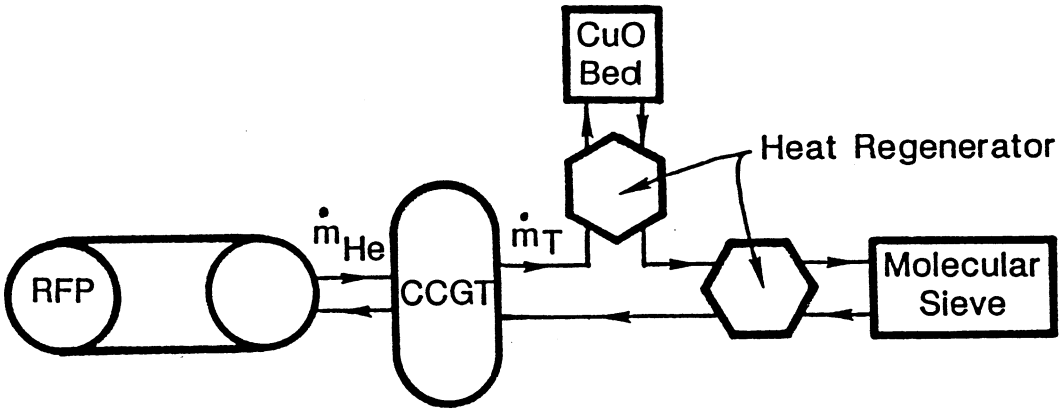

Fig. 8.5.-12. Schematic of tritium extraction for the TITAN FISC concept.

Based on the design of extracting the bred tritium from the main coolant stream, at 1% of the main coolant flow rate, the coolant tritium inventory was estimated to be 1.6 g which, if all released, would result in a site boundary dose of less than 0.2 rem.

The key safety-related item that needs to be addressed is routine tritium release and tritium releasable inventory from solid blanket materials. It is also important to identify the feasible low activation materials that can be used for other near torus components, (e.g., magnet coils and plasma heating devices) in order to ascertain the maintenance and waste disposal advantages of the FISC design.

8.5.9. Conclusions

The FISC design for TITAN is at an early stage of development. However, it appears to offer certain advantages:

1. This design has the best combination of materials to achieve inherent safety, since there is negligible induced afterheat from the blanket

material shortly after shutdown, and the induced radioactivities would be about 6 orders of magnitude less than for metallic structured designs. This would reduce the problem of reactor waste management considerably. Coupled with the high temperature capability of the design, no safety problem related to afterheat is expected.

2. With the compressive load design, FISC can take a neutron wall loading of 20 MW/m^2 at a first wall surface heat loading of 1.5 to 2 MW/m^2.

3. With the closed cycle gas turbine power conversion system (CCGT), a thermal efficiency of 40% or higher can be expected.

The key development need for the FISC design is in ceramic-fiber-matrix materials. This includes areas in material development, fabrication, joining technology, material impurity controls and irradiation effects. More detailed designs are also needed to better quantify the projected safety advantages of the FISC design, and to establish the potential in high wall loading reactors. The advantages of the concept are more compelling for lower power density, lower heat flux reactors.

8.6. DIRECTIONS FOR THE DESIGN PHASE

During the scoping phase of the TITAN study a large number of design concepts and options were considered. Of particular importance are the four blanket concepts described in this section. It was decided to narrow to two the number of FPC designs to be pursued during the design phase. The decision was necessary because of inadequate resources to pursue all four designs. The decision on which of the two concepts to pursue was difficult to make. All four concepts have attractive features. The lithium-loop design promises excellent thermal performance and is one of the main concepts being developed by the blanket technology program. The water design promises excellent safety features and use of more developed technologies. The helium-cooled ceramic design offers true inherent safety and excellent thermal performance. The molten-salt pool design is the only low-pressure blanket and promises passive safety. The lithium loop concept and the aqueous loop-in-pool concept were chosen for detailed conceptual design and evaluation in the design phase of the TITAN program. The choice was made primarily on the capability to operate at high

neutron wall load and high surface heat flux. The choice not to pursue the helium-ceramic and molten-salt designs should in no way denigrate these concepts. Both concepts offer high performance and attractive features when used at lower wall loads; these concepts should be pursued in other design studies.

REFERENCES

1. E. Cheng, GAT, private communication (1986).

2. R. MacFarlane, Los Alamos National Laboratory, private communication (1983).

3. Los Alamos Monte Carlo Group, "MCNP-A general Monte Carlo Code for Neutron and Photon Transport," LA-7396-M, Rev., Los Alamos National Laboratory (1981).

4. J. Briesmeister, Los Alamos National Laboratory, private communication, March 22, 1984.

5. D. Steiner, R. C. Block, and B. K. Malaviya, "The Integrated Blanket-Coil Concept applied to the Poloidal Field and Blanket Systems of a Tokamak Reactor," Fusion Tech. 7 (1985) 66.

6. D. L. Smith et al., "Blanket Comparison and Selection Study-Final Report", Argonne national Laboratory Report, ANL/FPP-84-1 (1984).

7. D. L. Smith, B. A. Loomis and D. R. Diercks, J. Nucl. Mater. 135 (1985) 125.

8. K. Natesan, J. Nucl. Mater. 115 (1983) 251.

9. B. Loomis and O. Carlson, Proc. Third Annual Conf. on Reactive Metals, Buffalo, NY, May 27, 1985, pp. 227-243.

10. D. N. Braski, "The Effect of Neutron Irradiation on the Tensile Properties and Microstructure of Several Vanadium Alloys," J. Nucl. Mater. 141-143 (1986) 1125.

11. S. Sharafat, UCLA, private communications (1986).

12. I. LeMay, Principles of Mechanical Metallurgy, Elsevier, New York, Oxford, 1981, p. 365.

13. C. H. Adelheim, H. U. Borgstedt and J. Konys, Fusion Techn. 8 (1985) 541.

14. O. K. Chopra and P. F. Tortorelli, J. Nucl. Mater. 122-123 (1984) 1201.

15. H. U. Borgstedt, M. Grundmann and J. Konys, Fusion Tech. 8 (1985) 536.

16. B. G. Logan, et al., "MARS-Mirror Advanced Reactor Study, Final Report," Lawrence Livermore National Laboratory Report, UCRL-53480, (1984).

17. W. C. Reynolds, J. Heat Transfer, Trans. ASME, (1960) 108.

18. G. W. Sutton and A. Sherman, Engineering Magnetohydrodynamics, McGraw-Hill Series in Mechanical Engineering, 1965.

19. J. A. Shercliff, "Magnetohydrodynamic Pipe Flow Part 2. High Hartmann Number", Fluid Mechanics, 13 (1962) 513.

20. J. C. R. Hunt, "Magnetohydrodynamic Flow in Rectangular Ducts", Fluid Mech., 21 (1965) 577.

21. J. C. R. Hunt and J. R. Holroyd, "Application of Laboratory and Theoretical MHD Duct Flow Studies in Fusion Reactor Technology", Culham Laboratory Report, CLM-R169 (1977).

22. M. A. Hoffman and G. A. Carlson, "Calculation Techniques for Estimating the Pressure Losses for Conducting Fluid Flows in Magnetic Fields", Lawrence Livermore National Laboratory Report, UCRL-51010 (1971).

23. H. Madarame, "Leakage Current Effects on the MHD Pressure Drops in Liquid Metal Blankets", UCLA Report, PPG-868 (1985).

24. B. A. Boley and J.H. Weimer, Theory of Thermal Stress, John Wiley & Sons, Inc., 1960.

25. G. J. DeSalvo and J. A. Swanson, "ANSYS User's Manual", Swanson Analysis Systems, Inc., July 1979.

26. M. I. Baskes, "DIFFUSE 83," Sandia National Laboratory Report, SAND-83-8231 (1983).

27. P. Chou and N. M. Ghoniem, J. Nucl. Mater. 117 (1983) 55.

28. V. A. Maroni et al., Nucl. Tech. 25 (1975) 83.

29. D-K. Sze and J. Brooks, "Aspire - Advanced Safe Pool Immersed Reactor," International Symposium on Fusion Reactor Blanket and and Fuel Cycle Technology, Oct. 27-29, 1986. University of Tokyo, Tokai-mura, Japan.

30. D. Steiner, et. al., "A Heavy Water Breeding Blanket," 11th Symposium on Fusion Engineering, Austin, Texas, November 1985.

31. K. Hannerz, "Adapting the LWR to Future Needs SECURE-P (PIUS)," Power Engineering, September 1985.

32. DWR/PWR 1300 MWe, Nuclear Engineering International, March 1984.

33. P. F. Tortorelli and J. H. Devan, Alloy Development for Irradiation Performance: Semiannual Progress Report for the Period Ending March 31, 1983, DOE/ER-0045/10 (1983) 201.

34. B. R. Diercks and D. L. Smith, "Corrosion Behavior of Vanadium-Based Alloys in Pressurized Water at 288°C," Presented at the Second International Conference on Fusion Reactor Materials, Chicago, Il, April 13-17, 1986 and to be published in J. Nucl. Mat.

35. M. J. Pourbaix, "Atlas of Electromechanical Equilibria in Aqueous Solutions," Oxford, New York, Pergamon Press, 1966.

36. D. N. Braski, "The Effect of Neutron Irradiation on Vanadium Alloy," Oak Ridge, Tn, CONF-860421--18, DE86009156.

37. H. R. Brager, "Effects of Neutron Irradiation to 63 dpa on the Properties of Various Commercial Copper Alloys," International Conference on Fusion Reactor Materials 2, April 14-17, Chicago, Il, HEDL-SA-3516FP.

38. H. R. Brager, H. L. Heinisch, and F. A. Garner, "Effects of Neutron Irradiation at 450°C and 16 dpa on the Properties of Various Commercial Copper Alloys," ADIP, DOE/ER-0045/13, (1984) 183.

39. G. J. Butterworth, "Transmutation and Activity Effects in High-Conductivity Copper Alloy Exposed to a First Wall Neutron Flux," J. Nucl. Mater. 135 (1985) 160.

40. H. L. Heinisch and H. R. Brager, "Tensile Property Change of Commercial Copper Alloys Neutron Irradiated at 450°C," DAFS, DOE/ER0046/19, (1984) 135.

41. D. W. Kneff, B. M. Oliver, R. P. Skowronski, L. R. Greenwood, "Helium Production in Reactor Irradiated Copper and Titanium, and Evidence for a Copper Three-Stage Reaction," DAFS, DOE/ER-0046/20 (1984) 13.

42. S. J. Zinkl, D. H. Plantz, R. A. Dodd, and G. L. Kulcinski, "Physical Properties of High-Strength, High-Conductivity Copper Alloys," DAFS. - DOE/ER-0046/20 (1985) 85.

43. J. A. Spitznagel, and J. W. Davis, "Response of Selected High-Strength, High-Conductivity Copper Alloys to Fusion Irradiation and Temperature Conditions," ADIP, DOE/ER-0045/13 (1984) 171.

44. H. R. Brager and F. A. Garner, "Conductivity Changes in Neutron Irradiated Commercial Copper Alloys at 450°C," DAFS, DOE/ER-0046/19 (1984) 138.

45. R. D. Boyd, et al., "Technical Assessment of Thermal-Hydraulics for High Heat Flux Fusion Components," Sandia National Laboratories Report, SAN84-0159 (1985).

46. M. A. Abdou, et. al., "Technical Assessment of the Critical Issues and Problem Areas in High Heat Flux Materials Component Development," UCLA Report, PPG-815/UCLA-ENG-84-25 (1984).

47. K. Stephan, H. Auracher, "Correlations for Nucleate Boiling Heat Transfer in Forced Convection," Int. J. Heat Mass Transfer, 24 (1981) 99.

48. L. S. Tong, Boiling Heat Transfer and Two-Phase Flow John Wiley & Sons, New York (1965) 156.

49. S. P. Timoshenko and J. M. Gere, Theory of Elastic Stability, McGraw-Hill, pp. 289 and 321.

50. A. Dombra, Chalk River Nuclear Laboratories, private communication, August 1986.

51. The NET Team, "NET Status Report," NET-51, December 1985.

52. K. Y. Wong, et. al., "Canadian Tritium Experience," Ontario Hydro, 1984.

53. D. Jeffert, Ontario Hydro, private communication, June 1986.

54. C. Baker, et. al.,"Tokamak Power Systems Studies," Argonne National Laboratory Report, ANL/FPP-85-2 (1985).

55. W. R. Grimes, "Molten Salt Reactor Chemistry," Nucl. Appl. Tech. 8 (1970) 137.

56. D. H. Berwald and S. Zenczak, "Assessment of Beryllium Resources for Fusion Applications," Fusion Technology, 8 (1985) 1143.

57. A. Klein and D-K. Sze, "The Costs and Benefit of Utilizing Beryllium as an Energy Multiplier," Second International Conference on Fusion Reactor Materials, Chicago, Illinois, April 13-17, 1986.

58. R. L. Erickson, "Crystal Abundance of Elements and Mineral Reserves and Resources," United States Geological Survey Prof. Paper 820, D. A. Brobst and W. R. Prat (Eds.), Washington, 1973, p. 21.

59. Y. Cha, Argonne National Laboratory, private communication.

60. J. Devan, Oak Ridge National Laboratory, private communication.

61. G. R. Hopkins, et. al., "Low Activation Fusion Reactor Design," Fusion Reactor Design and Technology, IAEA-TC-392/33, 1983.

62. R. W. Conn, et. al., "Lower Activation Materials and Magnetic Fusion Reactors," Nuclear Tech./Fusion 5 (1984).

63. I. Maya, et. al., "Inertial Confinement Fusion Reaction Chamber and Power Conversion System Study, Final Report," GA Technologies Report, GA-A17843 (1985).

64. R. J. Price, "Properties of Silicon Carbide for Nuclear Fuel Particle Coatings," Nuclear Tech. 35 (1977).

65. G. R. Hopkins and R. J. Price, "Fusion Reactor Design with Ceramics," Nucl. Eng. and Design/Fusion 2 (1985) 111.

66. G. R. Hopkins and J. Chin, "SiC/SiC Composites," GA Project 4411, GA-A18295, January 1986.

67. C. P. C. Wong, GAT, private communications.

68. C. P. C. Wong, E. T. Cheng, L. Creedon, C. R. Hopkins, C. Kessel, and K. R. Schultz, "A Low Activation Blanket for the Moving Ring Field-Reversed Mirror Reactor," GA Report, GA-A16543 (1981).

69. H. W. Babel and G. Sines, "A Biaxial Fracture Criterion for Porous Brittle Materials," J. Basic Eng., Trans. ASME, (1968) 285.

70. S. P. Timoshenko, Theory of Plates and Shells, McGraw-Hill, New York, NY (1959) 441.